



NTNU – Trondheim
Norwegian University of
Science and Technology

Robust attitude and heading estimation of submerged steering device

Marius Hjertaker

Master of Science in Cybernetics and Robotics

Submission date: May 2015

Supervisor: Jan Tommy Gravdahl, ITK

Norwegian University of Science and Technology
Department of Engineering Cybernetics



THESIS DESCRIPTION SHEET

Name: Marius Hjertaker
Department: Engineering Cybernetics
Thesis title: Robust attitude and heading estimation of submerged steering device

Thesis Description:

In order to increase the accuracy of the seismic data collecting for a marine seismic streamer a dynamic position (DP) device used to achieve high accuracy positioning of the seismic streamers. Achieving this require accurate attitude determination.

The purpose of this thesis is to design and experimentally test a attitude estimator for a marine seismic streamer. The embedded system has a limited processing capacity, so a lightweight estimator are preferable. Only IMU measurements are available for the estimator design, including three-axis accelerometer, magnetometer and gyroscope.

The following items must be considered:

1. Theoretical survey: existing methods for attitude estimation, filter design and robust estimation.
2. Simulations and implementation of the estimation algorithm.
3. Design and implement the non-linear observer's in MATLAB, and the MEKF for benchmark purposes.
4. Verification of the attitude observers using a small simulator, able of producing IMU data.
5. Test the observers on both simulated and real data
6. Test plausible error scenarios
7. Investigate methods for sensor calibration.

Start date: 2015-01-05
Due date: 2015-06-01

Thesis performed at: Department of Engineering Cybernetics, NTNU
Supervisor: Professor Jan Tommy Gravdahl, Dept. of Eng. Cybernetics, NTNU
Co-Supervisor: Torbjørn Barheim, Kongsberg Seatex AS



NTNU – Trondheim
Norwegian University of
Science and Technology

Robust attitude and heading estimation of submerged steering device

Marius Hjertaker

May 22, 2015

MASTER THESIS

Department of Engineering Cybernetics

Faculty of Information Technology, Mathematics and Electrical Engineering

Norwegian University of Science and Technology

Supervisor: Jan Tommy Gravdahl

Co-supervisor: Torbjørn Barheim

Preface

This master thesis concludes the final work of the Masters program at the Norwegian University of Science and Technology, Department of Engineering Cybernetics. Discussing, testing and implement method's for attitude estimation of a underwater steering device. The master thesis is conducted in collaboration with Kongsberg Seatex AS. This collaboration where motivated by interning at Kongsberg Seatex, working with sensor calibration of the underwater steering device. Studying these aspects evolved to further investigation of the system and attitude estimation.

The knowledge of classical physics such as kinetics and kinematics are useful to understand the thesis. Knowledge of SNAME notation and terminology of describing motion and reference frames would also be helpful.

Marius Hjertaker

Trondheim, May 22, 2015

Acknowledgment

I would like to thank my supervisor , professor Jan Tommy Gravdahl, for his continuous support, enthusiasm, understanding and helpful conversation during the work with this thesis. I really appreciate it. I would also like to thank Torbjørn Barheim at Kongsberg Seatex for his advices and technical support concerning the system, it's properties, limitations and system testing.

Last but not least. I would like thank those closest to me, for their understanding, encouragement and enthusiasm during the hole master's program.

M.H.

Summary

The accuracy of seismic surveys are vital in order obtain accurate and good analysis of the gathered data. This can be done using seismic cable control, where underwater steering devices guides and stabilizes the cables. In order for these underwater steering devices to have as accurate control as possible are a attitude observer beneficial. The orientation of the seismic cables would also help correcting and interpreting data gathered under the seismic surveys.

The industry standard observer for attitude estimations have for decades been the extended Kalman filter. However, extensive research the recent years on non-linear observers are changing this. Enabling a smaller footprint on the embedded system, and by fusing low-cost inertial sensors.

The main objective of this thesis are to implemented and experimentally test - with both simulated and experimental collected data - attitude observers integrating inertial measurements obtained from a inertial measurement unit (IMU). Enhancing their benefits and disadvantages.

A extensive literature study looking for different methods for attitude estimation, aspects related to attitude representation and current attitude observers solutions for seismic cables are presented. The main aspects of the selected observers are presented, with a further uncomplicated full overview and tuning properties.

By merging different properties, from two different papers, have the author proposed a new locally exponentially stable attitude observer, witch will globally decoupling of the roll and pitch estimates from yaw and magnetometer measurements. Moreover, all the observers are compared and given a clear overview of their estimation performance. Where their heading (yaw) estimation capabilities are emphasized.

A simulation model capable of simulating the IMU data from a dynamic model governed by angular velocities or input torques are also made. Calibration procedures of the raw experimental sensor measurements, using a batch based iterative calibration, are also presented.

Sammendrag

Nøyaktigheten til seismiske undersøkelser er avgjørende for oppnå nøyaktig og god analyse av de innsamlede dataene. Dette kan gjøres ved hjelp av seismiske kabelen kontroll, der undervannsstyringsenheter guider og stabiliserer kablene. For at disse undersjøiske styringsenhetene skal ha så nøyaktig kontroll som mulig, er en attityde observatør gunstig. Orienteringen av de seismiske kabler vil også bidra til å korrigere og tolke data innsamlet under de seismiske undersøkelsene.

Bransjestandar observatøren for attityde estimerer har i flere tiår vært Extended Kalman filter. Men omfattende forskning de siste årene på ikke-lineære observatører endrer dette. Muliggjøring av et mindre «footprint» på den innebygde system, og ved å fusjonere lav-kost treghetsensorer.

Hovedmålet med denne avhandlingen er å implementere og eksperimentelt teste - med både simulert og eksperimentelle innsamlede data - attityde observatører som integrerer treghetsmålinger hentet fra en treghets måleenhet (IMU). Og framheve fordeler og ulemper ved disse.

En omfattende litteraturstudie på jakt etter forskjellige metoder for attityde estimering, aspekter knyttet til attityde representasjon og nåværende attityde observatører løsninger for seismiske kabler presenteres. De viktigste aspektene ved de utvalgte observatører presenteres, med en påfølgende ukomplisert og oversiktlig total oversikt.

Ved å slå sammen ulike egenskaper, fra to forskjellige artikkler, har forfatteren foreslått en ny lokalt eksponentielt stabil attityde observatør, hvor yaw og magnetometermålinger globalt dekobles fra rull- og pitch estimerer. Videre er alle observatørene sammen gitt en klar oversikt over deres estimerings ytelser. Hvor deres yaw estimering vektlegges.

En simuleringsmodell i stand til å simulere IMU data fra en dynamisk modell, styrt av vinkelhastigheter eller moment er også gjort. Kalibreringsprosedyrer av rå – sensor - data blir også presentert, dette ved hjelp av en batch basert iterativ kalibrering.

Contents

Preface	i
Acknowledgment	ii
Summary	iii
Sammendrag	iv
1 Introduction	3
1.1 Background	3
1.2 Problem Formulation	4
1.3 Literature Survey	5
1.3.1 Attitude Representation	5
1.3.2 Attitude Estimation	5
1.3.3 Attitude Estimation for Seismic Cables	7
1.3.4 Calibration	8
1.4 Objectives	8
1.5 Limitations	8
1.6 Thesis Contributions	9
1.7 Structure of the Report	10
I Background and Theory	11
2 System Dynamics and Kinematics	13
2.1 Reference Frames	13
2.2 Attitude Representation	15

2.2.1	Euler Angels	16
2.2.2	Unit Quaternions	17
2.2.3	Gibbs Vector	19
2.2.4	Topological Obstructions and Unwinding	20
2.3	Coordinate Transformation	20
2.4	Kinematics and Kinetics	22
3	Attitude Observers	25
3.1	Linear Acceleration Mapping and Magnetometer Tilt Compensation	26
3.2	QUEST - QUaternion ESTimator	27
3.3	MEKF	28
3.4	Observer Using Single Vector Measurements	30
3.5	Globally Exponentially Stable Observer	32
3.6	Angular Velocity Observer	34
3.7	Developed Attitude Observer	35
4	Sensors and Sensor Calibration	39
4.1	Sensors	39
4.1.1	Gyroscope	40
4.1.2	Accelerometer	41
4.1.3	Magnetometer	42
4.2	Calibration	43
4.2.1	Offline Calibration	44
4.2.2	Online Calibration	45
II	System Description	49
4.3	System Properties	51
4.4	System Model, Approximations and Simplifications	52
4.4.1	Rigid Body Inertia	53
4.4.2	Roll Dynamics	54
4.4.3	Foil Theory	54

4.4.4	Rolling Added Mass, Drag and Restoring	56
4.4.5	IMU Centripetal Acceleration Model	57
III	Simulation Model	59
5	Simulation model	61
IV	Implementation	63
6	Algorithm Implementation Aspects	65
6.1	Discrete Implementation	65
6.2	Corrector-Predictor Formulation	66
6.3	Signal Processing	67
6.4	Ad-hoc Magnetic Disturbance Handling	68
7	Algorithm Implementation	69
7.1	Linear Acceleration Mapping and Magnetometer Tilt Compensation	70
7.2	QUEST Algorithm	71
7.3	MEKF Algorithm	73
7.4	Batista Algorithm	76
7.5	Grip Algorithm	77
7.6	Angular Velocity Observer Algorithm	80
7.7	Developed Attitude Observer Algorithm	82
7.8	Calibration	83
V	Results	85
8	Preliminary	87
9	Simulations Results	89
9.1	Linear Mapping and Magnetic Tilt Compensation	90
9.2	Observers using Single Vector Measurements	93

9.3	Developed Attitude Observer and Angular Velocity Estimation	103
9.4	SO(3) Confined vs Globally Defined Observer	109
9.5	Comparison of the Attitude Observers	111
10	Experimental Tests / Water Tests	121
10.1	Attitude Estimation	123
11	Calibration	131
11.1	Calibration Simulation	131
11.2	Calibration of Experimental Data	132
VI	Overall Discussion	137
12	Overall Discussion	139
VII	Conclusion and Further Work	143
13	Conclusion	145
14	Further Work	147
VIII	Appendix	149
A	Acronyms	151
B	Assumptions, Definitions	153
B.1	Assumption 1	153
B.2	Assumption 2	153
B.3	Assumption 3	154
B.4	Definition 1	154
B.5	Theorem 3.5 in (Nocedal and Wright, 2006)	154
C	Simulation Parameters	155

D Additional Results	159
D.1 Developed observer - Correction Term Comparison	159
D.2 Additional Field Test Results	161
E Simulink Model	171
Bibliography	175

List of Figures

2.1	The Geodetic(l, μ, h), ECI(x_i, y_i, z_i), ECEF(x_e, y_e, z_e), NED(x_n, y_n, z_n) and body / Bird(x_b, y_b, z_b) coordinate systems.	14
2.2	Illustration sketch of the steering device, including frame conventions and placement. The overall steering unit are seen to the left, while on of the steering wings including the inertial measurement unit are viewed to the right	23
4.1	The steering device, courtesy http://www.km.kongsberg.com/	51
4.2	A cubic simplification of the bird wing's. The bird wing's hight, width, depth and mass are specified by h, w, d and m respectively	53
4.3	Illustration sketch of bird wing foil. Where α represents the angle of attack, F_L , and F_D are the lift and drag components of the total force F_{wing} forces, and are respectively defined perpendicular and parallel to the in-flow fluid flow velocity vector U	55
5.1	Top layer Simulink simulation model. Sources in green - angular velocity inputs and torque inputs, sinks in red - data storage, the other subsystems in yellow - IMU, kinematics and torque model.	62
7.1	Comparing the Gibbs (green) and unit quaternion (magenta) parametrization of the attitude error in MEKF, during a 360° roll motion. Zoom of the transaction between $+180^\circ$ to -180° roll	74
7.2	Comparison using QUEST and not using QUEST to initialize the observer in Table 7.4. The MEKF is used as truth goal. Data from field testing are utilized	79

9.1	Linear mapping. Roll, pitch and yaw error when subjected to magnetic distortion. Simulation using small roll and pitch angles ($\pm 2^\circ$)	91
9.2	Centripetal acceleration contribution. Worst case scenario, maximum wing deflection, 20° , and bird roll angular velocity up to $25^\circ/s$	92
9.3	Sensor data. Complex maneuver.	94
9.4	Quaternion estimate using a single vector observation. The actual or real Euler angles in red, the estimated Grip and Batista quaternion in blue and cyan respectively	96
9.5	Euler estimate using a single vector observation. The actual or real Euler angles in blue, the estimated Grip and Batista Euler in blue and cyan respectively	97
9.6	Euler estimate error using a single vector observation. Grip and Batista illustrated with blue and cyan respectively	98
9.7	The actual and estimated X-, Y- and Z-axis normalized acceleration. Obtained by the Batista using a single vector	99
9.8	The actual and estimated X-, Y- and Z-axis normalized auxiliary vector $\hat{v}(t)$. Obtained by the Batista using a single vector	100
9.9	Euler estimate error using a single vector observation undergoing slow dynamics. Grip and Batista illustrated with blue and cyan respectively	102
9.10	Wing deflection. Sourced from data collected during water test	104
9.11	Gyroscope estimate.	105
9.12	Normalized acceleration estimate.	106
9.13	Normalized magnetic field estimate.	107
9.14	Euler angles estimates. The actual estimates(blue), the Developed attitude observer(green) and the Magnis estimate(red)	108
9.15	Comparison of globally defined and SO(3) confined attitude estimation. Represented by the quaternion error angle	110
9.16	Quaternion estimates. Comparing the algorithms of Grip(purple), QUEST(striped, red), MEKF(striped, yellow) and the developed(green) attitude observer. The actual attitude in blue	112
9.17	Euler angle error. Comparing the algorithms of QUEST(striped, blue), MEKF(striped, red), Grip(yellow) and the Developed(purple) attitude observer	113

9.18 Grip(striped, yellow) and MEKF(striped, red) Gyro bias estimation compared against the actual bias. Both methods converge to the actual gyro bias	114
9.19 Euler angle estimate error. Magnetic misalignment and scale factor are introduced at 100 seconds and turned off after 300 seconds	115
9.20 Grip and Developed with As-hoc magnetic disturbance handling, Euler angle estimate error. Magnetic misalignment and scale factor are introduced at 100 seconds and turned off after 300 seconds	116
10.1 Field test. Tail-buoy in left photo (mounted on the aft of the cable), the Bird mounted on the cable in the up-right photo and the seismic cable winch in the down-right photo.	122
10.2 Experimental test, day one. Obtained raw sensor data	123
10.3 Experimental test, day two. Obtained raw sensor data	124
10.4 Field test Midøy day 1. Euler angle estimation, LinearMapping(striped, blue), QUEST (striped, red), MEKF(striped, yellow) and Grip(purple)	125
10.5 Field test Midøy day 1 zoom. Euler angle estimation, LinearMapping(striped, blue), QUEST(striped, red), MEKF(striped, yellow) and Grip(purple)	126
10.6 Field test Midøy day 1. Gyro bias estimation, MEKF(striped, red) and Grip(blue)	127
10.7 Field test Midøy day 1. Euler angle estimation using single vector observation, MEKF(striped, yellow) and Batista(striped, light blue)	128
11.1 Calibrated magnetometer measurements (dotted, red) compared to the raw magnetic measurement(dotted, yellow). The estimated IMU-sensor axis in black, magenta and green.	134
11.2 Calibrated accelerometer measurements (dotted, red) compared to the raw accelerometer measurement(dotted, yellow). The estimated IMU-sensor axis in black, magenta and green.	135
D.1 Comparison of different injection terms in the Developed observer.	160
D.2 Field test Midøy day 1. Euler angle estimation, converted to the Bird frame, linear mapping(striped, blue), QUEST(striped, red), MEKF(striped, yellow) and Grip(purple)	162

D.3	Field test Midøy day 1. Quaternion estimation, QUEST(striped, blue), MEKF(striped, red), Grip(yellow) and Batista(striped, green)	163
D.4	Field test Midøy day 1. Euler angle estimation RMS, linear mapping(striped, blue), QUEST(striped, red), MEKF(striped, yellow) and Grip(purple)	164
D.5	Field test Midøy day 1. Batista, normalized acceleration estimates(blue) and the measured(red).	165
D.6	Field test Midøy day 2. Euler angle estimation, LinearMapping(striped, blue), QUEST (striped, red), MEKF(striped, yellow) and Grip(purple)	166
D.7	Field test Midøy day 2. Quaternion estimation, QUEST(striped, blue), MEKF(striped, red), Grip(yellow) and Batista(striped, green)	167
D.8	Field test Midøy day 2. Euler angle estimation RMS, linear mapping(striped, blue), QUEST(striped, red), MEKF(striped, yellow) and Grip(purple)	168
D.9	Field test Midøy day 2. Euler angle estimation, converted to the Bird frame, linear mapping(striped, blue), QUEST(striped, red), MEKF(striped, yellow) and Grip(purple)	169
D.10	Field test Midøy day 2. Gyro bias estimation, MEKF(striped, red) and Grip(blue) . .	170
E.1	IMU model.	172
E.2	Accelerometer model	172
E.3	Magnetometer model	173
E.4	Gyroscope model	173
E.5	Kinetic model	173
E.6	Kinematic model.	174

List of Tables

7.1	QUEST	72
7.2	Multiplicative Extended Kalman Filter	75
7.3	Non-linear attitude observer using single vector measurements	77
7.4	GES Non-linear attitude observer using multiple vector observations	78
7.5	Angular velocity observer	81
7.6	Proposed attitude observer	82
9.1	Batista gains	95
9.2	Angular velocity input	101
9.3	Root-mean-square Euler angle error. Comparing of Grip, QUEST, MEKF and the Developed attitude observer.	112
9.4	Root-mean-square heading error impact using wrong local magnetic field. Comparing the performance of QUEST, MEKF, Grip and developed attitude observer. The observer assume the local magnetic field at Trondheim. Although the actual operation area are 178 km north and west from Trondheim	118
11.1	Magnetometer calibration estimates, compared to their true values. Using ring formed data, 360° rolling and pitch less then 15°	132
11.2	Magnetometer calibration estimates, experimental data.	132
11.3	Accelerometer calibration estimates, experimental data.	133
C.1	Initial simulation parameters	155
C.2	Bird simulation parameters	156

C.3 IMU simulation parameters 157

Chapter 1

Introduction

The master thesis is presented in this chapter, its background and motivation explained and the problem formulation stated. The most relevant literature which has been studied and used is discussed. The thesis contributions is also presented, as is the structure of the rest of the thesis.

1.1 Background

The used of two-dimensional (2D) and three three-dimensional (3D) marine seismic surveys has been used for decades by the oil and gas industry. Enabling mapping of the geological structures of the seabed. Towed cables equipped with seismic receivers are dragged through the water, recording acoustic (sound) waves reflected by the seabed. Sound waves that are generated by bursting air-guns ([Davies et al., 2004](#)).

A 3D seismic survey provide a static picture of the earth. This technology uses multiple closely separated towed cables that provide an detailed data array about the geological features ([Davies et al., 2004](#)). In doing so do the risk of crossing the towed cables appear. Which may cause severe damage to the towed equipment. One solution would be to have a sufficient gape, separating the towed cables. However, the data acquisition detail increases with the decrease of separation. It would therefore be beneficial to have as small separation as possible. Utiliz-

ing multiple control/steering devices along the cables streamers, so-called birds, can the towed cables be more closely separated. Enabling dynamic positioning (DP) of the cables streamers. Which again would enable precise 3D seismic survey. Furthermore, precise 4D seismic surveys could be conducted. This is repeatable 3D survey, providing time structural changes in the geometric topology (Davies et al., 2004).

As part of achieving this are accurate bird (steering device) attitude and heading needed, together with position control. The focus of this thesis lies on the attitude estimation of these birds. Using on-board bird sensors - an internal measurement unit (IMU) - to estimate the attitude and heading.

1.2 Problem Formulation

The purpose of this master thesis is to design, implement and experimentally test a robust attitude estimators for a underwater steering device (bird). Since the bird used in this study has a limited processing capacity, would it be preferable with lightweight but precise attitude estimator.

Opposed to a statistical (e.g Extended Kalman filter) approach do a non-linear estimator provide a smaller footprint on the processor. It would therefore be preferable to use a non-linear estimator. However, to verify or at least provide a benchmark of the non-linear observer estimation will a Multiplicative Extended Kalman Filter (MEKF) be considered. Due to the process capacity on the bird, will simulations and algorithm tests be made on a computer. Where the algorithms will be subjected to both simulated and experimental collected data.

The data are collected using a IMU, consisting of three-axis accelerometer, three-axis gyroscope and three-axis magnetometer. Ferromagnetic objects near the IMU, infecting the magnetic measurements, are a great concern in the embedded system, and must be considered.

Moreover, to obtain a good attitude estimate are precise inertial measurements are needed. Calibration routines are therefore needed. Although, calibration partially goes out of the scope

of this thesis are some calibration aspects also considered.

1.3 Literature Survey

The appropriate material that was discovered during the literature survey will be summarized briefly in the following sections.

1.3.1 Attitude Representation

In order to understand and be able to design methods for attitude estimation are knowledge of mathematical notation, their properties and advantages beneficial. There are numerous methods of representing the orientation of an object. [Shuster \(1993\)](#) provide a comprehensive study on the most known parametrizations, and their advantages and disadvantages. A total of twelve different attitude representation parametrizations are presented. Varying from vector space representation to Euler angles and Quaternions. Vectors using both three and four parameters, as well as different size matrices.

1.3.2 Attitude Estimation

This is a widely explored subject. However, researcher are still trying to improve methods with theoretical analysis and experiments, as well as producing new methods. For decades have the Kalman filter (KF), and extensions(e.g extended Kalman filter), been the estimation method of choice. The Kalman filter was first introduced in the 1960 ([Kalman, 1960](#)), and has later gotten multiple extension. A comprehensive overview can be seen in [Crassidis et al. \(2007\)](#). Moreover, [Crassidis et al. \(2007\)](#) states that the KF encounters difficulties when it comes to non-linearities, and stability proofs. This has motivated researchers to look for new attitude estimation methods ([Nijmeijer and Fossen, 1999](#)). Attitude filters utilizing the non-linear structures of the system. Resulting in beneficial theoretical analysis, proving robustness and stability convergence.

The last decade has a number of such non-linear attitude observers been introduced. [Vik and Fossen \(2000\)](#) proposed a non-linear attitude observer using linearly mapped measurements in a quaternion based observer. Where static inertial measurements are required. [Mahony et al. \(2005\)](#) introduced attitude observers based passivity and inertial vector measurements. Resulting in better stability properties and locally exponential stability. However, stationary reference vectors and unbiased gyro rate measurements were assumed.

The work of [Mahony et al. \(2005\)](#) greatly inspired [Bonnabel et al. \(2008\)](#) to introduce theory for so called symmetry preserving observers. The symmetries (invariance) of a system has been greatly used in control theory for feedback design, not so much in observer design ([Bonnabel et al., 2008](#)). Utilizing these system symmetries did [Martin and Salaün \(2007\)](#) propose invariant observers, governed by direct input of inertial measurements. [Martin and Salaün \(2007\)](#) also considers the drawbacks of this approach. Where the error variable coupling are a major concern, mainly the coupling of attitude and the earth magnetic field. Which in practice would mainly affect the heading estimation.

Integration of GNSS velocity measurements with non-stationary reference vector were then later introduced by [?](#) , which resulted in a semi-global exponential stability. Using projection were [Grip et al. \(2011\)](#) able to propose a semi-global estimator for a time varying reference vector and with biased internal measurements.

Global stability convergence however has been rather difficult to prove. Since confining the attitude dynamics on the unit sphere and $SO(3)$ leads to unwinding and topological obstructions ([Bhat and Bernstein, 2000](#)). This means that a locally designed system, such as $SO(3)$, are not able to globally stabilize the system to a rest configuration. In light of this did were [Grip et al. \(2012a\)](#) able to design a globally exponentially stable observer using a larger state space formulation that converges to $SO(3)$, and integration of GNSS and inertial measurements. [Batista et al. \(2012b\)](#) follows that same approach but considers a stationary reference vector. Furthermore, a newly released paper where the main work of [Batista et al. \(2012b\)](#); [Grip et al. \(2011, 2012c\)](#) are considered, are presented by [Grip et al. \(2015\)](#). Presenting a globally exponentially stable observer using GNSS and inertial measurements and gyro bias estimation.

[Hua et al. \(2014b\)](#) on the other hand have designed a almost globally asymptotically stable observer. Where the observer is aided by velocity measurements in the body-frame. Moreover, the attitude (roll, pitch) are globally decoupled from magnetometer measurements.

Attitude estimation using only single vector measurements can also be found in the literature [Batista et al. \(2012a\)](#); [Mahony et al. \(2009\)](#) to mention a few. However, this requires persistent excitation (PE) to be possible. Meaning that the attitude of the object being estimate has to have "rich enough" excitation. This PE condition can also be utilized for to obtain a attitude estimate, in presence of magnetic distortion or temporarily loss of vector measurements ([Grip et al., 2015](#)).

Applications

Many comparison and application driven studies can also be found in the literature. [Utstumo and Gravdahl \(2013\)](#) provide a comparison of the MEKF and the complementarity filter of [Mahony et al. \(2008\)](#) for agricultural robotics. [Borup et al. \(2014\)](#) uses theory from [Grip et al. \(2012c\)](#) for designing a depth-observer, using a pressure sensor and inertial measurements, for a AUV. [Bryne et al. \(2014\)](#) expands the work of [Grip et al. \(2013\)](#) for translation motion, using time-varying gains for a dynamic positioning. Using a quadrotor helicopter do [Hua et al. \(2014a\)](#) present an observer, that globally decouples the attitude (roll, pitch) from the heading (yaw) estimation. This to only present a few.

1.3.3 Attitude Estimation for Seismic Cables

A survey for existing seismic cable observers show only the study of [Nguyen and Egeland \(2004\)](#). However, this observer consider a towed seismic cable attached to a one depth controller at end and with a pre-described motion at the other.

1.3.4 Calibration

The literature are full of calibration routines for inertial measurement sensors. Both online, using batch like methods, both linear and non-linear approaches, to offline calibration procedures using external measurements and references. [Alonso and Shuster \(2002\)](#); [Foster and Elkaim \(2008\)](#); [Vasconcelos et al. \(2011\)](#); [Crassidis et al. \(2005\)](#) represent some of these approaches.

1.4 Objectives

The main objectives of this master thesis are to

- Study existing method's of attitude estimation and attitude representation. Its imperative that observers are able to estimate the attitude by only using IMU collected data.
- Design and implement the non-linear observer's in MATLAB, and the MEKF for benchmark purposes.
- Verification of the attitude observers using a small simulator, able of producing IMU data.
- Test the observers on both simulated and real data
- Test plausible error scenarios

1.5 Limitations

The objectives described in Section 1.4 are limiting factors. Moreover, there a several limiting factors concerning attitude estimation of this system. One of the main limitations are the lack of multiple measurement sources. As only inertial measurements are available for determining the attitude, would these at least need to be precise.

A system model and model coefficients are not known. Resulting in multiple assumption and inaccuracies. The lack of a system model also limits the possibility of making model based

and/or model aided observers. Bird simulations would thereby also be very approximated.

The bird itself have some constraints. This could be both beneficial and a disadvantage. The overall system are fairly limited to roll motions, pitch motions are small and yaw motions are quite slow. On the contrary do other parts of the system has fairly large roll, pitch, yaw motions. Although, dynamic roll motion are complex itself; consisting of a rigid-body rotation in a fluid, do pitch and yaw dynamics take this even more complex level; including dynamics in both pitch and roll in a non-rigid body.

With regard to the attitude estimation could the geographical wideness of a seismic survey introduce limitations, as the knowledge of local measurement references may be time-varying.

1.6 Thesis Contributions

The main thesis contributions and aspects are as follows:

- Development of a new attitude observer
- Comparison of the attitude observer of [Grip et al. \(2015\)](#) and [Batista et al. \(2014b\)](#) with MEKF, QUEST and a Developed algorithm. With a corresponding clear overview of the attitude observers. The angular velocity observer of [Magnis and Petit \(2015b\)](#) are also clearly present.
- MEKF attitude error representation comparison. Unit quaternion versus Gibbs vector representation.
- A simplified model of external roll forces acting on the system
- Experimental testing, on data collected during system field test
- Implementation and test of a batch based IMU-measurement calibration routine for bias, scale factor and orthogonality errors.
- IMU and system simulation model, developed in Simulink.

- Object-oriented MATLAB code, including corrector-predictor formulation of the non-linear observers.
- A extensive literature study. Including, attitude observers, attitude representation, sensor calibration and modeling.

1.7 Structure of the Report

The rest of the report are organized as follows:

- Part I gives an introduction to theory and methods used in the thesis. Attitude representation, reference frames and coordinate transformations for navigational purposes, introduction of the concepts of the attitude observers studied and sensor modeling.
- Part II includes descriptions of the system and approximations utilized for simulation of the system.
- Part III a short presentation of the Simulink simulation model
- Part IV presents a overview of the implemented and studied observers. Some implementation aspects are also found.
- Part V includes simulation study and experimental test results.
- Part VI include a general discussion relating the overall thesis and results.
- Part VII presents a short summary and conclusions of the main results in the thesis. Recommendations for further work are also found here.
- Part VIII contains the thesis appendix. Where acronyms, assumptions, additional results and bibliography are found.

Part I

Background and Theory

Chapter 2

System Dynamics and Kinematics

This chapter gives introduction of the theory and background material used in the rest of the master thesis. Including different and relevant notations and definitions, such as reference frames, some relevant attitude representations, coordinate transformations and some kinematics.

2.1 Reference Frames

Geodetic coordinate system: The geodetic coordinate system is a widely used in GPS-based navigation. This coordinate system are defined near the earth surface in terms of the longitude, latitude and height, denoted (l, μ, h) respectively.

ECI: Earth-centered inertial reference frame $\{i\} = (x_i, y_i, z_i)$ is a global coordinated system with the origin O_i in the center of the earth. This is a non-accelerating, fixed, reference frame with its origin in the center of the earth.

ECEF: Earth-centered earth fixed reference frame $\{e\} = (x_e, y_e, z_e)$ is a global coordinated system with its origin equal to the ECI, $O_e = O_i$. This frame is is rotating relative to the ECI, rotating with a rotational rate $\omega_e \approx 7.2921e^{-5}$ rad/sec. For a vehicle moving at relative low speeds, this frame can be seen as inertial.

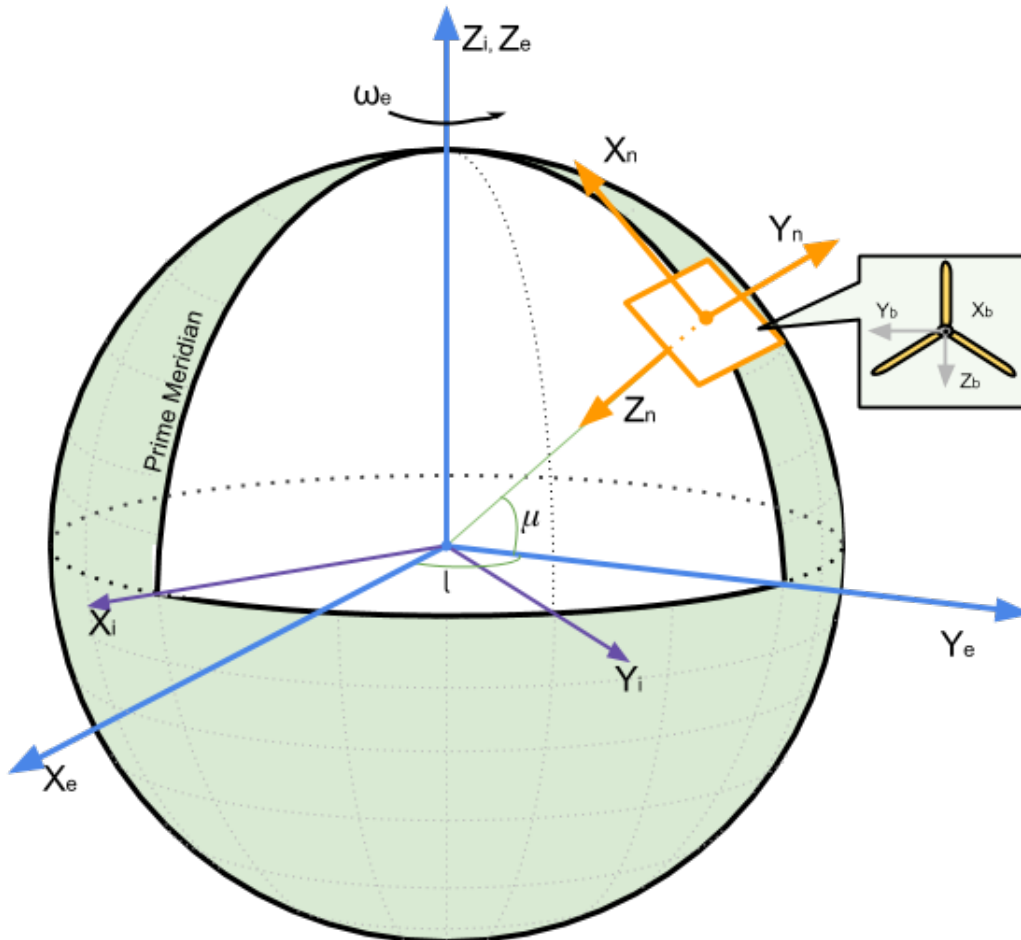


Figure 2.1: The Geodetic(l, μ, h), ECI(x_i, y_i, z_i), ECEF(x_e, y_e, z_e), NED(x_n, y_n, z_n) and body / Bird(x_b, y_b, z_b) coordinate systems.

NED: Local north-east-down reference frame $\{n\} = (x_n, y_n, z_n)$ is a local reference frame with origin O_n , often used to get better resolution of the area of interest. Its coordinate frame is fixed to the earth's surface, based on the World Geodetic System 84 (WGS84) ellipsoid. The z-axis points downwards perpendicular to the plane tangent to the ellipsoid, the x-axis points towards true north and the y-axis points towards east. Guidance and navigation are normally carried out in this frame. The location $\{n\}$ relative to $\{e\}$ determined by the longitude and latitude. For a vehicle operating in a local area, approximately constant longitude and latitude, can we assume $\{n\}$ as inertial, so that newtons laws apply.

It is also worth mentioning that we also have a vehicle carried NED frame. This reference frame is associated with the moving vehicle. However, operations in small regions with low speed result in that the directional difference being completely neglectable. Which is the case for this thesis.

Body: The body reference frame $\{b\} = (x_b, y_b, z_b)$ is a local reference frame that is fixed to the vehicle at a predefined point on the vehicle. Where axes are usually chosen so that x_b points in the forward direction, y_b points to the right side and z_b points downward.

2.2 Attitude Representation

An object's orientation in the space it's in, can be described using several techniques. Euler angles, Gibbs vector, Euler-Rodrigues, rotations vector and quaternions just to mention a few. The most common being Euler angles and the more complex quaternions. Although the Euler angles is the most know and has obvious advantages of representing coordinate transformations and mathematical identities is the more complex quaternions a more preferable choice in attitude representation (Shuster, 1993). A small elaboration of Euler angles, the Unit quaternions the Gibbs vector is presented.

Firstly, a three-dimensional rigid body rotation can be described by a rotation matrix \mathbf{R} which is an element of the special orthogonal group of order 3, $SO(3)$. Where $SO(3)$ is defined

as

$$SO(3) := \{\mathbf{R} | \mathbf{R} \in R^{3 \times 3}, \mathbf{R}^T \mathbf{R} = \mathbf{I}, \det \mathbf{R} = 1\} \quad (2.1)$$

The group $SO(3)$ is a set of all orthogonal matrices of order 3.

2.2.1 Euler Angels

Euler angels is a widely used representation, providing the possibility of formulating attitude representations as a sequence of single axis rotations. Where Each parameters provide a intuitive representation of the single-axis rotation. For navigational purposes are these angels known as roll, pitch and yaw (written θ , ϕ and ψ , respectively) and represent the rotation around x-, y-, and z-axis respectively. The rotation matrix \mathbf{R} of these three simple rotations can be obtained by (Fossen, 2011)

$$\mathbf{R}_b^n(\Theta_{nb}) = \begin{bmatrix} \cos(\psi)\cos(\theta) & -\sin(\psi)\cos(\theta) + \cos(\psi)\sin(\theta)\sin(\phi) & \sin(\psi)\sin(\theta) + \cos(\psi)\sin(\theta)\cos(\phi) \\ \sin(\psi)\cos(\theta) & \cos(\psi)\cos(\theta) + \sin(\phi)\sin(\theta)\sin(\psi) & -\cos(\psi)\sin(\theta) + \sin(\theta)\sin(\psi)\cos(\theta) \\ -\sin(\theta) & \cos(\theta)\sin(\phi) & \cos(\theta)\cos(\phi) \end{bmatrix} \quad (2.2)$$

where $\Theta_{nb} = [\phi, \theta, \psi]$ is the Euler angles between the $\{b\}$ and $\{n\}$ frames. The Euler angels kinematics is found by (Fossen, 2011)

$$\dot{\Theta}_{nb} = \mathbf{T}_\Theta(\Theta_{nb})\omega_{b/n}^b \quad (2.3)$$

where

$$\mathbf{T}_\Theta(\Theta_{nb}) = \begin{bmatrix} 1 & \sin(\phi)\tan(\theta) & \cos(\phi)\tan(\theta) \\ 0 & \cos(\phi) & -\sin(\phi) \\ 0 & \sin(\phi)/\cos(\theta) & \cos(\phi)/\cos(\theta) \end{bmatrix} \quad \theta \neq \pm 90^\circ \quad (2.4)$$

and $\omega_{b/n}^b = [p, q, r]$ is the angular velocity of point O_b with respect to the $\{n\}$ frame represented in the $\{b\}$ frame. This representation is non-global as it introduces singularities for $\theta \neq \pm 90^\circ$.

This is not unique for Euler angles but present in all other three-parameter representations (e.g. Rotation vector) (Shuster, 1993).

2.2.2 Unit Quaternions

Unit quaternions or Euler parameters presents another representation. Using four parameters to represent the rotation matrix instead of three. Avoiding the singularities associated with the three-parameter parameterizations.

The set of unit quaternions is defined as (Fossen, 2011)

$$Q := \{\mathbf{q} | \mathbf{q}\mathbf{q}^T = 1, \mathbf{q} = [\eta, \boldsymbol{\epsilon}^T]^T, \boldsymbol{\epsilon} \in \mathbb{R}^3 \text{ and } \eta \in \mathbb{R}\} \quad (2.5)$$

where $\eta := \cos(\beta/2)$ and $\boldsymbol{\epsilon} = [\epsilon_1, \epsilon_2, \epsilon_3]^T := \boldsymbol{\lambda} \sin(\beta/2)$ is the real scalar part and the imaginary vector part, respectively. Furthermore, β is the quaternion rotation angle and $\boldsymbol{\lambda} = [\lambda_1, \lambda_2, \lambda_3]^T$ a unit vector satisfying $\boldsymbol{\lambda} = \pm \boldsymbol{\epsilon} / \sqrt{\boldsymbol{\epsilon}\boldsymbol{\epsilon}^T}$ if $\sqrt{\boldsymbol{\epsilon}\boldsymbol{\epsilon}^T} \neq 0$. The rotation matrix represented using quaternions are defined as

$$\mathbf{R}_b^n(\mathbf{q}) := \mathbf{I}_{3 \times 3} + 2\eta\mathbf{S}(\boldsymbol{\epsilon}) + 2\mathbf{S}^2(\boldsymbol{\epsilon}) \quad (2.6)$$

where $\mathbf{S}(\bullet)$ is the skew symmetric matrix

$$\mathbf{S}(\boldsymbol{\epsilon}) = \begin{bmatrix} 0 & -\epsilon_3 & \epsilon_2 \\ \epsilon_3 & 0 & -\epsilon_1 \\ -\epsilon_2 & \epsilon_1 & 0 \end{bmatrix} \quad (2.7)$$

Opposed to the three parameter, non-linear, Euler angle kinematics representation can the kinematics of the quaternion be found using a linear representation (Shuster, 1993). Where the kinematics can be seen as

$$\dot{\mathbf{q}} = \mathbf{T}_q(\mathbf{q})\boldsymbol{\omega}_{b/n}^b \quad (2.8)$$

where

$$\mathbf{T}_q(\mathbf{q}) = \frac{1}{2} \begin{bmatrix} -\epsilon_1 & -\epsilon_2 & -\epsilon_3 \\ \eta & -\epsilon_3 & \epsilon_2 \\ \epsilon_3 & \eta & -\epsilon_1 \\ -\epsilon_2 & \epsilon_1 & \eta \end{bmatrix} = \frac{1}{2} \begin{bmatrix} & -\boldsymbol{\epsilon}^T \\ \boldsymbol{\eta} \mathbf{I}_{3 \times 3} + \mathbf{S}(\boldsymbol{\epsilon}) & \end{bmatrix} \quad (2.9)$$

using [Fossen \(2011\)](#) representation, or by using the more compact notation of [Egeland and Gravdahl \(2002\)](#)

$$\dot{\mathbf{q}} = \frac{1}{2} \mathbf{q} \otimes \begin{bmatrix} 0 \\ \boldsymbol{\omega}_{b/n}^b \end{bmatrix} \quad (2.10)$$

where the quaternion product, \otimes is utilized, or alternatively using

$$\dot{\mathbf{q}} = \frac{1}{2} \boldsymbol{\Omega}(\boldsymbol{\omega}_{b/n}^b) \mathbf{q} \quad (2.11)$$

where $\boldsymbol{\Omega}(\boldsymbol{\omega}_{b/n}^b)$ are defined by the 4D skew symmetric matrix

$$\boldsymbol{\Omega}(\boldsymbol{\omega}_{b/n}^b) = \begin{bmatrix} 0 & -\boldsymbol{\omega}_{b/n}^b \\ \boldsymbol{\omega}_{b/n}^b & -\mathbf{S}(\boldsymbol{\omega}_{b/n}^b) \end{bmatrix} \quad (2.12)$$

Advantages using the quaternion product can also be utilized in performing successive rotations of multiple quaternions ([Egeland and Gravdahl, 2002](#)). Given an arbitrary three-dimensional column vector \mathbf{v} , can (2.6) be written as

$$\begin{bmatrix} 0 \\ \mathbf{Rv} \end{bmatrix} = \mathbf{q} \otimes \begin{bmatrix} 0 \\ \mathbf{v} \end{bmatrix} \otimes \mathbf{q}^{-1} \quad (2.13)$$

where \mathbf{q}^{-1} is the inverse unit quaternion, defined as the quaternion conjugate $\mathbf{q}^{-1} = [\eta, -\boldsymbol{\epsilon}]^T$. We also have the quaternion corresponding to the rotation identity matrix, $\mathbf{q}_{id} = [1, \mathbf{0}]^T$. Further-

more, the quaternion product of two unit quaternions is a unit quaternion (2.14)

$$\mathbf{q} := \mathbf{q}_1 \otimes \mathbf{q}_2 = \begin{bmatrix} \eta_1 \eta_2 - \boldsymbol{\epsilon}_1^T \boldsymbol{\epsilon}_2 \\ \eta_1 \boldsymbol{\epsilon}_2 + \eta_2 \boldsymbol{\epsilon}_1 + \mathbf{S}(\boldsymbol{\epsilon}_1) \boldsymbol{\epsilon}_2 \end{bmatrix} \quad (2.14)$$

In practice, may numerical integration of the quaternion introduce accumulated of numerical *round-off errors*, which may affect the orthogonality of the rotation matrix. Where the deviation of the rotation matrix orthogonality can be seen as the \mathbf{q} length deviation from unity (Shuster, 1993). Normalization procedures may help with such errors. For instance by direct normalization (2.15) (Egeland and Gravdahl, 2002). Seen Section 6.1 for more on numerical integration of the quaternion.

$$\mathbf{q} = \frac{\mathbf{q}}{\sqrt{\mathbf{q}^T \mathbf{q}}} \quad (2.15)$$

2.2.3 Gibbs Vector

The Gibbs vector or Rodrigues parameters is closely related to the quaternion, and can be seen as a gnomonic projection¹ of the quaternion space onto the three-dimensional euclidean space (Markley, 2003). Where the three parameters are defined as follows

$$\mathbf{g} = \frac{\boldsymbol{\epsilon}}{\eta} = \frac{\lambda \sin(\beta/2)}{\cos(\beta/2)} = \lambda \tan\left(\frac{\beta}{2}\right) \quad (2.16)$$

The rotation matrix has the following Gibbs representation

$$\mathbf{R}_b^n(\mathbf{g}) = \mathbf{I}_{3 \times 3} + \frac{2}{1 + |\mathbf{g}|^2} [\mathbf{S}(\mathbf{g}) + \mathbf{S}^2(\mathbf{g})] \quad (2.17)$$

The Gibbs vector become infinite for $\beta = \pi$, meaning that 180° rotations cannot be represented. However, this infinite representation are beneficial in error representation, e.g in MEKF to obtain better margins for large attitude errors (Markley, 2003).

¹Gnomonic projection. Each surface point of the sphere is projected onto the tangent plane through the center of the sphere to the tangent plane (WIKIPEDIA, 2015)

2.2.4 Topological Obstructions and Unwinding

A important issue to consider when working with attitude estimation as well as attitude control, is problem of locally defined parameterizations in estimation/control schemes.

The Euler rotation matrix are the subject to six constraints, while the unit quaternions have one constraint, see the above sections. The Euler angles introduce topological obstructions, singularities for certain orientations, while the unit quaternions enables two different representations, with opposite signs, of the same orientation.

Using unit quaternion to enlighten this issue, can it be shown that a global result is not possible with this local parametrization (Bhat and Bernstein, 2000). Although the unit quaternion $\mathbf{q} = [\eta, \mathbf{0}]^T$ and $\mathbf{q} = [-\eta, \mathbf{0}]^T$ represent the same physical orientation, are these not mathematically equivalent. $\mathbf{q} = [-\eta, \mathbf{0}]^T$ represent a unstable equilibria, while $\mathbf{q} = [\eta, \mathbf{0}]^T$ a stable equilibria. Meaning that a estimate initially close to $\mathbf{q} = [-\eta, \mathbf{0}]^T$ would diverge and then converge to the $\mathbf{q} = [\eta, \mathbf{0}]^T$. In a attitude determination case, could this mean that attitude estimate exhibit errors up to 360° . This phenomena are called *unwinding*, and is present in all SO(3) designed attitude or control problems. Consequently, leading to unnecessary motion and increased wear and tear on the vehicle actuators.

2.3 Coordinate Transformation

Some relevant coordinate transformation are seen in the current section. (Fossen, 2011).

Geodetic and ECEF: The positions given by the GPS are most often provided as ellipsoidal coordinates (latitude, longitude and height) based on the World Geodetic System 84 (WGS84) ellipsoid. In order to convert the GPS measurements to NED do we first need an intermediate

step converting GPS to ECEF. This can be done in the following way

$$\mathbf{p}_{b/e}^e = \begin{bmatrix} x_e \\ y_e \\ z_e \end{bmatrix} = \begin{bmatrix} (N_E + h) \cos(\mu) \cos(l) \\ (N_E + h) \cos(\mu) \sin(l) \\ [N_E(1 - e^2) + h] \sin(\mu) \end{bmatrix} \quad (2.18)$$

where e is the eccentricity of the ellipsoid and $N_E = r_e^2 / \sqrt{r_e^2 \cos^2(\mu) + r_p^2 \sin^2(\mu)}$ is the prime vertical radius of the curvature, where r_e is the semi-major axis and r_p is the semi-minor axis of the ellipsoid.

ECEF and NED: The position transformation from NED to ECEF are defined as follows

$$\mathbf{v}_{b/e}^e = \dot{\mathbf{p}}_{b/e}^e = \mathbf{R}_n^e(\Theta_{ne}) \dot{\mathbf{p}}_{b/e}^n \quad (2.19)$$

where $\mathbf{p}_{b/e}^n$ is the position of the point O_b with respect to the $\{e\}$ -frame represented in the $\{n\}$ -frame, $\Theta_{ne} = [l, \mu]^T$ and the rotation matrix between ECEF to NED are

$$\mathbf{R}_n^e(\Theta_{ne}) = \begin{bmatrix} -\cos(l) \sin(\mu) & -\sin(\mu) & -\cos(l) \cos(\mu) \\ -\sin(l) \sin(\mu) & -\cos(\mu) & -\sin(l) \cos(\mu) \\ \cos(\mu) & 0 & -\sin(\mu) \end{bmatrix} \quad (2.20)$$

and $\mathbf{p}_{b/e}^e$ can be found by integrating 2.19.

Geodetic and NED: The relationship between geodetic position and NED, where the geodetic position and the NED velocity are of great interest.

$$\begin{bmatrix} \dot{l} \\ \dot{\mu} \\ \dot{h} \end{bmatrix} = \begin{bmatrix} \frac{v_n}{(N_E + h) \cos(\mu)} \\ \frac{u_n}{M_E + h} \\ -w_n \end{bmatrix} \quad (2.21)$$

The derivatives of the NED velocities are then given as

$$\mathbf{V}_{b/n}^n = \begin{bmatrix} \dot{u}_n \\ \dot{v}_n \\ \dot{w}_n \end{bmatrix} = \begin{bmatrix} -\frac{v_n^2 \sin(\mu)}{(N_E+h)\cos(\mu)} + \frac{u_n w_n}{M_E+h} + a_{mx_n} \\ \frac{u_n v_n \sin(\mu)}{(N_E+h)\cos(\mu)} + \frac{u_n w_n}{N_E+h} + a_{my_n} \\ -\frac{v_n^2}{(N_E+h)} - \frac{u_n^2}{M_E+h} + g + a_{mz_n} \end{bmatrix} \quad (2.22)$$

where g is the gravitational constant and $\mathbf{a}^n = [a_{mx_n}, a_{my_n}, a_{mz_n}]^T$ is the projection of $\mathbf{a}^b = [a_{mx_b}, a_{my_b}, a_{mz_b}]^T$ (the acceleration measured on the body) onto the vehicle carried NED. The acceleration \mathbf{a}^b can typically be measured by a three-axis accelerometer, assuming that the center of origin (CO) of the accelerometer coincide with the center of gravity of the vehicle. However, in the case where accelerometer origin does not coincide with the CG, transformation is needed.

Body and NED: The kinematic relation between body and NED, this relationship is important in modeling and control of a vehicle. This relation can be viewed in Section 2.2, using different attitude representation.

2.4 Kinematics and Kinetics

Assuming that Bird is rigid and that the $\{n\}$ -frame is inertial, my the attitude kinematics of the system be represented trough rotation matrix between the $\{b\}$ -frame and the $\{n\}$ -frame. Where kinematics of \mathbf{R}_b^n can be described in the following way

$$\dot{\mathbf{R}}_b^n = \mathbf{R}_b^n \mathbf{S}(\boldsymbol{\omega}_{b/n}^b) \quad (2.23)$$

and \mathbf{R}_b^n satisfies (2.1). Moreover, based on the chosen attitude parametrization do rotation matrix take different forms (Section 2.2). Also recall that $\boldsymbol{\omega}_{b/n}^b$ represent the angular velocity of $\{b\}$.

In addition to the regular reference frames described in Section 2.1 do the Bird system have multiple local reference frames. Namely the $\{bird\}$, $\{wing\}$, $\{IMU\}$ frame, see Figure 2.2. This means that a small rewriting of (2.23) is needed. For notational purposes are the kinematics now

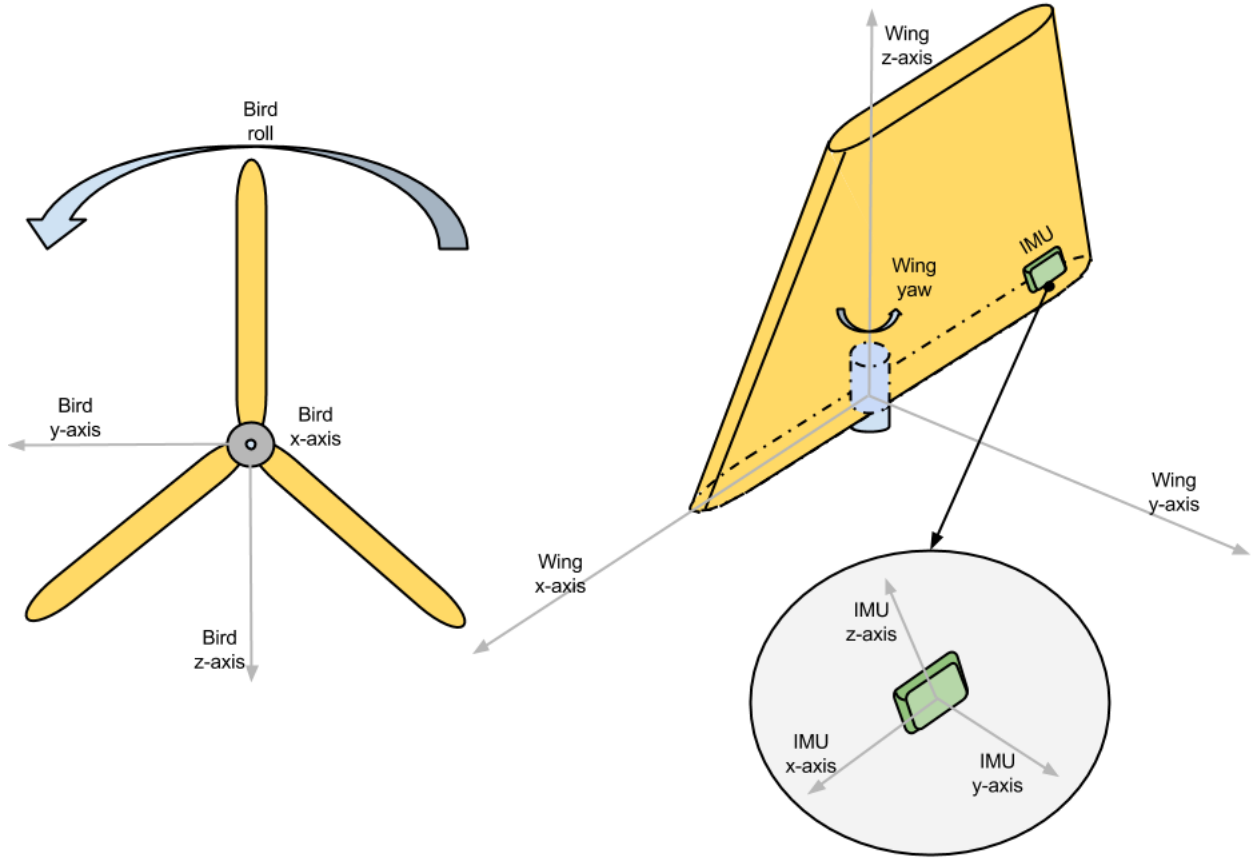


Figure 2.2: Illustration sketch of the steering device, including frame conventions and placement. The overall steering unit are seen to the left, while on of the steering wings including the inertial measurement unit are viewed to the right

represented with alternative representation

$$\dot{\mathbf{R}}_{wing}^n = \mathbf{S}(\omega_{wing/n}^n) \mathbf{R}_{wing}^n \quad (2.24)$$

where

$$\mathbf{R}_{wing}^n = \mathbf{R}_{bird}^n \mathbf{R}_{wing}^{bird} \quad (2.25)$$

$$\omega_{wing/n}^n = \omega_{bird/n}^n + \mathbf{R}_{bird}^n \omega_{wing/bird}^{bird} \quad (2.26)$$

Although this may be a small over-representation for the attitude estimation scheme - from $\{n\}$

to $\{wing\}$ attitude determination - are it convenient for modeling and simulation purposes. The (2.23) representation would be sufficient (or the quaternion representation in Section 2.2.2) for attitude estimation.

As for the translational motion of the system can we assume that $\dot{\mathbf{v}}_{bird/n}^n \approx \mathbf{0}$ and that $\dot{\mathbf{v}}_{wing/n}^n$ are governed by the centripetal acceleration in the following way

$$\dot{\mathbf{v}}_{wing/n}^n = \dot{\mathbf{v}}_{bird/n}^n + (\mathbf{S}(\boldsymbol{\omega}_{bird/n}^n) + \mathbf{S}(\boldsymbol{\omega}_{bird/n}^n)^2) \mathbf{r}_{wing}^{bird} \quad (2.27)$$

$$= \mathbf{S}(\boldsymbol{\omega}_{bird/n}^n)^2 \mathbf{r}_{wing}^{bird} \quad (2.28)$$

where \mathbf{r}_{wing}^{bird} are the level arm and $\boldsymbol{\omega}_{bird/n}^n$ bird angular velocity, the transversal acceleration are neglected.

Chapter 3

Attitude Observers

The studied attitude observers and their concepts will be presented in the current section. As the system currently are unable to use aiding measurements (e.g velocity). Will the focus of the presented observers lie on observers capability of handling only inertial measurements. This includes the linear mapping and magnetometer tilt compensation method, the MEKF, QUEST and the non-linear attitude observers of [Grip et al. \(2015\)](#), [Batista et al. \(2014b\)](#), the angular velocity observer of [Magnis and Petit \(2015b\)](#) and the author developed attitude observer.

For further details relating the implementation of these observer see [Chapter 7](#).

3.1 Linear Acceleration Mapping and Magnetometer Tilt Compensation

Assuming that static inertial reference frame. Can the linear mapped acceleration from a IMU be used to obtain the roll and pitch angles estimates (Fossen, 2011)¹

$$\begin{aligned}\phi &= \operatorname{atan}\left(\frac{a_y}{a_z}\right) \\ \theta &= -\operatorname{atan}\left(\frac{a_x}{\sqrt{a_y^2 + a_z^2}}\right)\end{aligned}\quad (3.1)$$

Using the ϕ and θ estimates in a magnetometer tilt compensating manner, can the yaw angle be determined from the horizontal components of the magnetometer.

$$\psi = \operatorname{atan}\left(\frac{h_y}{h_x}\right)\quad (3.2)$$

where the horizontal components are

$$h_y = m_y \cos(\phi) - m_z \sin(\phi)\quad (3.3)$$

$$h_x = m_x \cos(\theta) + m_y \sin(\phi) \sin(\theta) + m_z \cos(\phi) \sin(\theta)\quad (3.4)$$

It should be noted that the sign of the horizontal components should be taken into consideration. For further details on this see Fossen (2011). The yaw angles can also be determined using gyroscope measurements using a similar approach (Vik, 2014).

Variation of the earth magnetic field must be taken into considered using such a method. Since the earth magnetic poles and the earth's axis of rotation is shifted, and are not at the same geographical localization. This creates differences between the true north and the magnetic north. This difference, called the declination angle, d , is dependent on the localization of the magnetic measurements. The declination angle can be obtained using the World Magnetic Model (WMM)([Ngdc.noaa.gov](http://ngdc.noaa.gov), 2015b) or equivalent models. The geographical heading

¹atan is the inverse tangent function

can then be found by

$$\psi = \text{atan}\left(\frac{h_y}{h_x}\right) \pm d \quad (3.5)$$

where the declination angle is either added or subtracted depending whether you have a western or eastern longitude, respectively.

This linear mapping of measurements, can further be used in more complex observer methods. For instance by using quaternions and complementarity filtering to estimate the attitude (Fossen, 2011). However, because of the sub-system structure of such an approach, would it not be beneficial to do this in practice. As significant computational errors sources may be induced (Mahony et al., 2008).

It should also be noted that these mapping procedures are only applicable in a static environment. Dynamic behavior would introduce significant errors, as gravitational acceleration cannot be separated from induced body acceleration. Another source of error using this approach are noise characteristics of the measurements, and how well-conditioned² the attitude resolution are.

3.2 QUEST - QUaternion ESTimator

The QUaternion ESTimator (QUEST), based on Wahblas' problem (Wahba, 1965), uses quaternions and its properties to find the optimal quaternion describing the attitude. Wahbla's problem consist of finding a proper orthogonal matrix, \mathbf{A} , that minimizes function the

$$\mathbf{J}(\mathbf{A}) = \frac{1}{2} \sum_{i=1}^N a_i |\mathbf{W}_i - \mathbf{A}\mathbf{V}_i|^2 \quad (3.6)$$

²How well-conditioned - or alternatively ill-conditioned - the attitude resolution are, depends on how close or alternatively how separated the measurement vectors (eg. magnetic and gravitational) used in the attitude determination are. Also see Grip et al. (2012b); Mahony et al. (2008); Hua et al. (2014a) and references therein, for further discussion on the subject

where \mathbf{W}_i is a set of unit vectors measured in the $\{b\}$ -frame, \mathbf{V}_i the corresponding unit vectors in the reference frame (e.g $\{n\}$) and a_i non-negative scalar weighting operators. The QUEST method builds on the q-method of P. Davenport (1968) (this work was never published (Shuster, 2006)), and was first introduced by Shuster and Oh (1981). Rewriting the Wahblas' cost function

$$\mathbf{J}(\mathbf{A}) = \lambda_0 - \text{trace}(\mathbf{AB}) \quad (3.7)$$

where

$$\lambda_0 = \sum_{i=1}^N a_i \quad B = \sum_{i=1}^N a_i \mathbf{W}_i \mathbf{V}_i \quad (3.8)$$

making the minimization problem of the cost function (3.6) to a maximization problem of $\text{trace}(\mathbf{AB})$. Utilizing this rewriting of Wahbla's problem has many methods (see Markley and Mortari (2000) for multiple variations) been developed in order to solve Wahbla's problem. The QUEST based solution uses this structure to find an optimal quaternion that maximizes $\text{trace}(\mathbf{AB})$. One of the advantages of QUEST is that it do not depend on initial conditions. QUEST is also well-known as a fast attitude estimation algorithm (Shuster, 2006), utilizing only the vector measurements of a single time-step. This is also one of the disadvantages of the method. Because it will be very sensitive to measurement noise and do not include any additional filtering. For details on the algorithm and it chosen implementation method, there are several, see Section 7.2

3.3 MEKF

The Kalman filter and its extensions has for decades been used as the industry standard for estimation purposes. In light of this will considerations using the Kalman filter for state-estimation be used. However, mainly as a estimation benchmark for the other more lightweight non-linear observers. The MEKF uses a quaternion representation, Section (2.2), to estimate the attitude quaternion, \mathbf{q} , and the gyro sensor bias, \mathbf{b} . Where the quaternion error govern the quaternion update. Moreover, due to the constraint on the quaternion would an full representation of the quaternion lead to singularities in the Kalman covariance matrix. Which again would make the

filter unstable. The reason being accumulation of round-off errors in an implemented numerical filter (Shuster, 1993). One method handling this is to reduce dimension of the four parameter quaternion error (3.9), using only the quaternions vector part, $\delta\boldsymbol{\epsilon}$, in the error representation.

$$\delta\mathbf{q} = \begin{bmatrix} \delta\eta \\ \delta\boldsymbol{\epsilon} \end{bmatrix} = \hat{\mathbf{q}}^{-1} \otimes \mathbf{q} \quad (3.9)$$

Making the state vector of the filter

$$x = \begin{bmatrix} \delta\boldsymbol{\epsilon} \\ \mathbf{b} \end{bmatrix} \quad (3.10)$$

which results in that the covariance matrix, \mathbf{P} , and the other Kalman matrices, \mathbf{K} and \mathbf{H} are described without singularities (Shuster, 1993).

There are multiple parameterizations handling this three parameter representation of the quaternion error and the update of the quaternion estimate (Markley, 2003). Among others

$$\hat{\mathbf{q}} = \bar{\mathbf{q}} \otimes \begin{bmatrix} \sqrt{1 - \|\delta\boldsymbol{\epsilon}\|^2} \\ \delta\boldsymbol{\epsilon} \end{bmatrix} \quad (3.11)$$

which is the unit quaternion representation and the most common representation. Or alternatively twice of the Gibbs vector, which provide advantage of first defining the unnormalized quaternion error and then normalizing it

$$\boldsymbol{\rho} = \bar{\mathbf{q}} \otimes \begin{bmatrix} 2 \\ \delta\mathbf{g} \end{bmatrix} \quad \hat{\mathbf{q}} = \frac{\boldsymbol{\rho}}{\sqrt{\boldsymbol{\rho}^T \boldsymbol{\rho}}} \quad (3.12)$$

It is important to note that the quaternion update must have same parametrization as the quaternion error. To be more specific do this mean that the unit quaternion parametrization would have the error representation in (3.9) with the quaternion update of (3.11). The Gibbs vector

representation would have the error

$$\delta \mathbf{g} = 2 \frac{\delta \boldsymbol{\epsilon}}{\delta \eta} \quad (3.13)$$

and the quaternion update of (3.12).

The advantage of using the Gibbs vector also come in handy when the largest possible attitude errors occur, 180° rotation. Leading to an infinite Gibbs vector - scalar part becomes zero, see Section 2.2.3 and (3.13). Using the more common representation (3.11), would make the quaternion error norm equal to 2 under such situations. Leading to an unsensible quaternion reset and large quaternion estimate errors (Markley, 2003).

When it comes to the state innovation of the MEKF, is this done on the premises that $\delta \boldsymbol{\epsilon}$ in (3.10) is identically zero. Meaning that the innovation of the state between measurements do that modify the covariance. Resulting in that the covariance matrix do not become singular Markley (2003).

See Section 7.3 for further details on the measurement model, update and propagation procedures.

3.4 Observer Using Single Vector Measurements

The possibility of estimating the attitude using only a single vector measurement would be beneficial in the case of this thesis. The reason being magnetic distortion in the magnetic measurements, as well avoiding the need of magnetometer calibration.

Batista et al. (2012a) introduced a globally exponentially stable observer using a single vector observation. However, the gyro accumulating and bias drift where not considered. Recently have the same author introduced two companion papers, Batista et al. (2014a) and Batista et al. (2014b), that consider this slowly varying error. This by separately estimating that earth velocity expressed in $\{body\}$ -frame. The Batista et al. (2014b) paper will be considered here. Although, this method only introduce semi-global results, because of the $SO(3)$ design (see Section 2.2.4),

are the main interest the ability to estimate the attitude using only a single vector measurement. Additionally, projection methods enabling $SO(3)$ estimates can be avoided.

A preliminary assumption made, are that obtained measurements of angular velocity measurements are given by a high-grade rate gyros. Making the gyro measurement model

$$\boldsymbol{\omega}_m^b = \boldsymbol{\omega}^b + \boldsymbol{\omega}_e^b \quad (3.14)$$

where $\boldsymbol{\omega}_e^b$ are the angular velocity of the earth, expressed in $\{b\}$ -frame. Further, assuming that we have the knowledge of a constant reference vector in inertial-frame, the earth's angular velocity in inertial-frame is known and the reference vector and angular velocity i co-linear. Moreover, the angular velocity and angular acceleration in the $\{body\}$ -frame is bounded. See assumption [B.1](#) and [B.3](#) in Appendix B.

Then as the plurality of non-linear attitude estimation methods (e.g [Mahony et al. \(2008\)](#); [Grip et al. \(2011\)](#)), can we obtain an estimate of the angular velocity error using two vectors. However, here with one real and one artificial. The artificial vector are estimated through a auxiliary observer. Where the artificial, or auxiliary, vector are defined as

$$\mathbf{v}^b(t) := \mathbf{a}^b(t) \times [\mathbf{a}^b(t) \times \boldsymbol{\omega}_e^b(t)] \quad (3.15)$$

where $\mathbf{a}^b(t)$ is the measured vector in the $\{body\}$ -frame and $\boldsymbol{\omega}_e^b(t)$ the angular velocity of the earth. The counterpart in the inertial frame are defined as

$$\mathbf{v}^n := \mathbf{a}^n \times [\mathbf{a}^n \times \boldsymbol{\omega}_e^n] \quad (3.16)$$

where relationship between (3.15) and (3.16) are obtained by the rotation matrix \mathbf{R}_b^n . \mathbf{v}^n is constant and known, where $\boldsymbol{\omega}_e^n$ represent the angular velocity of the earth around it own axis.

Using (2.23), (3.14) and the rotation matrix relationship, can the dynamics of the measured

vector and the auxiliary vector be seen as

$$\dot{\mathbf{a}}^b = -\mathbf{S} \left[\boldsymbol{\omega}^b - \boldsymbol{\omega}_e^b \right] \mathbf{a}^b \quad , \quad \dot{\mathbf{v}}^b = -\mathbf{S} \left[\boldsymbol{\omega}^b - \boldsymbol{\omega}_e^b \right] \mathbf{v}^b \quad (3.17)$$

Furthermore, using the orthogonal basis in assumption B.1 can the angular velocity of the earth, in $\{b\}$, be written

$$\boldsymbol{\omega}_e^b = c_1 \mathbf{a}(t) - c_2 \mathbf{v}(t) \quad (3.18)$$

where

$$c_1 := \frac{\boldsymbol{\omega}_e^n \cdot \mathbf{a}^n}{\|\mathbf{a}^n\|^2} \quad , \quad c_2 := \frac{\|\mathbf{a}^n \times \boldsymbol{\omega}_e^n\|^2}{\|\mathbf{a}^n \times (\mathbf{a}^n \times \boldsymbol{\omega}_e^n)\|^2} \quad (3.19)$$

Applying these results to design a auxiliary observer and a attitude observer using (2.8), (3.14) do Batista et al. (2014b) prove semi-global results. This without the assumption of persistent-excitation (PE), see Definition B.4 in Appendix B, which are common assumption for attitude estimation using a single vector observation. For details on the actual estimation scheme see Section 7.4

3.5 Globally Exponentially Stable Observer

As described in Section 2.2.4 may attitude estimations confined to $SO(3)$ induce topological obstructions and unwinding. On the contrary, representing the attitude estimation by a full nine parameter, unconstrained, rotation matrix solves this problem (Grip et al., 2015; Batista et al., 2014a, 2011). Although this matrix not necessary guaranteed to belong to $SO(3)$, which is in-fact wanted, can either projection method's (Batista et al., 2011) or algebraic a formula (Grip et al., 2015) be utilized to make the estimates converge to $SO(3)$. The method of Grip et al. (2015) will be considered here.

Under the assumption of a constant gyro bias, see Assumption B.2, and making the used of Assumption B.1, a common non-linear attitude estimation assumption, do Grip et al. (2015)

construct the orthogonal basis

$$\mathbf{A}^n(t) = \begin{bmatrix} \frac{\mathbf{a}^n}{\|\mathbf{a}^n\|} & \frac{\mathbf{S}(\mathbf{a}^n)\mathbf{m}^n}{\|\mathbf{S}(\mathbf{a}^n)\mathbf{m}^n\|} & \frac{\mathbf{S}^2(\mathbf{a}^n)\mathbf{m}^n}{\|\mathbf{S}^2(\mathbf{a}^n)\mathbf{m}^n\|} \end{bmatrix} \quad (3.20)$$

$$\mathbf{A}^b(t) = \begin{bmatrix} \frac{\mathbf{a}^b}{\|\mathbf{a}^b\|} & \frac{\mathbf{S}(\mathbf{a}^b)\mathbf{m}^b}{\|\mathbf{S}(\mathbf{a}^b)\mathbf{m}^b\|} & \frac{\mathbf{S}^2(\mathbf{a}^b)\mathbf{m}^b}{\|\mathbf{S}^2(\mathbf{a}^b)\mathbf{m}^b\|} \end{bmatrix} \quad (3.21)$$

when two vector measurements are available to design a Globally Exponentially Stable (GES) attitude observer with gyro bias estimation. Where the attitude estimate are governed by (2.23), with the injection term

$$\mathbf{J}(t, \hat{\mathbf{R}}) = \left(\mathbf{A}^n(t) - \hat{\mathbf{R}}\mathbf{A}^b(t) \right) \mathbf{A}^b(t)^T \quad (3.22)$$

and an adaptive projection³ method for gyro bias estimation. The adaptive parameter projection $\text{PROJ}(\cdot, \cdot)$ are defined as:

$$\text{Proj}(\hat{\mathbf{b}}, \beta) = \begin{cases} \left(\mathbf{I} - \frac{c(\hat{\mathbf{b}})}{\|\hat{\mathbf{b}}\|^2} \hat{\mathbf{b}}\hat{\mathbf{b}}^T \right) \beta, & \|\hat{\mathbf{b}}\| \geq \mathbf{M}_b, \quad \hat{\mathbf{b}}^T \beta > 0 \\ \beta, & \text{otherwise} \end{cases} \quad (3.23)$$

where

$$c(\hat{\mathbf{b}}) = \min \left(1, \frac{\|\hat{\mathbf{b}}\|^2 - \mathbf{M}_b^2}{\mathbf{M}_b^2 - \mathbf{M}_b^2} \right) \quad (3.24)$$

This is a special case of the gradient projection algorithm, where the adoption gain are $\Gamma = \beta$, where β is a scalar value.

As stated above, do the attitude estimate using this approach not necessary provide estimates that belong to $SO(3)$. If $SO(3)$ estimates are needed do [Grip et al. \(2015\)](#) proposes to use

³Projection is a method of guaranteeing a bounded parameter estimate.

the algebraic formula

$$\begin{aligned}\bar{\mathbf{R}}(\hat{\mathbf{R}}) &= [\bar{r}_2 \quad \bar{r}_1 \quad \mathbf{S}(\bar{r}_1)\bar{r}_2] \\ \bar{r}_1 &= \frac{\hat{r}_1}{\max(\|\hat{r}_1\|, \mu)} \\ \bar{r}_2 &= \frac{(\mathbf{I} - \bar{r}_1 \bar{r}_1^T)\hat{r}_2}{\max(\|(\mathbf{I} - \bar{r}_1 \bar{r}_1^T)\hat{r}_2\|, \mu)}\end{aligned}\tag{3.25}$$

making the estimates converge to $SO(3)$. The convergence transient of these estimates depends on the tuning of the observer and the choice of μ , where $\mu \in (0, 1)$ are a small constant. \hat{r}_1 and \hat{r}_2 are the first and second column of the estimated matrix \mathbf{R} .

The complete observer algorithm and further details can be seen in Section 7.5.

3.6 Angular Velocity Observer

Opposed to the above observers, which estimates the attitude of the rigid body by employing vector measurements and rate gyros, do this section introduce a observer that estimates the angular velocity. These estimates could then be fed through (2.23) to describe the attitude. The main motivation behind this approach are the relatively noisy and drifting property of the rate gyros, making attitude determination noisy and a demanding task.

Utilizing Assumption B.1 and B.3 in Appendix B, and by assuming the knowledge of the inertia matrix and the external forces action on the rigid body have Magnis and Petit (2015b) recently proposed a fairly simple method of estimating the angular velocity. This by applying the kinematic relation described by (2.23) where the angular velocity are governed by

$$\dot{\boldsymbol{\omega}} = \mathbf{J}^{-1} (\mathbf{J}\boldsymbol{\omega} \times \boldsymbol{\omega} + \boldsymbol{\tau}) := \mathbf{E}(\boldsymbol{\omega}) + \mathbf{J}^{-1}\boldsymbol{\tau}\tag{3.26}$$

where $\mathbf{J} = \text{diag}(J_1, J_2, J_3)$ are the inertia matrix and $\boldsymbol{\tau}$ the external input torque. Moreover, by using two body fixed vector measurements and there constant counterparts in the inertial frame can an estimate $\hat{\boldsymbol{\omega}}$ of $\boldsymbol{\omega}$ be computed. See details in Section 7.6.

Also make note of that angular velocity estimation are also possible for a single vector ob-

servation under a certain PE condition (Magnis and Petit, 2015a).

Although the angular velocity observer of Magnis and Petit (2015b) is fairly simple in design, do it demand some a prior information to work. Namely the rigid body inertia matrix and the external torque. The inertia matrix can be calculated by using the physical properties of the bird. Whereas the knowledge of the input torque, τ , from the external disturbances are a more difficult task. This due to no direct measurement of τ , which is assumed by Magnis and Petit (2015a), are available for the current system. Nevertheless, making use foil and hydrodynamic theory could these forces be modelled. See Section 4.4 for further details.

3.7 Developed Attitude Observer

Motivated by the ability of estimating the angular velocity of the system using the approach of Magnis and Petit (2015b), are the author proposing a SO(3) attitude observer merging this approach with other known attitude estimation aspects. The Magnis and Petit (2015b) angular velocity observer has a locally exponential stable error dynamics, making $\hat{\omega} \rightarrow \omega$. However, substituting the angular velocity estimates into the kinematics (2.23) would not necessary lead to a correct - error free - attitude.

Attitude Error

Firstly, the goal of SO(3) attitude estimation are to obtain a estimate such that the attitude error $\tilde{\mathbf{R}} := \mathbf{R}\hat{\mathbf{R}} \rightarrow \mathbf{I}_3$. Where \mathbf{R} and $\hat{\mathbf{R}}$ are the true and estimated attitude matrix respectively. Further, the kinematics of attitude error, $\dot{\tilde{\mathbf{R}}}$, can be seen as (Mahony et al., 2008)

$$\dot{\tilde{\mathbf{R}}} = \dot{\mathbf{R}}\hat{\mathbf{R}}^T + \mathbf{R}\dot{\hat{\mathbf{R}}}^T = \mathbf{R}\mathbf{S}(\omega)\hat{\mathbf{R}}^T - \mathbf{R}\mathbf{S}(\omega)\hat{\mathbf{R}}^T = \mathbf{R}[\mathbf{S}(\omega) - \mathbf{S}(\omega)]\hat{\mathbf{R}}^T = \mathbf{0} \quad (3.27)$$

meaning that the attitude error $\tilde{\mathbf{R}}$ would be constant. However, using a injection or correction term would fix the problem of a constant attitude error. Recent literature presents a wide variety of such correction terms, see Mahony et al. (2008); Grip et al. (2013); Hua et al. (2014a) among

others. These papers presents methods using vector measurements to estimate the gyro bias and the attitude through $\dot{\hat{\mathbf{R}}}_b^n = \mathbf{RS}(\hat{\boldsymbol{\omega}} - \mathbf{b} + \sigma)$, where σ are the injection term and \mathbf{b} the gyro bias. Now since gyro bias aren't a problem using the angular velocity estimates obtained from [Magnis and Petit \(2015b\)](#), are only a injection term needed in order to obtain a error free attitude. The attitude estimate would then be obtained by

$$\dot{\hat{\mathbf{R}}}_b^n = \mathbf{R}_b^n \mathbf{S}(\hat{\boldsymbol{\omega}}^b + \sigma) \quad (3.28)$$

,resulting in the dynamics of the attitude error are found by $\dot{\hat{\mathbf{R}}} = -\mathbf{RS}(\sigma)\hat{\mathbf{R}}^T$.

Magnetic Disturbances and Coupling

Secondly, in a attitude estimation scheme is it usually desirable for magnetic measurements to only estimate the heading(yaw) of the system, and not the roll and pitch estimates. This could theoretically be done using the method in Section 3.1. However, this come with it's own problems.

Magnetic disturbances may be a concern in the thesis system, or in any practical application for that matter. Resulting in inaccurate magnetic measurements. Moreover, it is a known fact that there are a high coupling between roll, pitch and yaw angles. As a consequence would roll and pitch error estimates have a additional error effect on the yaw estimates. Using a injection term that decouples roll and pitch estimates from magnetic measurements would therefore be preferable. With this in mind have [Hua et al. \(2014a\)](#) designed a decoupling strategy that globally decouples the roll and pitch estimates from yaw and magnetic measurements.

The injection term are defined as

$$\sigma := k_1 \mathbf{u}^b \times \hat{\mathbf{R}}^T \mathbf{u}^n + k_2 \mathbf{u}^b \mathbf{u}^{bT} (\mathbf{v}^b \times \hat{\mathbf{R}}^T \mathbf{v}^n) \quad (3.29)$$

where the vectors \mathbf{u}^b and \mathbf{u}^n are the normalized acceleration in the body and inertial frame

respectively. \mathbf{v}^n and \mathbf{v}^b are auxiliary vectors , defined by

$$\mathbf{v}^n = \frac{\pi_{u^b} \bar{\mathbf{m}}^n}{\|\pi_{u^b} \bar{\mathbf{m}}^n\|}, \quad \mathbf{v}^b = \frac{\pi_{u^n} \bar{\mathbf{m}}^b}{\|\pi_{u^n} \bar{\mathbf{m}}^b\|} \quad (3.30)$$

where $\pi_x = \|\mathbf{x}\|^2 \mathbf{I}_{3 \times 3} - \mathbf{x} \mathbf{x}^T$ are the orthogonal projection of the vector \mathbf{x} onto the plan orthogonal to \mathbf{x} . Moreover, $\bar{\mathbf{m}}^n$ and $\bar{\mathbf{m}}^b$ represent the normalized magnetic field in the inertial and body frame respectively. k_1 and k_2 are positive constant tuning gains.

Moreover, the injection term (3.29) introduce the ability to use non-high gains - more robust - to obtain fast dynamics even for a ill-conditioned attitude problems (geomagnetic and gravitation vector are close to each other). Opposed to using the more standard injection term $\sigma = \sum_{j=1}^n k_j \mathbf{v}_j^b \times \mathbf{v}_j^n$, with $k_j > 0$, $j = 1, \dots, n$ representing scalar gains and \mathbf{v}_j^b , \mathbf{v}_j^n the body measured and inertial vectors, respectively (See Mahony et al. (2008); Grip et al. (2011, 2013) among others). Which would result in high gains for a ill-conditioned attitude problem - amplifying the measurement noise and uncertainties. See Appendix D for some additional results regarding this subject.

Stability

Knowing that the angular velocity observer of Magnis and Petit (2015b) are proven to be locally exponentially stable (LES) . Further, from part 2 of theorem 1 in Hua et al. (2014a) can we conclude that $\tilde{\mathbf{R}}$ are LES with the injection term (3.29). So, by combing these facts can it be stated that the attitude estimate is LES, with a globally decoupled roll and pitch estimate from yaw and magnetic measurements.

The observer are presented in full in Section 7.7.

Chapter 4

Sensors and Sensor Calibration

4.1 Sensors

The IMU provided in this system is a micro-electro-mechanical system (MEMS). The benefit and applications of the MEMS technology has gain strong interest the last decade. This due to the small size and low-cost of the MEMS technology. The signal output of a low-cost IMU system, however, is the subject to high noise levels and time-varying bias terms (Mahony et al., 2008). Models of the IMU sensors are presented in this section. The IMU model error model presented consist of a three-axis accelerometer, three-axis gyroscope and three-axis magnetometer and is based on the paper of Vik and Fossen (2000).

Generally will misalignment¹, scale-factors, biases and noise be factor in an IMU error model. Calibration procedures are always necessary and would enable reduction of these errors. See Section 4.2 for more on calibration.

A important factor to notice is that the measurement from a IMU is defined with opposite orientation as opposed to the inertial($\{n\}$) and the $\{b\}$ -frame. Meaning that the positive vertical axis are pointing upwards, not downwards (NED terminology). Furthermore, are the IMU sensor mounted to the $\{wing\}$ -frame coordinated system. This is situation is called a strapdown

¹Including psychical sensor axis misalignment and non-orthogonality between the sensor axis

system, since the IMU is strapped to the wing. Since the IMU is mounted with a lever arm with respect to the $\{wing\}$ -frame origin a transformation is needed. However, instead of transforming the measurements to the origin of $\{wing\}$ it is more preferable to do the state estimation in the measurement frame and then transform the estimated states to $\{wing\}$. This transformation is seen given as

$$\begin{bmatrix} \mathbf{v}_{wing/n}^{wing} \\ \boldsymbol{\omega}_{wing/n}^{wing} \end{bmatrix} = \begin{bmatrix} \mathbf{I}_{3 \times 3} & \mathbf{S}(\mathbf{r}_{IMU}^{wing}) \\ \mathbf{0}_{3 \times 3} & \mathbf{I}_{3 \times 3} \end{bmatrix} \begin{bmatrix} \mathbf{v}_{IMU/n}^{wing} \\ \boldsymbol{\omega}_{IMU/n}^{wing} \end{bmatrix} \quad (4.1)$$

where $\mathbf{r}_{IMU}^{wing} = [x_{IMU}, y_{IMU}, z_{IMU}]^T$ is the lever arm (Fossen, 2011).

4.1.1 Gyroscope

A gyroscope measures the angular velocity about the $\{IMU\}$ -frames axis, relative to the inertial frame. Measuring rapid changes in the attitude profile of the object it is attached to. This is generally done using multiple techniques - fiber optic gyro (FOG), a laser ring gyro (RLG) or the low cost MEMS technology. Integration of the measured angular velocity can be obtained in order to get the orientation of the object. However, due to sensor bias and drift which is present within all gyros' cannot the gyro be used single-handedly. Conjugating the gyro with other sensors must therefore always be conducted.

Gyro Error Model

The gyro output model can be seen as (Mahony et al., 2008)

$$\boldsymbol{\omega}_{imu} = \boldsymbol{\omega}_{b/n}^b + \mathbf{b}_{gyro} + \mathbf{w}_{gyro} \quad (4.2)$$

where \mathbf{b}_{gyro} represent the gyro bias and \mathbf{w}_{gyro} the sensor measurement noise. In addition should the misalignment and scale factors be included in the model. This can according to

Vik (2014) be done as follows

$$\boldsymbol{\omega}_{imu} = [\mathbf{I}_{3 \times 3} + \Delta(\boldsymbol{\kappa}, \boldsymbol{\alpha})] \boldsymbol{\omega}_{ib}^b + \mathbf{b}_{gyro} + \mathbf{w}_{gyro} \quad (4.3)$$

where

$$\Delta(\mathbf{s}, \boldsymbol{\phi}) = \begin{bmatrix} s_x & \phi_{xy} & \phi_{xz} \\ \phi_{yx} & s_y & \phi_{yz} \\ \phi_{zx} & \phi_{zy} & s_z \end{bmatrix} \quad (4.4)$$

and $\mathbf{s} = [s_x, s_y, s_z]^T$ and $\boldsymbol{\phi} = [\phi_{xy}, \phi_{xz}, \phi_{yx}, \phi_{yz}, \phi_{zx}, \phi_{zy}]^T$ is the scale-factors and misalignment angles, respectively. These errors models can be described through the first order models

$$\dot{\mathbf{b}}_{gyro} = -\mathbf{T}_1^{-1} \mathbf{b}_{gyro} + \mathbf{w}_2 \quad (4.5)$$

$$\dot{\boldsymbol{\kappa}} = -\mathbf{T}_2^{-1} \boldsymbol{\kappa} + \mathbf{w}_3 \quad (4.6)$$

$$\dot{\boldsymbol{\alpha}} = -\mathbf{T}_3^{-1} \boldsymbol{\alpha} + \mathbf{w}_4 \quad (4.7)$$

where \mathbf{w}_2 , \mathbf{w}_3 and \mathbf{w}_4 is Gaussian white noise, and \mathbf{T}_1 , \mathbf{T}_2 and \mathbf{T}_3 are diagonal time constants.

4.1.2 Accelerometer

Accelerometers measure the gravitational acceleration of the $\{IMU\}$ -frame and the object its attached to. In addition to the gravitational will also the centripetal, Coriolis and transversal acceleration be included in the measurements. There are several different types of accelerometers, among others pendulum, vibrating quartz and vibrating silicone. The quality of accelerometer measurement are very accurate. Even cheap accelerometers have errors below 10mg and an output range of $\pm 100g$ (Vik, 2014).

Accelerometer Error Model

The accelerometer model can be represented in the same manner - as the gyro error model - with respect to the misalignment and scale-factors (Vik, 2014). Using the IMU model of Mahony et al. (2008) the complete accelerometer model can be seen as

$$\mathbf{a}_{imu} = [\mathbf{I}_{3 \times 3} + \Delta(\epsilon, \beta)] \mathbf{R}_b^n(\Theta_{nb}) (\dot{\mathbf{v}}^n - \mathbf{g}^n) + \mathbf{b}_{acc} + \mathbf{w}_{acc} \quad (4.8)$$

where ϵ and β is the scale-factor and misalignment, respectively. \mathbf{b}_{acc} and \mathbf{w}_{acc} is the accelerometer bias and measurement noise, respectively. These errors will be modeled in a same fashion as in (4.5 - 4.7). Furthermore, $\mathbf{g}^n = [0, 0, 9.81]^T$ is the gravitational acceleration in $\{n\}$ and $\dot{\mathbf{v}}^n$ are the induced acceleration on the $\{IMU\}$ -frame in the $\{n\}$ -frame.

4.1.3 Magnetometer

A magnetometer measures the local magnetic field. Where the magnetic field represents the magnetic flux density. The magnetic flux density measured by a magnetometer will vary depending on the geographical localization of the measurements - the scale and direction of these measurements will vary. Near the equator, the magnetic field lines are almost parallel to the earth. However, traveling towards one of the poles will make the field lines direction point more straight into the earth. Another factor when using magnetic sensing is that the magnetic poles do not coincide with the geographical north, the magnetic poles are slightly shifted from the geographical. This difference is called magnetic declination angle, and can be used to shift between magnetic bearing or geographical bearing.

Using data from magnetic models such as the World Magnetic model (WMM) or the International Geomagnetic Reference Field (IGRF) the local magnetic field in $\{n\}$ can be calculated. These models provide a seven component description of the magnetic field based on the geographical localization on the earth and the distance above WGS84 ellipsoid (sea level). Among others the horizontal and vertical components and the declination angle. For surface navigational purposes, the WMM is the preferable choice. Since it is a more high resolution model,

including magnetic field contributions of the earth crust and so on (Ngdc.noaa.gov, 2015a).

Magnetic distortion and bias is a major concern in magnetic sensing. As other ferromagnetic material's influence the measurements. Permanent and non-changing components may be compensated for in calibration procedures. The time-varying on the other-hand is more difficult to handle. The motor in the wing and magnetic fields for the seismic cables would be such error sources.

Magnetometer Error model

The magnetic error model is modelled in the same fashion as gyro model in Section 4.1.1 with misalignment, scale and bias errors. The Magnetometer error model

$$\mathbf{m}_{imu} = [\mathbf{I}_3 + \Delta(\xi, \gamma)] \mathbf{R}_b^n(\Theta_{nb}) \mathbf{m}^n + \mathbf{b}_{mag} + \mathbf{w}_{mag} \quad (4.9)$$

where ξ and γ is the scale-factor and misalignment, respectively. \mathbf{b}_{mag} and \mathbf{w}_{mag} are the magnetometer bias and measurement noise, respectively. The local magnetic field \mathbf{m}^n in this thesis is retrieved from the WWM at Ngdc.noaa.gov (2015b).

4.2 Calibration

Calibration of the sensors is vital in practical applications. After installing the sensors in its operation device, many error sources have been introduced. Such as orientation misplacement and nearby objects inflicting the sensor measurements. Factory defects may also be present. These effects will then cause physical misalignment, scale-factors, biases and orthogonality errors ([Foster and Elkaim, 2008](#)). There are multiple methods of estimating these errors, both online or offline. However, the offline calibration theory goes out of the scope of this thesis, but calibration of the sensors are conducted in parallel to this thesis. A small elaboration on the calibration methods used is therefore included below. Moreover, online calibration - or at least quasi-online - calibration would be preferable for this system. A batch based quasi-online estimation method

are therefore presented.

Using an ellipsoid explanation can the bias calibration, so-called *hard-iron* calibration, be seen as the centering of the origin of the ellipsoid. The scale-factors as the scaling-size of the ellipsoid and the orthogonal misalignment as angles between the sensor x-, y- and z-axis and x-axis, x-z plane and y-z plane, respectively. The calibration of scale factors and orthogonal between axis is often called *soft-iron* calibration (Vasconcelos et al., 2011).

4.2.1 Offline Calibration

Offline accelerometer calibration can be done using a six-point tumble test. Rotating the accelerometer to get the positive and negative outer edges for each axis measurement, and comparing this to the known gravity direction. Batch measurements of gravity accelerations during rotation can then be used in a linear least-squares estimation procedure. Offline calibration of the acceleration in this thesis uses a high performance Motion Reference Unit (MRU) as gravity reference and an iterative least-squares estimation approach.

In order to calibrate a magnetometer precisely is the knowledge about magnetic direction important. Using for instance Helmholtz coils to produce the magnetic direction, can a known magnetic environment be created. The magnetic errors can then be calibrated in the same manner as the accelerometer. However, due to time-varying ferromagnetic object near the sensors in a practical application will an offline calibration only be valid to some extent - permanent and constant errors - for the purpose of this system, see further details in Section 4.3. The offline calibration in this thesis is done using a reference magnetometer, a tumble test and an iterative least-squares estimation. The tumble test, is done by applying positive and negative magnetic directions, produced by a three-axis Helmholtz coils, to the stationary IMU. Which is located inside the Helmholtz coils.

Gyro calibration can be done using a rotating rate table as reference. The rate table rotates with a known angular rate and the misalignment and scale factors can be calculated using linear or a non-linear model to get a more precise calibration. The gyro bias is a more difficult

task, this due to the time varying random walk component, so-called gyro bias drift, that cannot be compensated for using offline calibration procedures. On-line estimation techniques must therefore be used to compensate the gyro bias drift (Mahony et al., 2005).

Additionally to misalignment scale-factors and bias, will the IMU sensors outputs drift with the temperature. Hence, are temperature calibration or some kind of compensating for temperature changes needed.

4.2.2 Online Calibration

Calibration of the accelerometer and magnetometer under operation is preferable. Especially magnetometer calibration. The reason for this is that additional disturbances may have been introduced when the bird is mounted onto the seismic cables, plus that the time varying magnetic field from the motors will induce errors. A real-time attitude-independent magnetometer calibration method is presented by Crassidis et al. (2005), where a Kalman filter structure is utilized to estimate the bias, scale factors and orthogonal errors. However, processing limitations on the embedded system may be a problem.

Methods such as Alonso and Shuster (2002); Foster and Elkaim (2008); Vasconcelos et al. (2011) enables estimation of bias, scale factors and orthogonality errors. This through a batch of measurement data and a iterative least squares estimation. Performing these procedures sequentially would then make this a quasi online approach. Furthermore, this could also be done on a separate computer and thereafter be provide back to the bird embedded system.

Using a attitude independent model of the magnetic field can the Gauss-Newton method be applied iteratively to estimate the bias, scale factors and non-orthogonal errors (Alonso and Shuster, 2002; Vasconcelos et al., 2011) (Note that physical misalignment error are not incorporated. Calibration of such error requires a reference of some kind, see the previous section).

A common method to obtain an attitude independent calibration, are done by transposing

the terms in (4.9) and squaring the model, yielding

$$\|\mathbf{m}^n\|^2 = \|[\mathbf{I}_3 + \Delta(\xi, \gamma)]^{-1}(\mathbf{m}_{imu} - \mathbf{b} - \mathbf{w})\|^2 \quad (4.10)$$

Which can be seen as a distorted ellipsoid with a shifted origin. One approach is then to determine the algebraic coefficients of the ellipsoid quadratic surface described by (4.10), and thereafter algebraically compute the center, radii, rotation of the ellipsoid, see (Vasconcelos et al., 2011) and references therein. Or alternatively, using the completing of squares to obtain the quadratic form of (4.10) and determine these coefficient to obtain estimates of the centering, scale factors and non-diagonal elements describing the model, see Alonso and Shuster (2002) and references therein.

The method of Alonso and Shuster (2002) are utilized and described in short here. For notational purposes are some quantities first defined:

$$\boldsymbol{\theta} := [\mathbf{b}^T \quad \mathbf{D}^T]^T \quad (4.11)$$

$$\mathbf{D} := [\xi_x, \xi_y, \xi_z, \gamma_{xy}, \gamma_{xz}, \gamma_{yz}]^T \quad (4.12)$$

$$\mathbf{E} := 2\Delta(\xi, \gamma) + \Delta^2(\xi, \gamma) \quad (4.13)$$

$$\mathbf{c} := (\mathbf{I}_{3 \times 3} + \Delta(\xi, \gamma)) \mathbf{b} \quad (4.14)$$

$$\mathbf{K}_k := \left[m_{imu_x}^2, m_{imu_y}^2, m_{imu_z}^2, 2m_{imu_x}m_{imu_y}, 2m_{imu_x}m_{imu_z}, 2m_{imu_y}m_{imu_z} \right] \quad (4.15)$$

$$\mathbf{E} := [E_{11}, E_{22}, E_{33}, E_{12}, E_{13}, E_{23}]^T \quad (4.16)$$

where \mathbf{K}_k are seen as elements associated with the quadratic form of an general quadratic surface². Further, forming the attitude independent observation of the measurements through

$$y_k = \|\mathbf{m}_{imu}\|^2 - \|\mathbf{m}^n\|^2 = \mathbf{L}_k \boldsymbol{\theta}' - \|\mathbf{b}(\boldsymbol{\theta}')\|^2 + \mathbf{w} \quad (4.17)$$

²A general quadratic surface are described by $Ax^2 + By^2 + Cz^2 + Dxy + Exz + Fyz + Gx + Hy + Iz + J = 0$

where

$$\mathbf{L}_k = [2\mathbf{m}_{imu}^T \quad -\mathbf{K}_k] \quad (4.18)$$

$$\boldsymbol{\theta}' = [\mathbf{c}^T \quad \mathbf{E}^T]^T \quad (4.19)$$

can now a maximum likelihood estimation be utilized in order to determine the unknown parameters (\mathbf{b}, \mathbf{D}) . The Gauss-Newton method are chosen. Moreover, since model (4.17) are quadratic do we only need to provide the Jacobian³, \mathbf{J} , to preform a Guess-Newton estimation though

$$\hat{\boldsymbol{\theta}}'_{k+1} = \hat{\boldsymbol{\theta}}'_k + \alpha_k (\mathbf{J}_k^T \mathbf{J}_k)^{-1} \mathbf{J}_k r_k \quad (4.20)$$

where α_k is the step length and r_k the residual defined by

$$r_k = y_k - \hat{y}_k \quad (4.21)$$

\hat{y}_k holds the k estimate of (4.17). Moreover, assuming that Theorem 3.5 in [Nocedal and Wright \(2006\)](#) (Appendix B) is satisfied do then the estimates converge to their true values.

Finally, once the estimates $\hat{\boldsymbol{\theta}}'$ are found can the estimates $\hat{\boldsymbol{\theta}}$ of (4.11) be determined using the singular value decomposition of $\hat{\mathbf{E}} = \mathbf{USU}^T$ ⁴ and the following calculations

$$\mathbf{W} = \text{diag} \left(-1 + \sqrt{1 + s_{11}}, \quad -1 + \sqrt{1 + s_{22}}, \quad -1 + \sqrt{1 + s_{33}} \right) \quad (4.22)$$

$$\Delta(\hat{\boldsymbol{\xi}}, \hat{\boldsymbol{\gamma}}) = \mathbf{U}\mathbf{W}\mathbf{U}^T \quad (4.23)$$

$$\hat{\mathbf{b}} = [\mathbf{I}_3 + \Delta(\hat{\boldsymbol{\xi}}, \hat{\boldsymbol{\gamma}})]^{-1} \hat{\mathbf{c}} \quad (4.24)$$

See, section 7.8 for more aspect regarding implementing of the algorithm.

It should be noted that the calibration procedures stated above also is applicable for accelerometer calibration.

³The Jacobian are found by the partial derivative of $h(\boldsymbol{\theta}') = \mathbf{L}_k \boldsymbol{\theta}' - \|\mathbf{b}(\boldsymbol{\theta}')\|^2$ with respect to $\boldsymbol{\theta}'$, and can be seen in [Alonso and Shuster \(2002\)](#)

⁴ \mathbf{U} are a orthogonal matrix and \mathbf{S} a diagonal

Part II

System Description



Figure 4.1: The steering device, courtesy <http://www.km.kongsberg.com/>

Properties and limitations of the system will be presented in this chapter. However, to avoid product disclosure are extensive details omitted, as this could be of interest to other manufacturers.

4.3 System Properties

The steering system that is utilized in this thesis, provides steering capabilities of the seismic cables under seismic surveys. Where the steering devices, or birds, are embedded onto/into and along the seismic cables. Multiple birds are attached to the cables provide a lateral and vertical positioning of the seismic cables. The bird consist of three rotatable wings and a rotatable center frame, see Figure 2.2 and 4.1. In addition to the IMU are each wing packed with electronics, batteries and a motor. Power and signals in the seismic cables passes through the center frame of the bird in addition to other electronics.

The IMU is located in the wing aft, see Figure 2.2. Which is the least inflicted position with regard to sensor disturbances. However, IMU sensor disturbances are still present. Especially magnetic disturbances - magnetic field's from the motor, batteries and the streamer cables -, resulting in *soft iron* errors, see Section 4.2.

The bird wings has rotatable limitation of $\pm 20^\circ$. The center frame on the other-hand has a full 360° rotation capability. The wing angel and the rotation of the center frame has a close relationship. As the wing angel and the water inflow determines the position of the center frame / bird.

Every bird mounted on the streamers can communicate with a stationary computer lactated at ship dragging the seismic cables. Information form the birds is not real-time. However, it's fast enough to capture the most vital information.

4.4 System Model, Approximations and Simplifications

Since a bird model and accompanying model parameters and coefficients are not known are some simplifications utilized to derive a simple bird model. On the contrary knowing these parameters and coefficients would be of great benefit in creating simulation model as well as a torque model for the [Magnis and Petit \(2015b\)](#) observer. One could then, for instance, make a of 4 DOF(*surge, sway, roll, yaw*)⁵ model or even a 6 DOF model, depending on the known coefficients. Such models can be found in [Fossen \(2011\)](#).

The approximation and simplifications made are presented below. The reason behind these simplification are motivated by assumptions of a almost neglectable bird pitching motion, and a slowly varying yaw. A hydrodynamic roll model from [Fossen \(2011\)](#), and wing foil theory from [Newman \(1977\)](#) are utilized to create a torque roll model for the bird.

Firstly, the rigid body attitude kinetics are defined as

$$\mathbf{I}\dot{\boldsymbol{\omega}}^b - \mathbf{S}(\mathbf{I}\boldsymbol{\omega}^b)\boldsymbol{\omega}^b = \boldsymbol{\tau} \quad (4.25)$$

where $\boldsymbol{\tau}$ are sum of the external moments acting on the body. \mathbf{I} the rigid body inertia matrix and $\boldsymbol{\omega}^b$ the angular velocity.

The bird parameters used are presented in Table [C.2](#) in Appendix [C](#).

⁵Pitching motion are almost neglectable during normal operations for this system

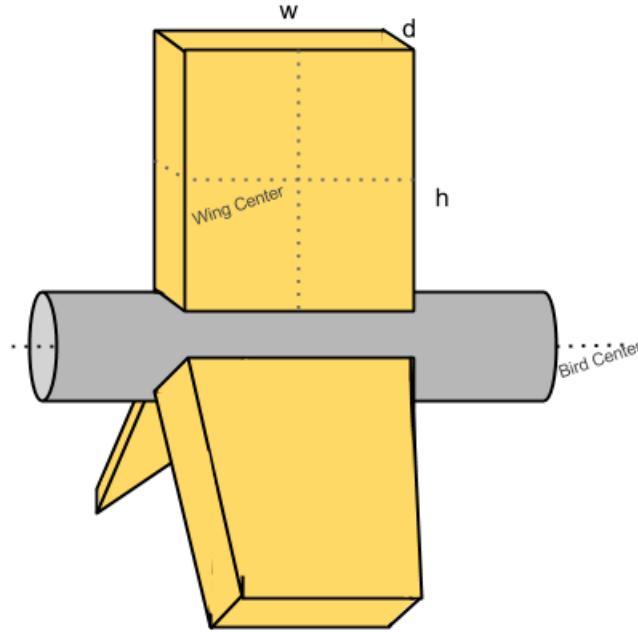


Figure 4.2: A cubic simplification of the bird wing's. The bird wing's height, width, depth and mass are specified by h , w , d and m respectively

4.4.1 Rigid Body Inertia

The bird wings are seen as solid cuboid's of a height h , width w , depth d and mass m , see Figure 4.2. The wing moment of inertia are thereafter calculated through this approximation, using (Fossen, 2011)

$$I_{x_{wing}} = \frac{1}{12} m(d^2 + h^2) \quad (4.26)$$

$$I_{y_{wing}} = \frac{1}{12} m(w^2 + h^2) \quad (4.27)$$

$$I_{z_{wing}} = \frac{1}{12} m(w^2 + d^2) \quad (4.28)$$

Furthermore, the bird are assumed symmetric yielding that the wing rigid body inertia matrix are found by $\mathbf{I} = \text{diag}\{I_{x_{wing}}, I_{y_{wing}}, I_{z_{wing}}\}$. The bird center of origin moment-inertia are calculated using the parallel-axis theorem (Fossen, 2011). The total bird rigid body inertia including

three wing's are then found to be

$$\mathbf{I}_{bird} = 3 \left(\mathbf{I}_{wing} - m \mathbf{S}^2(\mathbf{r}_{wing_c}^{bird}) \right) \quad (4.29)$$

where $\mathbf{r}_{wing_c}^{bird} = [0, 0, h/2]^T$ are the radial distance to the wing center from the bird center.

4.4.2 Roll Dynamics

As mentioned in the introduction of this chapter are non of the bird parameters or coefficients known⁶. However, studies concerning the roll dynamics and the birds external forces have been conducted by [Barheim \(2009\)](#). As the bird pitch can be assumed neglectable for this system and that yawing motion of this system incorporates the dynamics of the cable - modeling these dynamics are a thesis in itself - are only the bird roll dynamics considered. Note that in a practical situation should also the pitch and yaw dynamics be considered.

The bird net total roll torque can found by

$$\tau = \tau_{roll} + \tau_{roll_{AM}} + \tau_{roll_{drag}} + \tau_{roll_{stiffness}} \quad (4.30)$$

where $\tau_{roll_{AM}}$ are the added mass, created by body moving through the water, $\tau_{roll_{drag}}$ are the rolling drag and $\tau_{roll_{stiffness}}$ the restoring force.

4.4.3 Foil Theory

Each bird wings, seen in Figure 4.3, are seen as a foil in a fluid flow with relative angle of attack α . The total induced force, F_{wing} , on the foil can be decomposition into two forces known as

⁶These can be obtained by numerical approximations using experimental tests in a water towing-tank

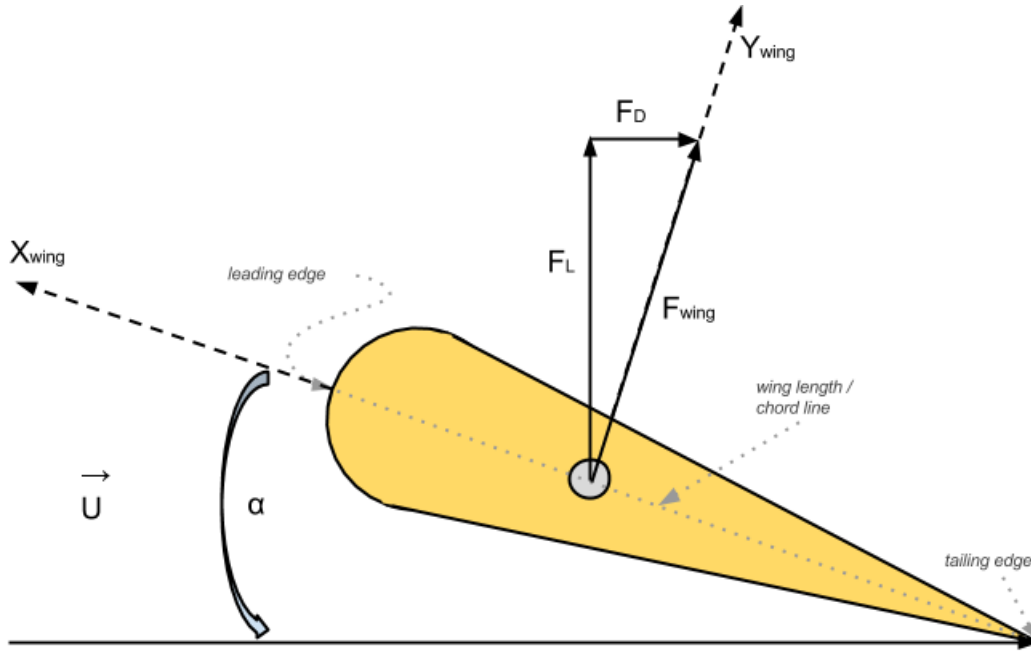


Figure 4.3: Illustration sketch of bird wing foil. Where α represents the angle of attack, F_L , and F_D are the lift and drag components of the total force F_{wing} forces, and are respectively defined perpendicular and parallel to the in-flow fluid flow velocity vector U

the lift, F_L and drag force F_D (see for instance (Newman, 1977))

$$F_L = \frac{1}{2} \rho U^2 AC_L(\alpha) \quad (4.31)$$

$$F_D = \frac{1}{2} \rho U^2 AC_D(\alpha) \quad (4.32)$$

where ρ is the fluid density, U the undisturbed in-flow fluid velocity, A the wing area and C_L and C_D are the lift and drag coefficient respectively. Furthermore, by assuming⁷ a linear relationship in the lift⁸ and drag⁹ force can equation (4.31)-(4.32) be written as

$$F_L = \frac{1}{2} \rho U^2 AC_L \alpha \quad (4.33)$$

$$F_D = \frac{1}{2} \rho U^2 AC_D |\alpha| \quad (4.34)$$

⁷Barheim (2009) has utilized much of same approximation and simplification to describing the external bird roll moment and bird forces.

⁸This are generally only valid for α less then the stall angle. Usually 15-20 deg depending on the inflow fluid (Newman, 1977)

⁹The drag coefficient are generally a sum of friction, profile, induced and wave drag coefficients and a function of both α and the Reynolds number, with a highly non-linear characteristic (Newman, 1977)

Further, assuming that these forces are in the same plane can the total force acting on the wing in the $\{wing\}$ -frame be described as

$$F_{wing} = \sqrt{F_L^2 + F_D^2} = \sqrt{\left(\frac{1}{2}\rho U^2 AC_L \alpha\right)^2 + \left(\frac{1}{2}\rho U^2 AC_D |\alpha|\right)^2} \quad (4.35)$$

α can in our case be seen as the wing yawing motion expressed in the $\{bird\}$ -frame. To handle whether F_{wing} are working in the positive or negative direction are the signum operator utilized, $F_{wing} = \sqrt{F_L^2 + F_D^2} \text{sign}(\alpha)$.

Transforming (4.35) to the $\{bird\}$ -frame yields

$$\mathbf{F}^{bird} = \mathbf{R}_{wing}^{bird} \mathbf{F}^{wing} = \begin{bmatrix} \cos(\alpha) & -\sin(\alpha) & 0 \\ \sin(\alpha) & \cos(\alpha) & 0 \\ 0 & 0 & 1 \end{bmatrix} \begin{bmatrix} 0 \\ F_{wing} \\ 0 \end{bmatrix} \quad (4.36)$$

Utilizing these assumptions can it be seen that (4.35) induces a roll moment on the bird expressed by

$$\tau_{roll} = f_c F_{wing} \cos(\alpha) \quad (4.37)$$

where f_c represent the radial distance from the $\{bird\}$ to the wing's force center along the z-axis. (Note that each wing on the bird would induce there separate roll moment on the bird expressed by (4.37). For further details on force contribution from each wing under different circumstances, see [Barheim \(2009\)](#).)

4.4.4 Rolling Added Mass, Drag and Restoring

The hydrodynamic moments acting on a rigid body can be modelled as a mass-damper-spring system ([Fossen, 2011](#)). The added mass are modelled as

$$\tau_{rollAM} = K_{\dot{\phi}} \ddot{\phi} \quad (4.38)$$

where $K_{\dot{\phi}}$ are the added mass coefficient. The hydrodynamic drag are modelled as

$$\tau_{roll_{drag}} = K_{\phi\phi}|\dot{\phi}|\dot{\phi} + K_{\phi}\dot{\phi} \quad (4.39)$$

where $K_{\phi\phi}$ and K_{ϕ} are the quadratic and linear drag, respectively. Finally, the hydrodynamic stiffness are modelled as

$$\tau_{roll_{stiffness}} = K_s\phi \quad (4.40)$$

where K_s are the restoring or stiffness coefficient of the system. These models of the hydrodynamic moments and there coefficients has been proven to be fairly accurate and in accordance with bird roll dynamics ([Torseth et al., 2014](#)).

4.4.5 IMU Centripetal Acceleration Model

The IMU sensor model are described in detail in Section 4.1. Where the centripetal acceleration on the IMU sensor frame are model accordantly to (2.28). Additionally, the lever arm, \mathbf{r}_{wing}^{bird} , are defined as

$$\mathbf{r}_{wing}^{bird} = \begin{bmatrix} x \\ y \\ z \end{bmatrix} = \begin{bmatrix} x \\ -x\sin(|\alpha|) \\ z \end{bmatrix} \quad (4.41)$$

where the y-axis lever arm are here dependent in the wing angle deflection, α .

Part III

Simulation Model

Chapter 5

Simulation model

The simulation model used in the thesis are made in Simulink. The top layer of the simulation model are seen in Figure 5.1. The model consist of a IMU model; both torque and angular velocity governed, a torque roll model and different input scenarios utilized for various simulation studies. The mathematical models utilized are described previously in the thesis.

- The IMU model are seen in Section 4.1
- The kinetics and kinematics by (4.25) and (2.8) respectively.
- The torque model as both sine input forces and as described in Section 4.4.2

The sources and sinks, in the model, are illustrated in green and red respectively. The other sub-systems are viewed in yellow and the manual switching opportunities in orange. See Appendix E for the subsystem overviews.

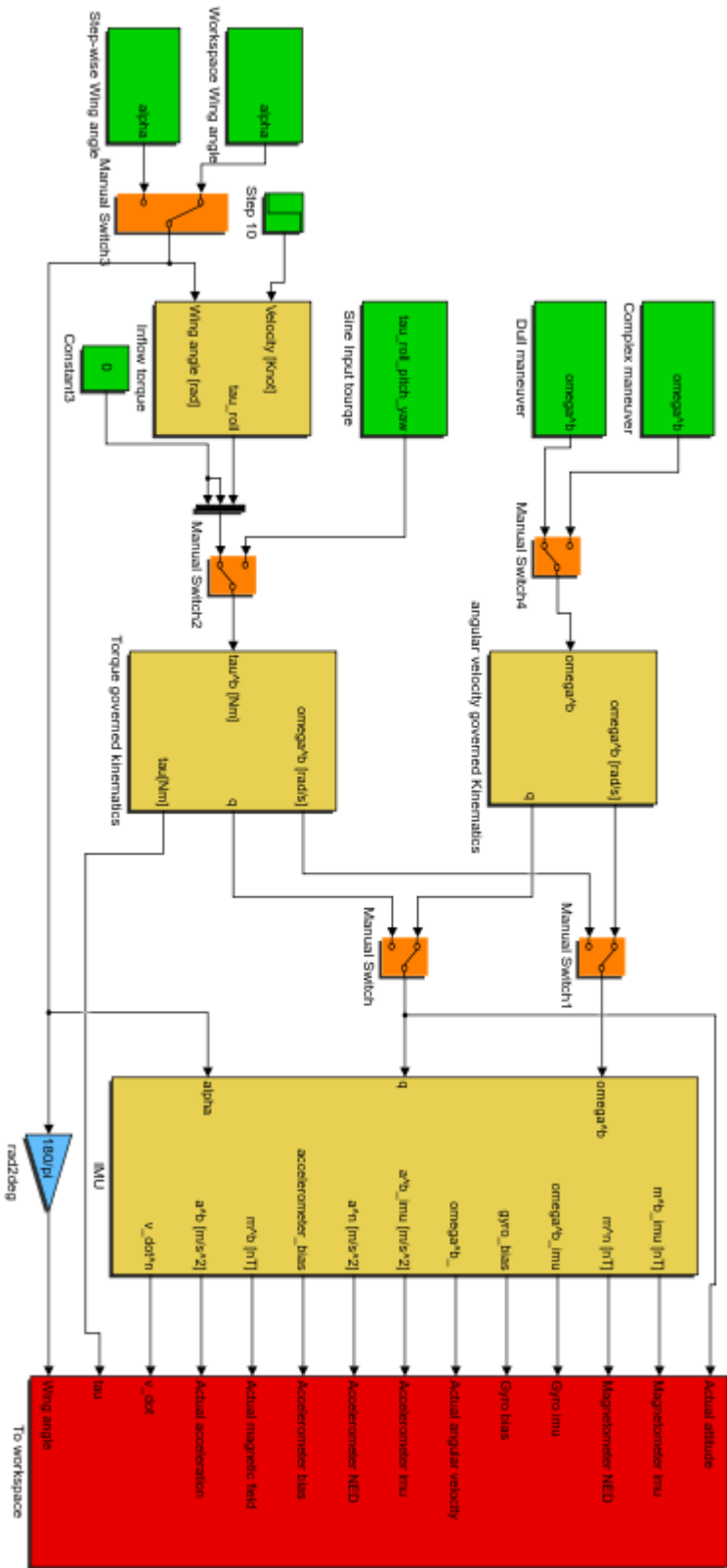


Figure 5.1: Top layer Simulink simulation model. Sources in green - angular velocity inputs and torque inputs, sinks in red - data storage, the other subsystems in yellow - IMU, kinematics and torque model.

Part IV

Implementation

Chapter 6

Algorithm Implementation Aspects

Some relevant and beneficial implementation aspects are shortly presented in a general setting. Discrete implementation and discrete integration, some common signal processing techniques, the Kalman filter corrector-predictor concept for handling measurement faults etc. and a ad-hoc magnetic disturbance handling.

6.1 Discrete Implementation

Implementation of continuous systems in a computer requires numerical methods. Moreover, the quaternion representation are utilized in almost all of the observers, except from the Grip observer which a matrix representation. As an example are therefore the discrete integration of the quaternion presented here.

Discretization using the forward Euler integration of the quaternion estimates are seen as

$$\hat{\mathbf{q}}(k+1) = \hat{\mathbf{q}}(k) + h \frac{1}{2} \mathbf{T}_q(\hat{\mathbf{q}}(k)) \hat{\omega}(k) \quad (6.1)$$

where h are the sampling interval and $\hat{\omega}_0$ ¹ represent the angular velocity estimates. Thereafter

¹The angular velocity estimates are computed in several different ways in the thesis, most often by measured angular rates, bias estimates and/or a injection term

are the quaternion, at each time step, normalized through (2.15) which minimizes *round-off-errors*. However, the normalization procedures of the first-order Euler method could also give rise to numerical errors (especially for large step sizes), adding to the already present *truncation-error* of the first order forward Euler method. See [Treven and Saje \(2015\)](#) and references therein.

On the other-hand, providing a Lie-group integrator, should theoretically avoid the need of the quaternion normalization resulting in less numerical errors. The first order Crouch-Grossman (CG) method should ensure the unity length of the quaternion. Using the 4D skew-symmetric quaternion kinematics representation, (2.11), do the Taylor expansion of the quaternion give

$$\hat{\mathbf{q}}(k+1) = \left[\cos\left(\frac{h\|\hat{\omega}_0(k)\|}{2}\right) \mathbf{I}_{4 \times 4} + \frac{1}{\|\hat{\omega}_0(k)\|} \sin\left(\frac{\|\mathbf{h}\hat{\omega}_0(k)\|}{2}\right) \hat{\Omega}_0(k) \right] \hat{\mathbf{q}}(k) \quad (6.2)$$

Also note that using the more complex higher order methods, such as the Runge-Kutta method of order 4 (RK4) or Crouch-Grossman of order 4 (CG4), would further increase the accuracy. Computational cost would then be a downside. See [Treven and Saje \(2015\)](#), and references therein, for more on integrating rotational vectors and discretization methods, their benefits and accuracy capabilities.

6.2 Corrector-Predictor Formulation

In order to handle different measurement sampling rates and enable dead-reckoning² capabilities are the Kalman filter *corrector-predictor* formulation advantageous. The general corrector-predictor formulation for a nonlinear system, $\dot{\mathbf{x}} = \mathbf{f}(\hat{\mathbf{x}}, \hat{\mathbf{u}})$, using Euler discretization are given as ([Fossen, 2011](#))

$$\text{Corrector} \quad \hat{\mathbf{x}}(k) = \bar{\mathbf{x}} + K(k)[\mathbf{y}(k) - \bar{\mathbf{y}}] \quad (6.3)$$

$$\text{Predictor} \quad \bar{\mathbf{x}}(k+1) = \hat{\mathbf{x}}(k) + h\mathbf{f}(\hat{\mathbf{x}}(k), \hat{\mathbf{u}}(k)) \quad (6.4)$$

²The case where no measurement updates are available for a period of time ([Fossen, 2011](#))

where $K(k)[\mathbf{y}(k) - \bar{\mathbf{y}}]$ are the injection term. Hence, if a measurement aren't available or faulty, do the prediction take the form

$$\bar{\mathbf{x}}(k+1) = \hat{\mathbf{x}}(k) + h\mathbf{f}(\hat{\mathbf{x}}(k), \hat{\mathbf{u}}(k)) \quad (6.5)$$

Situations where this could be the case are seen in Section 6.3 and 6.4.

6.3 Signal Processing

A low level signal processing module should always be implemented in order to handle typical signal faults. Increasing the fault-tolerance in the measurements. Faults checks for signal variance, signal freeze and wild points (Sørensen, 2013). A to high or to low measurement variance might indicate a inaccurate measurements or faulty sensor. Provided a measurement signal $\mathbf{x}(k)$ can a buffer of historic data

$$\sigma^2(k) = \frac{n}{n-1} \left(\sum_{i=k-(n-1)}^k \mathbf{x}(i)^2 - n\bar{\mathbf{x}}_k^2 \right) \quad (6.6)$$

where n are the size of the buffer containing the historic data and $\bar{\mathbf{x}}_k$ the moving average, be used to check whether there might be measurement failure or freeze.

Wild points. Sampled measurements, $\mathbf{x}(k)$, that have a considerable deviation from the previous measurements - outside a certain band about the moving mean average - are rejected for one sample. Hence, the sample measurement are accepted if it is inside the band

$$\mathbf{x}(k) \in [\bar{\mathbf{x}}_k - a\sigma, \bar{\mathbf{x}}_k + a\sigma] \quad (6.7)$$

where a are a scalar constant often set to a value between 3 – 9.

6.4 Ad-hoc Magnetic Disturbance Handling

As previously mentioned may magnetic distortion affect the accuracy of the measurements. A real-time calibration method such as [Crassidis et al. \(2005\)](#) could of course be used. However, as mentioned would the computational footprint be a drawback. On the contrary utilizing a-prior knowledge of the local magnetic field could a simple check be applied to handle cases of magnetic distortions.

The norm of the normalized magnetic measurements - in a undisturbed environment - are equal to one. Applying a simple distortion check based on this knowledge, can a band for accepted measurements be described as

$$\|\bar{\mathbf{m}}^b(k)\| \in [1 + d, 1 - d] \quad (6.8)$$

where $\bar{\mathbf{m}}^b(k)$ are the normalized measurement, d describe the threshold of acceptance. The scale of the constant d would be dependent on the accuracy and noise levels of the magnetic measurements.

Chapter 7

Algorithm Implementation

The algorithms that are studied and tested are implemented in MATLAB. This to simplify algorithm analysis and reduce bug fixing. The MATLAB codes are implemented with a object-oriented structure, enabling a short transition to a embedded system written in for instance C++. A MATLAB *Workspace* structure are enabled for execution of the algorithms. This makes it easy to shift between simulated and experimental data measurements.

Some preliminaries:

- The observer are implemented using forward Euler discretization. A Crouch-Grossman (CG) discretization could also be utilized for the $SO(3)$ defined observers, which should increase the accuracy of the discretization. However, since Grip aren't locally defined, $SO(3)$, would it be more beneficial to used consistent discretization method.
- The corrector-predictor representation are implemented on all the non-linear observers. However, to not complicate notation unnecessary are all the algorithms presented in continuous time. Furthermore, all of the vector measurements used in the observers, without exception, represented their normalized vectors.
- All the non-linear observer's are initialized by QUEST. QUEST are independent of the initial state, and provide a good initial estimate. For illustration purposes, are the Grip Algorithm utilized to show the significance of QUEST initialization compared to a zero initial-

ization. See Figure 7.2 and Section 7.5

- The Simulation are obtained at 10Hz. The reason being that the simulation time could be reduced. Moreover, the data from water test are obtained at 10Hz. The actual IMU frequency are 256 Hz.

It should also be noted that the algorithms presented, provides attitude estimates in the $\{IMU\}$ -frame (strapdown to the $\{wing\}$ -frame). Converting these estimates to the bird frame can easily be done using the rotation matrix

$$\mathbf{R}_{wing}^{bird} = \begin{bmatrix} \cos(\alpha) & -\sin(\alpha) & 0 \\ \sin(\alpha) & \cos(\alpha) & 0 \\ 0 & 0 & 1 \end{bmatrix} \quad (7.1)$$

where α is the wing angle deflection, corresponding to the wing yaw. See Figure 2.2.

7.1 Linear Acceleration Mapping and Magnetometer Tilt Compensation

Some minor implementation considerations of the linear acceleration mapping and magnetometer tilt compensating algorithm are presented.

Using the usual inverse tangent function returns angles in the range $\pm 90^\circ$. This would limit the roll motion of the bird to interval $\pm 90^\circ$ which is undesirable. However, using the two-argument tangent inverse, $Atan2(x, y)$, would enable full range representation, $\pm 180^\circ$ (Spong et al., 2006). Using the two-tangent inverse function means that a small rewriting on the roll, ϕ , mapping is done as follows

$$\phi = Atan2(a_y, -a_z) \quad (7.2)$$

The heading should also be calculated in a using the $Atan2$ function, or using the sign checking

procedures of Fossen (2011). Since the bird only will have small pitching motion are the normal inverse tangent function sufficient to obtain θ . Moreover, due to small pitch angles, are the issue of a non defined tangent inverse function not an issue¹.

The sign of the measured magnetometer z-component should be inverted. This due to the positive z-axis upwards in the measurement-frame, Figure 2.2.

7.2 QUEST Algorithm

The QUEST algorithm with covariance matrix calculation are the chosen QUEST implementation method. In addition to the properties mentioned in Section 3.2 are the QUEST algorithm, or to be more precise the QUEST algorithm with extra futures present. The possibility of calculating the attitude error covariance matrix using the procedures in Shuster (2006) makes the QUEST algorithm very beneficial as a initialization algorithm. This due to that the attitude error covariance matrix of the QUEST can be used as the measurement covariance matrix in the MEKF. Additionally to this could the optimal quaternion for the QUEST be used in the MEKF as reference quaternion. Further details about MEKF can be found in Section 3.3 and Section 7.3.

The implemented QUEST algorithm are based on Shuster and Oh (1981); Shuster (2006), using the flow chart of Takahashi et al. (2009) and can be viewed in Table 7.1. The algorithm are implemented on the premises that only two vector observations are given. Namely the magnetic and the acceleration vector. The corresponding vector measurement in the inertial frame are obtained by WWM and the assumption of constant acceleration, see Section 2.4.

Tuning

Additionally to the inertial vector measurements, do we need to specify the vector noise $\sigma = [\sigma_1 \ \sigma_2]$ of these vectors. Where σ_i^2 is the variance of any component of $\hat{\mathbf{W}}_i$ along the axis perpendicular to the actual \mathbf{W}_i . The extra weighting scalar λ_0 must also be provided. Generally, is

¹ $Atan2(x, y)$ are undefined for $(x, y) = (0, 0)$ in some software implementations. This is the case for $\theta = \pm 90$ in the horizontal plane

Description	Equation
Compute the	
Weight vector	$\frac{1}{\sigma_{tot}^2} = \sum_{i=1}^N \frac{1}{\sigma_i^2} \quad a_i = \lambda_0 \frac{\sigma_{tot}^2}{\sigma_i^2}$
Attitude profile matrix	$\mathbf{B} = \sum_{i=1}^N a_i \hat{\mathbf{W}}_i \hat{\mathbf{V}}_i^T$
Quantities S , σ , Z , Δ and κ	$\mathbf{S} = \mathbf{B} + \mathbf{B}^T \quad \sigma = \text{trace}(\mathbf{B})$ $\Delta = \det(\mathbf{S}) \quad \kappa = \text{trace}(\text{adj}(\mathbf{S}))$ $Z = \begin{bmatrix} B_{23} - B_{32} \\ B_{31} - B_{13} \\ B_{12} - B_{21} \end{bmatrix}$
Maximum eigenvalue	$\lambda_{max} = \sqrt{a_1^2 + 2a_1 a_2 \cos(\theta_V - \theta_W) + a_2^2}$
where	$\cos(\theta_V - \theta_W) = (\hat{\mathbf{V}}_1 \cdot \hat{\mathbf{V}}_2) (\hat{\mathbf{W}}_1 \cdot \hat{\mathbf{W}}_2) + \hat{\mathbf{W}}_1 \times \hat{\mathbf{W}}_2 \hat{\mathbf{W}}_1 \times \hat{\mathbf{W}}_2 $
Covariance matrix	$\mathbf{P}_{QQ} = \frac{1}{4} \left[\sigma_{tot}^2 \mathbf{I} + \hat{\mathbf{W}}_1 \times \hat{\mathbf{W}}_2 ^{-2} \begin{bmatrix} (\sigma_2^2 - \sigma_{tot}^2) \hat{\mathbf{W}}_1 \hat{\mathbf{W}}_1^T + (\sigma_1^2 - \sigma_{tot}^2) \hat{\mathbf{W}}_2 \hat{\mathbf{W}}_2^T \\ + \sigma_{tot}^2 (\hat{\mathbf{W}}_1 \cdot \hat{\mathbf{W}}_2) (\hat{\mathbf{W}}_1 \hat{\mathbf{W}}_2^T + \hat{\mathbf{W}}_2 \hat{\mathbf{W}}_1^T) \end{bmatrix} \right]$
Optimal quaternion	$\mathbf{X} = (\alpha \mathbf{I} + \beta \mathbf{S} + \mathbf{S}^2) \quad \hat{\mathbf{q}}_{opt} = \frac{1}{\sqrt{\gamma + \mathbf{X} ^2}} \begin{bmatrix} \gamma \\ \mathbf{X} \end{bmatrix}$
where	$\alpha = \lambda_{max}^2 - \sigma^2 + \kappa \quad \beta = \lambda_{max} - \sigma \quad \gamma = (\lambda_{max} + \sigma)\alpha - \Delta$

Table 7.1: QUEST

this extra scalar weight chosen as either $\lambda_0 = 1$ or $\lambda_0 = 1/\sigma_{tot}^2$ (Shuster, 2006). It is here chosen as $\lambda_0 = 1$.

7.3 MEKF Algorithm

The Multiplicative Extended Kalman filter described here are based on the paper of Markley (2003) and Shuster (2006) using the nice overview presented in Utstumo and Gravdahl (2013). In addition to the facts presented in Section (3.3) will topics regarding the measurement model of the MEKF be presented. Furthermore, the complete MEKF algorithm used in the thesis are seen in Table 7.2.

The measurement model of the MEKF is usually modelled as a m-dimensional measurement function, \mathbf{h} , consisting of vector measurements taken in the $\{body\}$ -frame, plus white noise. Leading to the need for the specification of the measurement sensitivity function, \mathbf{H} . Where $\mathbf{H} = [\mathbf{H}_a \quad \mathbf{0}_{m \times 3}]$ represent the linearized measurement function. Additionally do the measurement covariance matrix, \mathbf{R} , need to be specified by tuning. However, by using quaternion "measurements" in the MEKF can the manual specification of these be avoided. The sensitivity function \mathbf{H}_a can then be taken as the identity matrix, and \mathbf{R} can be seen as the covariance of the error angle form the quaternion measurement (Markley, 2003).

Using the QUEST method in Section 7.2 to produce these quantities would then lead a much easier observer initialization and design (Crassidis et al., 2007). The initialization would then only consist the state covariance matrix \mathbf{P} and the process covariance matrix \mathbf{Q} . Moreover, \mathbf{P} can be partitioned into 3×3 sub-matrices, \mathbf{P}_a and \mathbf{P}_b along the \mathbf{P} diagonal and \mathbf{P}_c as the correlation blocks. Together with \mathbf{H}_a do this result in a simplified covariance propagation. The linearized system matrices can then be computed as showed in Table 7.2 (Markley, 2003). Where ω_b are the gyro-measurement. The implemented MEKF observer with QUEST "measurements" are seen in Table 7.2.

Since the system described in this thesis would carry out 360° rolls, are the importance using the Gibbs vector error attitude representation imperative, see Section 3.3. This are verified and

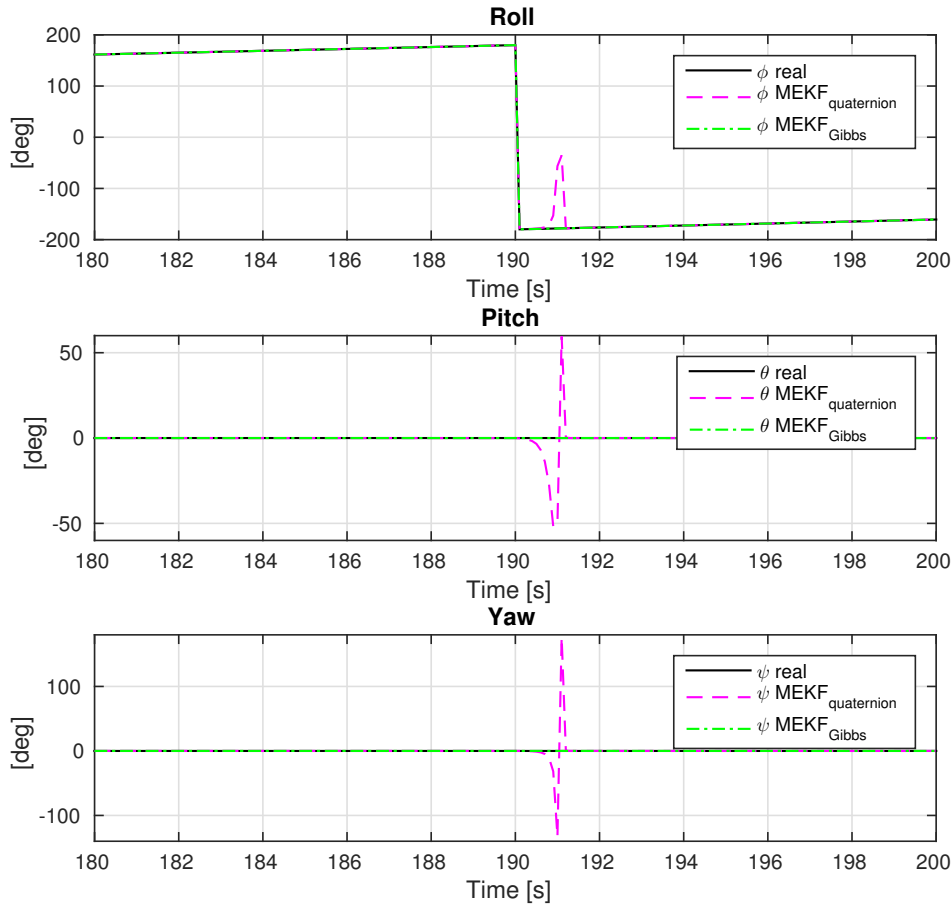


Figure 7.1: Comparing the Gibbs (green) and unit quaternion (magenta) parametrization of the attitude error in MEKF, during a 360° roll motion. Zoom of the transaction between $+180^\circ$ to -180° roll

seen in Figure 7.1. Comparing the Gibbs vector error representation with the more common unit quaternion error. As seen do large shifts in the quaternion error - $\|\delta\epsilon\| \approx 2$ - result in large errors using the unit quaternion representation. Whereas the Gibbs error representation handles this shift smoothly.

Tuning

The tuning of the MEKF are done empirically. Tuning the covariance matrix \mathbf{P} and the process covariance matrix \mathbf{Q} .

Step	Equation
Update step	
QUEST	$[\mathbf{q}_{QUEST}, \mathbf{R}_{QUEST}] = \text{QUEST}(\mathbf{m}^n, \mathbf{m}^b, \mathbf{a}^n, \mathbf{a}^b, \sigma_a, \sigma_m)$
Kalman gain	$\mathbf{K}(k) = [\bar{\mathbf{P}}_a \ \bar{\mathbf{P}}_c]^T [\bar{\mathbf{P}}_a + \mathbf{R}]^{-1}$
Covariance update	$\hat{\mathbf{P}}(k) = \bar{\mathbf{P}}(k) - \mathbf{K}(k) [\bar{\mathbf{P}}_a \ \bar{\mathbf{P}}_c]$
Attitude error	$\delta \mathbf{q}(k) = \bar{\mathbf{q}}^{-1}(k) \otimes \mathbf{q}_{QUEST}(k)$
Gibbs error	$\delta \mathbf{g}(k) = 2\delta \boldsymbol{\epsilon}(k) / \delta \eta(k)$
Innovation	$\hat{\mathbf{x}}(k) = \bar{\mathbf{x}}(k) + \mathbf{K}(k) \delta \mathbf{g}$
State update (Gibbs)	$\hat{\mathbf{q}}(k) = \bar{\mathbf{q}}(k) \otimes \begin{bmatrix} 2 \\ \hat{\mathbf{x}}_{1:3}(k) \end{bmatrix}$
Normalize	$\hat{\mathbf{q}}(k) = \hat{\mathbf{q}}(k) / \hat{\mathbf{q}}(k) $
Reset	$\hat{\mathbf{x}}_{1:3}(k) = \mathbf{0}$
Propagate	
Propagate state	$\bar{\mathbf{q}}(k+1) = \hat{\mathbf{q}}(k) + \frac{\Delta t}{2} \left(\hat{\mathbf{q}}(k) \otimes \begin{bmatrix} 0 \\ \omega_b(k) - \hat{\mathbf{x}}_{4:6}(k) \end{bmatrix} \right)$
Linearization	$\mathbf{F} = \begin{bmatrix} -\mathbf{S}(\omega_b - \hat{\mathbf{x}}_{4:6}(k)) & -\mathbf{I} \\ \mathbf{0} & \mathbf{0} \end{bmatrix}, \quad \mathbf{G} = \begin{bmatrix} -\mathbf{I} & \mathbf{0} \\ \mathbf{0} & \mathbf{I} \end{bmatrix}$
Propagate covariance	$\bar{\mathbf{P}}(k+1) = \bar{\mathbf{P}}(k) + \Delta t (\mathbf{F}\mathbf{P} + \mathbf{P}\mathbf{F}^T + \mathbf{G}\mathbf{Q}\mathbf{G}^T)$

Table 7.2: Multiplicative Extended Kalman Filter

7.4 Batista Algorithm

A overview of the observer presented in Section 3.4 are stated here. Including additional aspects and tuning. Table 7.3 presents the overall algorithm. The auxiliary observer and the actual attitude observer.

The auxiliary observer purpose is to estimate the $\{body\}$ -fixed auxiliary vector, $\mathbf{v}(t)$. Moreover, it also provide a extra future of estimating the measured $\{body\}$ -fixed vector. This observer are obtained by the decomposition of (3.17) using (3.18). The attitude observer are then designed by substituting (3.18) into (2.23).

The acceleration measurement and corresponding reference vector in $\{n\}$ is used in the implementation of this thesis, unlike Batista et al. (2014b) how uses magnetic measurements in their results. Using the assumption in Section 2.4 can we assume say that the gravity acceleration in $\{n\}$ are constant. Furthermore,

$$\omega_e^n = \mathbf{R}_n^e (\Theta_{ne})^T \omega_e \quad (7.3)$$

where $\omega_e = [0, 0, 7.292115e^{-5}]^T$ are the angular rotation of the earth - corresponding to a earth rotation about 15° per hour around it own axis - are used to obtain (3.16)

Tuning

In the observer in Table 7.3 do α_i , $i = 1, 2, 3, 4$ represent scalar positive tuning gains. As in most non-linear observer are these tuned empirically. However, Batista et al. (2014b) proposes to relate the gains α_3 and α_4 to their related vector noise and norm. The initial state for the body-fixed vector in the auxiliary observer is set equal to the first measurement of this vector, the auxiliary vector \mathbf{v}_0 are set equal to zero. Also note that the a approximated latitude needs to be provided. This to obtain the vector ω_e^n . Batista et al. (2014b) proposes that the gains for the auxiliary observer are tuned as piecewise constant tuning gains at the initialization phase. This to ensure the stability at steady-state for the auxiliary estimates.

Step	Equation
Initial estimate	
QUEST	$\mathbf{q}_{QUEST} = \text{QUEST}(\mathbf{m}^n, \mathbf{m}^b, \mathbf{a}^n, \mathbf{a}^b, \sigma_a, \sigma_m)$
Initial state	$\hat{\mathbf{q}}(0) = \mathbf{q}_{QUEST}$
Auxiliary observer	
Body vector	$\dot{\hat{\mathbf{a}}}^b = \mathbf{S}[\boldsymbol{\omega}^b + c_2 \hat{\mathbf{v}} + \alpha_1 \mathbf{a}^b \times \hat{\mathbf{a}}^b] \hat{\mathbf{a}}^b$
Auxiliary vector	$\dot{\hat{\mathbf{v}}} = \mathbf{S}[\boldsymbol{\omega}^b - c_1 \mathbf{a}^b] \hat{\mathbf{v}} + \alpha_2 \mathbf{a}^b \times \hat{\mathbf{a}}^b$
Attitude observer	
Vector correction ("bias")	$\mathbf{b} = -c_1 \mathbf{a}^b + c_2 \frac{\mathbf{a}^b}{\ \mathbf{a}^n\ } \times \left(\hat{\mathbf{v}} \times \frac{\mathbf{a}^b}{\ \mathbf{a}^n\ } \right) + \alpha_3 \mathbf{a}^b \times [\hat{\mathbf{R}}_n^b \mathbf{a}^n]$ $+ \alpha_4 \left[\frac{\mathbf{a}^b}{\ \mathbf{a}^n\ } \times \left(\hat{\mathbf{v}} \times \frac{\mathbf{a}^b}{\ \mathbf{a}^n\ } \right) \right] \times [\hat{\mathbf{R}}_n^b \mathbf{v}^n]$
Attitude	$\hat{\mathbf{R}}_b^n(\mathbf{q}) = \mathbf{R}_b^n(\mathbf{q}) \mathbf{S}(\hat{\boldsymbol{\omega}}^b + \sigma)$

Table 7.3: Non-linear attitude observer using single vector measurements

7.5 Grip Algorithm

Attitude estimation, estimating the full nine parameter rotation matrix is presented here. The algorithm exploits the concepts presented in Section 3.5 to get a global estimation of the rotation matrix that will converge to $SO(3)$.

The accelerometer and magnetometer are used as vector measurement. The corresponding vectors in the inertial frame are obtained under the same assumptions as QUEST - \mathbf{a}^n constant and \mathbf{m}^n obtained from WWM. Although the algorithm in Table 7.4 converges to the actual attitude after some time. Could for instance the QUEST method in Section 7.2 be used to get a good initial estimate. This would improve the initial convergence of the filter. See a small comparison in Figure 7.2 concerning this issue. Here are the observer 7.4 with QUEST initialization represented in green, while in blue are the observer with the rotation matrix initialization equal to the identity matrix.

Notation, $\mathbb{P}_a(\mathbf{X}) = \frac{1}{2}(\mathbf{X} - \mathbf{X}^T)$ denotes the skew-symmetric part of a square matrix, $\text{vex}(\mathbb{X})$ the vector part of a skew-symmetric matrix, \mathbf{X} .

Step	Equation
Initial estimate	
QUEST	$\mathbf{q}_{QUEST} = \text{QUEST}(\mathbf{m}^n, \mathbf{m}^b, \mathbf{a}^n, \mathbf{a}^b, \sigma_a, \sigma_m)$
Initial state	$\hat{\mathbf{R}}(0) = \mathbf{R}(\mathbf{q}_{QUEST})$
Preliminary calculations	
Injection term	$\mathbf{J}(t, \hat{\mathbf{R}}) = (\mathbf{A}^n(t) - \hat{\mathbf{R}}\mathbf{A}^b(t))\mathbf{A}^b(t)^T$
where	$\mathbf{A}^n(t) = \begin{bmatrix} \frac{\mathbf{a}^n}{\ \mathbf{a}^n\ } & \frac{\mathbf{S}(\mathbf{a}^n)\mathbf{m}^n}{\ \mathbf{S}(\mathbf{a}^n)\mathbf{m}^n\ } & \frac{\mathbf{S}^2(\mathbf{a}^n)\mathbf{m}^n}{\ \mathbf{S}^2(\mathbf{a}^n)\mathbf{m}^n\ } \\ \mathbf{A}^b(t) = \begin{bmatrix} \frac{\mathbf{a}^b}{\ \mathbf{a}^b\ } & \frac{\mathbf{S}(\mathbf{a}^b)\mathbf{m}^b}{\ \mathbf{S}(\mathbf{a}^b)\mathbf{m}^b\ } & \frac{\mathbf{S}^2(\mathbf{a}^b)\mathbf{m}^b}{\ \mathbf{S}^2(\mathbf{a}^b)\mathbf{m}^b\ } \end{bmatrix} \end{bmatrix}$
Attitude observer	
Attitude matrix	$\dot{\hat{\mathbf{R}}} = \hat{\mathbf{R}}\mathbf{S}(\boldsymbol{\omega}^b - \hat{\mathbf{b}}) + \sigma\mathbf{K}_p\mathbf{J}(t, \hat{\mathbf{R}})$
Bias observer	$\dot{\hat{\mathbf{b}}} = \text{Proj}(\hat{\mathbf{b}}, -k_I\text{vex}(\mathbb{P}_a(\hat{\mathbf{R}}^T\mathbf{K}_p\mathbf{J}(t, \hat{\mathbf{R}}))))$
Solution on SO(3)	
Attitude SO(3)	$\tilde{\mathbf{R}}(\hat{\mathbf{R}}) = [\tilde{r}_2 \quad \tilde{r}_1 \quad \mathbf{S}(\tilde{r}_1)\tilde{r}_2]$ $\tilde{r}_1 = \frac{\hat{r}_1}{\max(\ \hat{r}_1\ , \mu)}$ $\tilde{r}_2 = \frac{(\mathbf{I} - \tilde{r}_1\tilde{r}_1^T)\hat{r}_2}{\max(\ (\mathbf{I} - \tilde{r}_1\tilde{r}_1^T)\hat{r}_2\ , \mu)}$

Table 7.4: GES Non-linear attitude observer using multiple vector observations

Assumed that we have a PE system are also estimation using a single vector observation possible. Choosing $\mathbf{A}^b(t) = [\mathbf{a}^b/\|\mathbf{a}^b\|, 0, 0]$ and $\mathbf{A}^n(t) = [\mathbf{a}^n/\|\mathbf{a}^n\|, 0, 0]$. However, this are under the assumption that we have zero gyro bias. In practice could the last gyro bias estimate from the two vector observation solution be used (Grip et al., 2015). Moreover, the implemented *corrector-predictor* structure makes this switch easy.

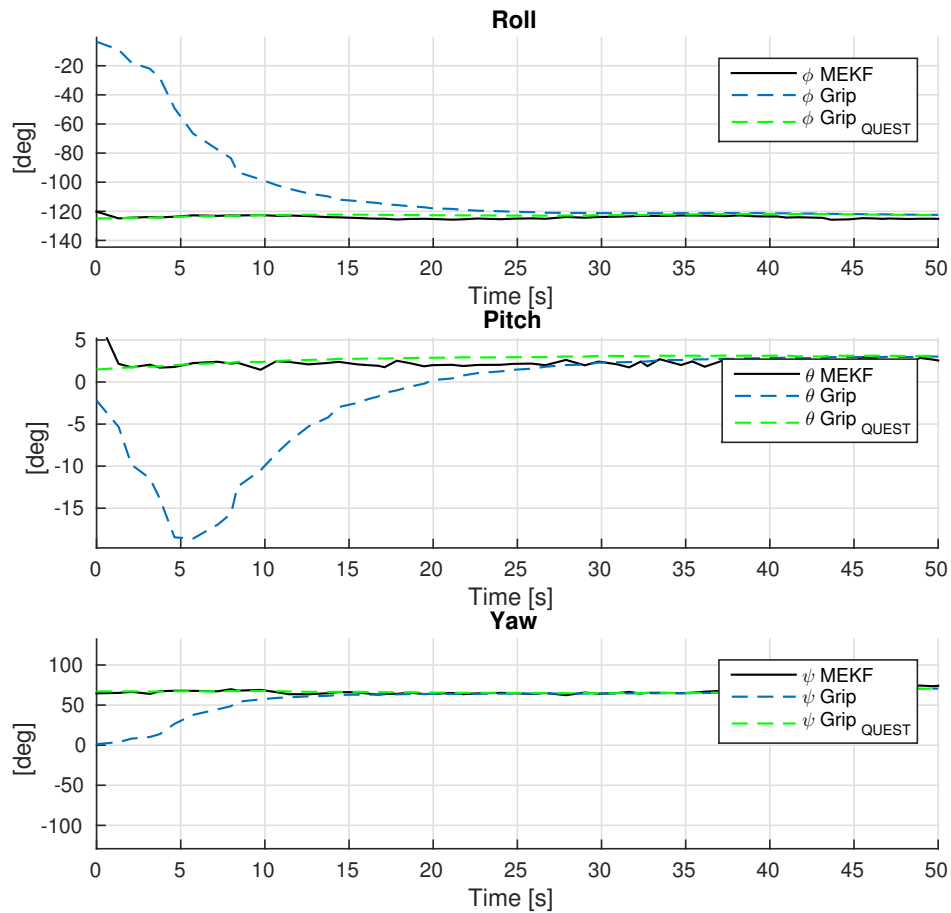


Figure 7.2: Comparison using QUEST and not using QUEST to initialize the observer in Table 7.4. The MEKF is used as truth goal. Data from field testing are utilized

Tuning

As for the tuning of the observer. This is easily done using three parameters, K_p , k_i and σ . Where $K_p \in \mathbb{R}^{3 \times 3}$ corresponds to the proportional tuning, the scalar k_i the bias tuning - or more correct the adoption gain of the bias estimate. After tuning these are $\sigma \geq 1$ then tuned to achieve stability of the estimates. Furthermore, the constant $M_b > 0$ defines the region of attraction of the bias $\|\mathbf{b}\|$ and is assumed known. $\|\hat{\mathbf{b}}\| \leq M_{\hat{b}}$ will then represent the bounded bias estimate. Provided that the initial condition satisfies $\|\hat{\mathbf{b}}(0)\| \leq M_b < M_{\hat{b}}$.

Accordingly to [Grip et al. \(2015\)](#) should choosing μ less then 0.75 ensure estimates on SO(3).

7.6 Angular Velocity Observer Algorithm

The angular velocity observer of [Magnis and Petit \(2015b\)](#) including the roll torque model introduced in Section 4.4.2 are presented. The overall torque model are given by

$$\boldsymbol{\tau} = \begin{bmatrix} \tau_{roll} \\ 0 \\ 0 \end{bmatrix} \quad (7.4)$$

The author emphasize that this simple torque model only are to display the concept using such a method as described by [Magnis and Petit \(2015b\)](#). Further analysis of pitch and yaw external moments are needed to get a full description.

Take the time derivative of the vector measurements given by

$$\dot{\mathbf{a}}^b = -\mathbf{S}(\boldsymbol{\omega}^b) \mathbf{R}_n^b \mathbf{a}^n = \mathbf{a}^b \times \boldsymbol{\omega}^b \quad (7.5)$$

$$\dot{\mathbf{m}}^b = -\mathbf{S}(\boldsymbol{\omega}^b) \mathbf{R}_n^b \mathbf{m}^n = \mathbf{m}^b \times \boldsymbol{\omega}^b \quad (7.6)$$

where \mathbf{a}^b and \mathbf{m}^b in this case are the IMU-measured acceleration and magnetic field (However, any known vector measurements could be used). Then stacking the body measurements \mathbf{a}^b , \mathbf{m}^b

and $\boldsymbol{\omega}^b$, which are governed by (7.5), (7.6) and (3.26) respectively, into the state vector \mathbf{X} are the angular velocity observer in Table 7.5 proposed by Magnis and Petit (2015b).

A easy structure, with a almost easier tuning - two scalar gains.

Step	Equation
Preliminary calculations	(see Section 4.4.2)
Calculate input torque	$\boldsymbol{\tau} = \begin{bmatrix} \tau_{roll} & 0 & 0 \end{bmatrix}^T$
Angular velocity Observer	
Observer	$\dot{\hat{\mathbf{X}}} = \begin{pmatrix} \mathbf{a}^b \times \boldsymbol{\omega}^b - \beta k(\hat{\mathbf{a}}^b - \mathbf{a}^b) \\ \mathbf{m}^b \times \boldsymbol{\omega}^b - \beta k(\hat{\mathbf{m}}^b - \mathbf{m}^b) \\ \mathbf{E}(\hat{\boldsymbol{\omega}}^b) + \mathbf{J}^{-1}\boldsymbol{\tau} + k^2\mathbf{a}^b \times (\hat{\mathbf{a}}^b - \mathbf{a}^b) + k^2\mathbf{m}^b \times (\hat{\mathbf{m}}^b - \mathbf{m}^b) \end{pmatrix}$

Table 7.5: Angular velocity observer

Tuning

The tuning of the observer is done empirically by the constant tuning parameters $\beta \in (0, 2\sqrt{1-p})$ and $k > 0$. Where p is derived under Assumption B.1 and is constant for all time, $p := \mathbf{a}^{bT} \mathbf{m}^b = \mathbf{a}^{nT} \mathbf{m}^n$. Moreover, p defines the linear independence of the vector measurements, consequently the closer p gets to 1, the slower the rate convergence. Moreover, in order to get a locally uniformly exponential stable error dynamics do the $k > k^*$ need to be satisfied. Where k^* is defined by (Magnis and Petit, 2015b)

$$K = \sqrt{\frac{1 + \frac{\beta}{2\sqrt{1-p}}}{1 - \frac{\beta}{2\sqrt{1-p}}}} \quad (7.7)$$

$$k^* = \frac{(\sqrt{\ln(K)} + \sqrt{\ln(K) + 2\beta K})^2}{\beta^2} \sqrt{2K\omega_{max}} \quad (7.8)$$

where ω_{max} is the maximum rotational rate of the rigid body. The scale of k will also have a direct impact on the convergence rate and noise sensitivity of the estimates.

7.7 Developed Attitude Observer Algorithm

The author proposed attitude observer from Section 3.7 are given a nice overview in the current section. The observer are as all the above attitude observers initialized with the quaternion estimate obtained from QUEST. The developed attitude observer can be seen i Table 7.7.

Step	Equation
Initial estimate	
QUEST	$\mathbf{q}_{QUEST} = \text{QUEST}(\mathbf{m}^n, \mathbf{m}^b, \mathbf{a}^n, \mathbf{a}^b, \sigma_a, \sigma_m)$
Initial state	$\hat{\mathbf{q}}(0) = \mathbf{R}(\mathbf{q}_{QUEST})$
Preliminary calculations	
Injection term	$\sigma := k_1 \mathbf{u}^b \times \hat{\mathbf{R}}^T \mathbf{u}^n + k_2 \mathbf{u}^b \mathbf{u}^{bT} (\mathbf{v}^b \times \hat{\mathbf{R}}^T \mathbf{v}^n)$
where	$\mathbf{v}^n = \frac{\pi_{u^b} \mathbf{m}^n}{\ \pi_{u^b} \mathbf{m}^n\ }, \quad \mathbf{v}^b = \frac{\pi_{u^n} \mathbf{m}^b}{\ \pi_{u^n} \mathbf{m}^b\ }$
	$\mathbf{u}^n = \frac{\mathbf{a}^n}{\ \mathbf{a}^n\ } \quad \mathbf{u}^b = \frac{\mathbf{a}^b}{\ \mathbf{a}^b\ }$
and	$\pi_{u^n} = \ \mathbf{u}^n\ ^2 \mathbf{I}_{3 \times 3} - \mathbf{u}^n \mathbf{u}^{nT}$
	$\pi_{u^b} = \ \mathbf{u}^b\ ^2 \mathbf{I}_{3 \times 3} - \mathbf{u}^b \mathbf{u}^{bT}$
Angular velocity observer	$\hat{\omega}^b \rightarrow$ See Table 7.5
Attitude observer	
Attitude	$\hat{\mathbf{R}}_b^n(\mathbf{q}) = \mathbf{R}_b^n(\mathbf{q}) \mathbf{S}(\hat{\omega}^b + \sigma)$

Table 7.6: Proposed attitude observer

Tuning

Except from the tuning aspects presented for angular velocity observer are k_1 and k_2 the only extra tuning parameters. These tuning gains are chosen to best get the best crossover between accelerometer and magnetometer filtering . As [Hua et al. \(2014a\)](#) describes, are k_1 and k_2 in practise chosen such that the gravity direction are emphasized over the geomagnetic field direction. The reason being that the gravity direction are more reliant compared to the geomagnetic field direction. Typically are k_2 chosen five times smaller than k_1 .

The scale of k_1 and k_2 would also depend on the angular velocity observer tuning, α and k . Where the best crossover emphasis on vector measurement and angular velocity estimates are made.

7.8 Calibration

This section presents implementation aspects, applied method and additions regarding the calibration algorithm in Section 4.2.

In order to calibrate the measurements using the Gauss-Newton method in Section 4.2, are good initial conditions needed. This to satisfy Theorem 3.5 in Appendix B. Failing to do so, may the algorithm not converge. Using the offline calibration parameters as initial estimates are a possibility. However, a centering approximation are proposed by [Alonso and Shuster \(2002\)](#) to fix this problem. This by removing quadratic term $\|\mathbf{b}\|^2$ in (4.17). Resulting in the centered measurements given by

$$\bar{y}_k = \bar{\mathbf{L}}_k \theta', \quad \bar{\mathbf{L}}_k = \mathbf{L}_k - \bar{\sigma}^2 \sum_{k=1}^N \frac{1}{\sigma_k^2} \mathbf{L}_k \quad (7.9)$$

Although this approximation do not provide a mathematical correct formulation of the minimization problem, are it still statistically correct. For further details see [Alonso and Shuster \(2002\)](#) and reference therein.

Implementation of the Gauss-Newton method also require the step length α_k to satisfy the *Armijo* and *Wolfe conditions* (Nocedal and Wright, 2006), meaning that minimization are decreased at every iteration in the Gauss-Newton method. To ensure this is the *Backtracking Line Search* algorithm in Nocedal and Wright (2006) utilized. This is not considered in the original algorithm of Alonso and Shuster (2002). However, a clear advantage using a *Backtracking Line Search* algorithm is observed in terms of the number of iterations needed before convergence.

Finally, the algorithm iterates until the precision criteria is reached. The euclidean norm of the search direction are utilized, when the new computed search direction is smaller then 10^{-8} are the algorithm executed.

It should also be noted that the inertial vector are assumed known throughout the hole measurement collection. Where \mathbf{m}^n are given by WWM, for magnetometer calibration.

Part V

Results

Chapter 8

Preliminary

The simulation and experimental field test results will be presented in the current part. Where Chapter 9 view the simulation results and Chapter 10 the experimental results of the attitude estimation. Chapter 11 view calibration results, both verification though simulation and the estimated calibration parameters obtained by the experimental data.

In order to clarify some of the results, are they given as Root-Mean-Square (errors), which is a widely used error representation method. RMS are given by

$$\mathbf{X}_{RMS} = \sqrt{\frac{1}{N} \sum_{n=1}^N |\mathbf{X}_n|^2} \quad (8.1)$$

During the simulation studies are also the error variables

$$\tilde{\mathbf{q}}(t) = \mathbf{q}(t) \otimes \hat{\mathbf{q}}^{-1}(t) \quad (8.2)$$

$$\tilde{\mathbf{R}}(t) = \mathbf{R}(t) \hat{\mathbf{R}}^T(t) \quad (8.3)$$

frequently used to present the results.

To not complicate with unnecessary citations are Grip, Batista, Magnis, QUEST, MEKF and Developed observer refereed to when taking about the algorithms in Table 7.4, 7.3, 7.5, 7.1, 7.2 and 7.6 respectively.

Chapter 9

Simulations Results

Simulation studies are presented in this chapter. Testing and verifying the algorithms in Section 7. The simulations were conducted using data obtained by the simulation model presented in Section 5. Where the simulation parameters utilized in the simulations are presented in Table C.1, C.2 and C.3 located in Appendix C.

In addition to the sensor noise - present in all the simulations - are the observers subjected to the following scenarios regarding dynamics and faults/errors

- Constant and slow dynamic behavior
- Fast dynamics
- Initialization errors
- Accelerometer and magnetometer sensor bias - *hard iron effects*
- Gyro bias
- Sensor misalignment and scale factor error - *soft iron effects*

Results of these scenarios are presented and discussed and compared against the benchmark made by the MEKF. Where the emphasis is place on their attitude(roll, pitch) and heading(yaw) accuracy. This Chapter is organized as follows

- Section 9.1: Linear mapping and magnetometer tilt compensation
- Section 9.2: Observers using single vector measurements
- Section 9.3: Developed Attitude Observer and Angular Velocity Estimation
- Section 9.4: SO(3) confined vs Global stable observer
- Section 9.5: Comparison of the attitude observers, including time varying inertial magnetic field and magnetic distortions

9.1 Linear Mapping and Magnetic Tilt Compensation

The main concern of this section are the impact of the vector measurement errors on the Euler attitude estimates. Using the linear mapping and magnetic tilt compensation method as testing algorithm. Since this are a direct mapping of the vector measurements and not considers the system dynamics or provide any extra filtering would this be a good method for purpose of this section.

Firstly, by assuming small roll and pitch angles, can the following expressions be derived (Vik, 2014)

$$\delta\phi \approx \frac{-\delta f_y}{g} \quad (9.1)$$

$$\delta\theta \approx \frac{\delta f_x}{g} \quad (9.2)$$

It is then seen that a 4 mg accelerometer error¹ results in roll and pitch error about 0.23°. Furthermore, using (3.5) and the magnetic field at Trondheim would this result in a static yaw error of 0.8 degrees. Variations in the earth's magnetic field - varying with the geographical localization - would of course affect the scale of yaw error. The knowledge of the magnetic declination angle would also contribute to this error.

¹Based on the provided IMU accelerometer noise performance

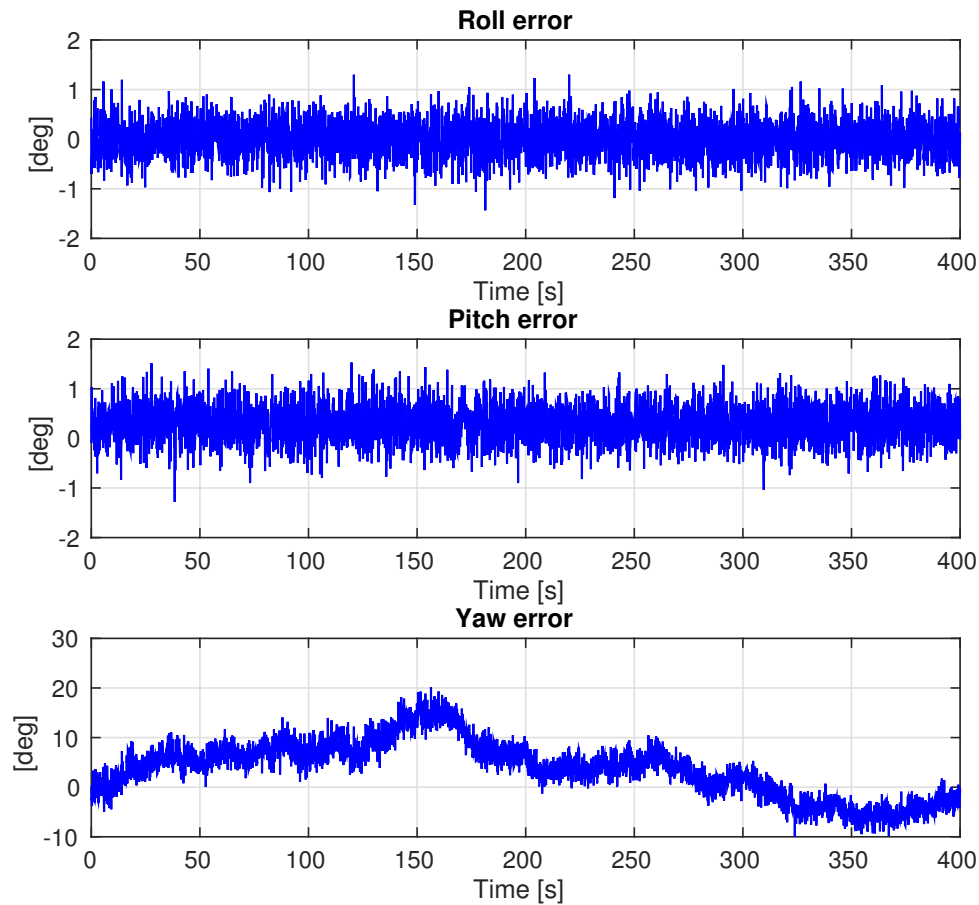


Figure 9.1: Linear mapping. Roll, pitch and yaw error when subjected to magnetic distortion. Simulation using small roll and pitch angles ($\pm 2^\circ$)

Temperature effects and changes may also be a factor concerning the heading error. For instance, a accelerometer temperature change of $0.02\%/^\circ C$ (Obtained by IMU data specs) will contribute to yaw error $\approx 1^\circ$ as a worst case scenario.

Magnetic distortion would contribute significantly. Figure 9.1 presents result of simulation subjected to general sensor noise, temperature effect and magnetic scale and misalignment errors. It can be seen that these contributions are significant in terms of yaw error. Sensor bias are not considered in this simulation. However, this would further contribute on the estimation error.

Another factor of concern are the accelerometer outputs. An accelerating IMU sensor frame

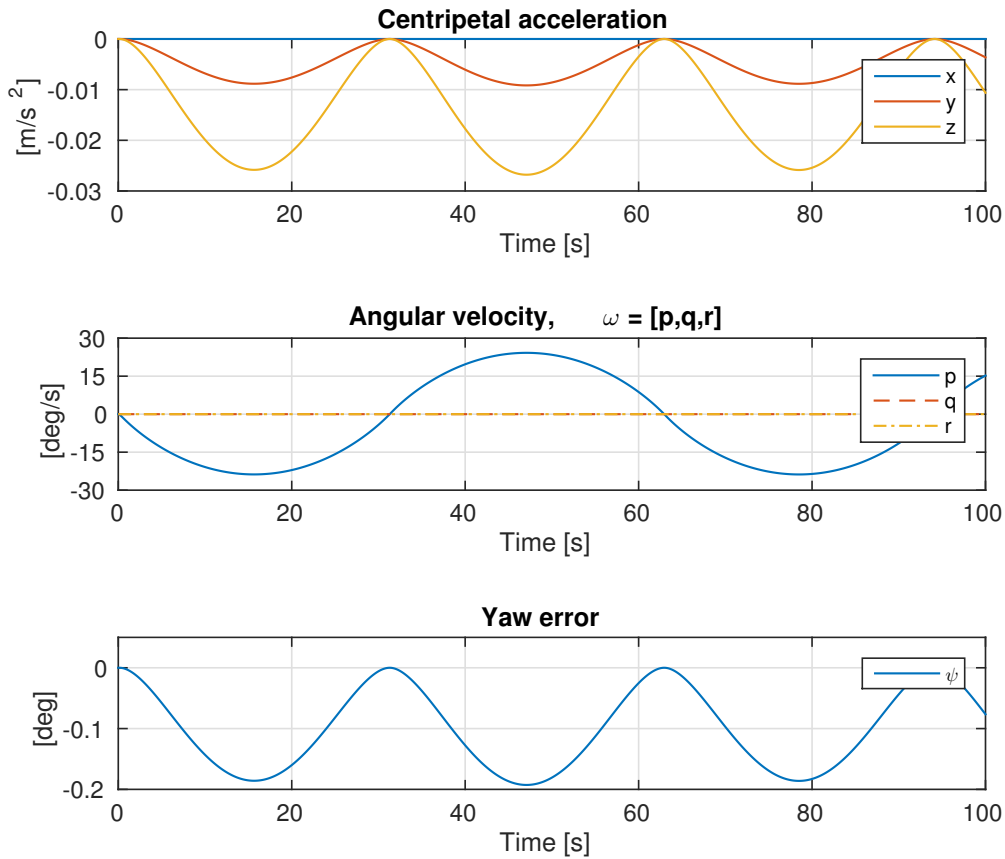


Figure 9.2: Centripetal acceleration contribution. Worst case scenario, maximum wing deflection, 20° , and bird roll angular velocity up to $25^\circ/s$

would contribute to a yaw error by introducing wrong tilt compensation. Figure 9.2 show the centripetal acceleration contribution of a bird roll subjected to roll rates close to it's system limits - $25^\circ/s$ - and with maximum wing angle at 20° . Although this is a worst case scenario, can it be seen that such a rapid bird roll motion will contribute to noticeable errors.

Discussion

As viewed by the results above, are there several error contributions influencing the accuracy of both the vector measurements and the Euler attitude estimation. Most significant would probably be the magnetic distortion. This enhances that calibration of the sensors are vital to ensure

proper measurements, some *soft-iron effects* would still be present. Moreover, the centripetal acceleration during high rolling rates are noticeable. Not significant, but noticeable. Such acceleration errors can only be removed by velocity or position aiding. However, for most of the time would such accelerations not be present, or its effect will only last for a short moment. Based on this knowledge and the fairly small acceleration contribution, is it therefore assumed in the rest of the simulations that $\dot{\mathbf{v}}_{wing/n}^n \approx 0$.

Moreover, summing all these can it be stated that the accuracy of the measurements in itself, are a important issue to be considered.

Although this method only direct map the vector measurements, and do not introduce any attentional filtering or dynamics, would it still be able to determine the attitude to some extend. But a noisy estimate of the attitude.

9.2 Observers using Single Vector Measurements

The presented results in this section are of the observers using a single vector observation. Namely the observers in Table 7.4 and 7.3. Both of the observers are subjected to the same error scenarios.

Simulations assuming noisy and non-biased measurements are presented. The reason for this assumption are that the single vector estimation of Grip are assuming that the bias are known, or more precisely it obtain by the least estimate form the two-vector-solution. Single vector estimation using the Grip method are thereby only possible for some time, depending on drifting property of the gyro. Batista on the other hand assumes a higher grade gyro, with the possibility of measuring the earth's rotation, typically a FOG or a RLG. The gyro bias are therefore assumed to be known, or at least minimal, in this section.

Another factor concerning attitude estimation using a single vector observation, are the presence of the PE (See Appendix B Definition B.4), at least for the Grip observer. In order to ensure the feasibility of estimating the attitude with a single vector observation, the accelerom-

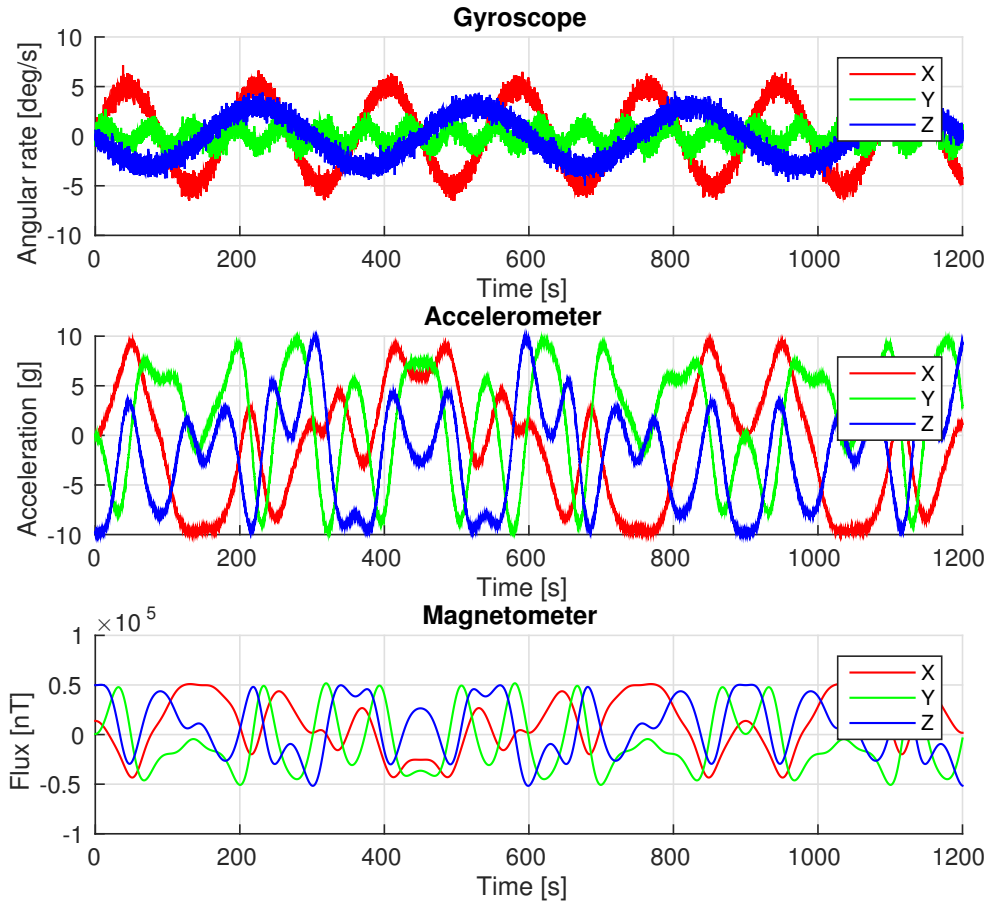


Figure 9.3: Sensor data. Complex maneuver.

eter in this case, are a complex attitude maneuver used to meet the PE requirement made by Grip. The attitude are governed by

$$\omega^b(t) = \begin{bmatrix} 5 \frac{\pi}{180} \sin\left(\frac{2\pi}{180} t\right) \\ \frac{\pi}{180} \sin\left(\frac{2\pi}{60} t\right) \\ -3 \frac{\pi}{180} \sin\left(\frac{2\pi}{300} t\right) \end{bmatrix} \text{ (rad/s)} \quad (9.3)$$

producing the measurements in Figure 9.3

Both observers are initialized with the quaternion estimate obtained by QUEST and should therefore be fairly close to the truth (but not the truth!). Tuning of the Batista observer are view in Table 9.1, which show the gain-initialization phase. The other observer gains are set to

Time interval	α_1	α_2
[0,300]	9.5	1
[300,420]	5.5	0.5
[420,600]	2.5	0.25
[600, ∞]	0.5	0.001

Table 9.1: Batista gains

$$\alpha_3 = 0.5 \tag{9.4}$$

$$\alpha_4 = \frac{0.02}{\|\mathbf{a}^n \times (\mathbf{a}^n \times \|\boldsymbol{\omega}_e\| [\cos(10.3733), 0, -\sin(10.3733)]^T)\|^2} \tag{9.5}$$

where α_4 are a combination of the initial vector and the measurement noise. The Grip observer have fixed gains, set as

$$\mathbf{K}_p = \text{diag}(5, 5, 5) \tag{9.6}$$

$$k_i = 0.03 \tag{9.7}$$

Figure 9.4 and 9.5 presents the quaternion estimate and Euler angle attitude estimate, respectively. As seen are both observers able to estimate the attitude. However, taking a closer look at the Euler attitude error in Figure 9.6, can it be seen that there actually are noticeable estimated error. The roll and pitch angle are estimated nicely by Batista, the heading estimate on the other hand have a mean estimate error of 2.5° . Moreover, the Grip estimate error actually seems to increase as time go.

Batista are also utilizing auxiliary estimates prior to the attitude estimate. Figure 9.7 presents the normalized acceleration estimate obtained from this procedure. Where it can be seen that the estimates are slightly deviating after some time. Figure 9.8 views the auxiliary vector estimate $\hat{\mathbf{v}}$.

Now, utilizing a more plausible attitude maneuver. Where the attitude are now governed by the angular velocity in Table 9.2. Seen this not necessary satisfy the PE condition, which are required for Grip method, are the Grip algorithm not able to estimate the attitude nor the heading. On the contrary Batitsta seems to produce a fairly good estimate, with an mean yaw

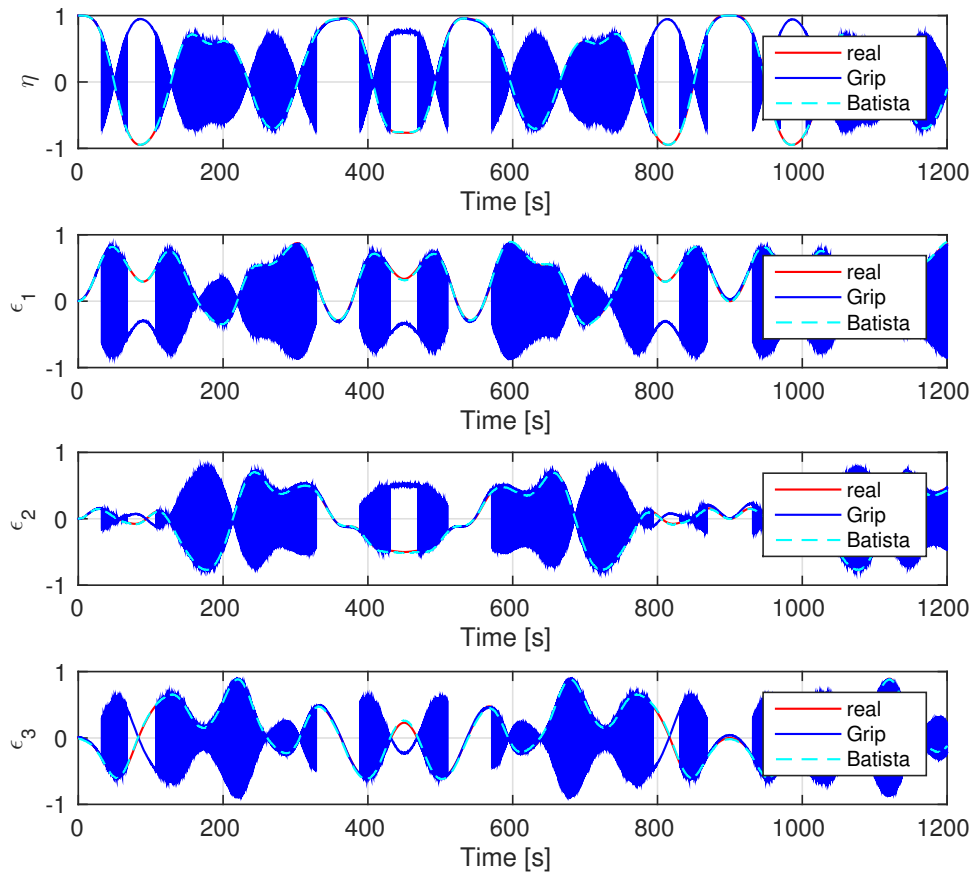


Figure 9.4: Quaternion estimate using a single vector observation. The actual or real Euler angles in red, the estimated Grip and Batista quaternion in blue and cyan respectively

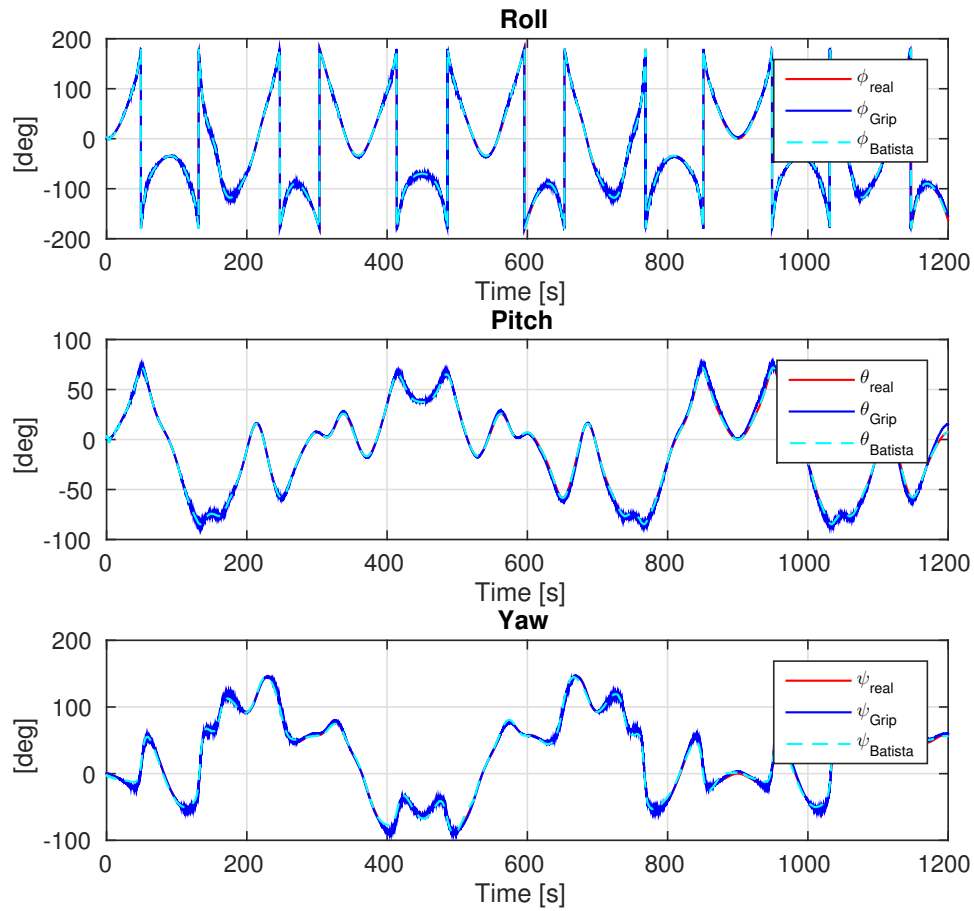


Figure 9.5: Euler estimate using a single vector observation. The actual or real Euler angles in blue, the estimated Grip and Batista Euler in blue and cyan respectively

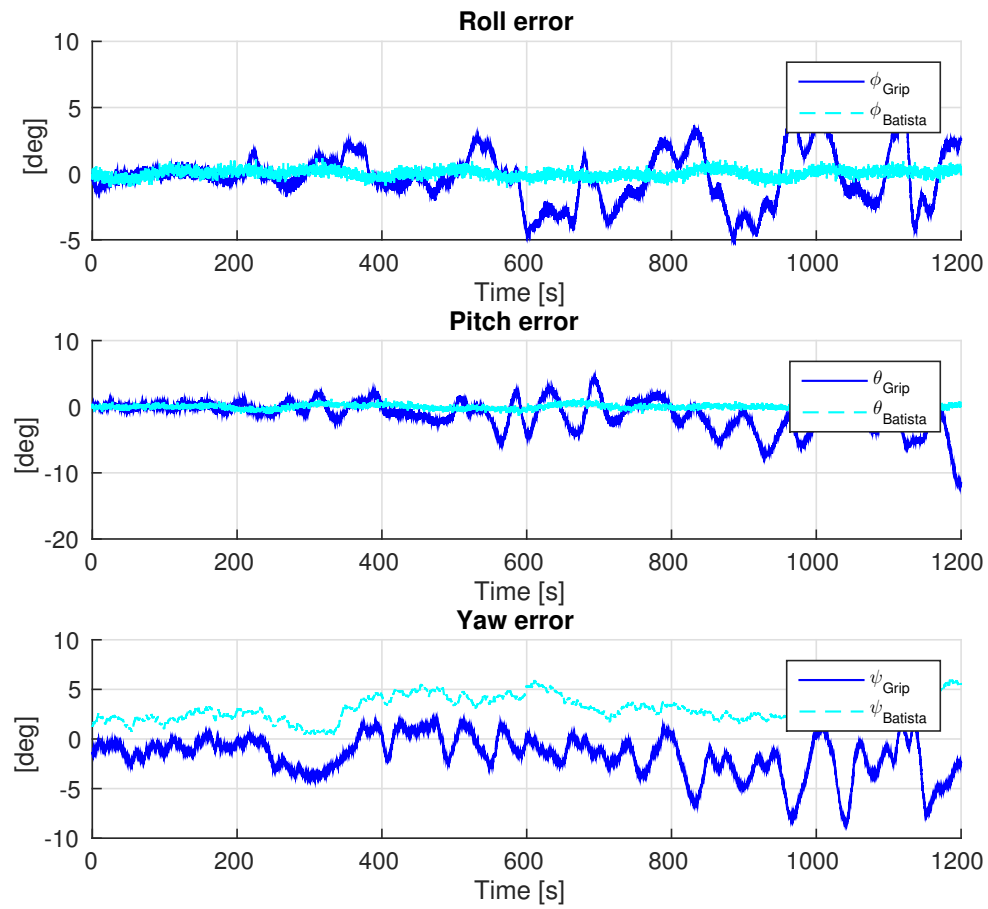


Figure 9.6: Euler estimate error using a single vector observation. Grip and Batista illustrated with blue and cyan respectively

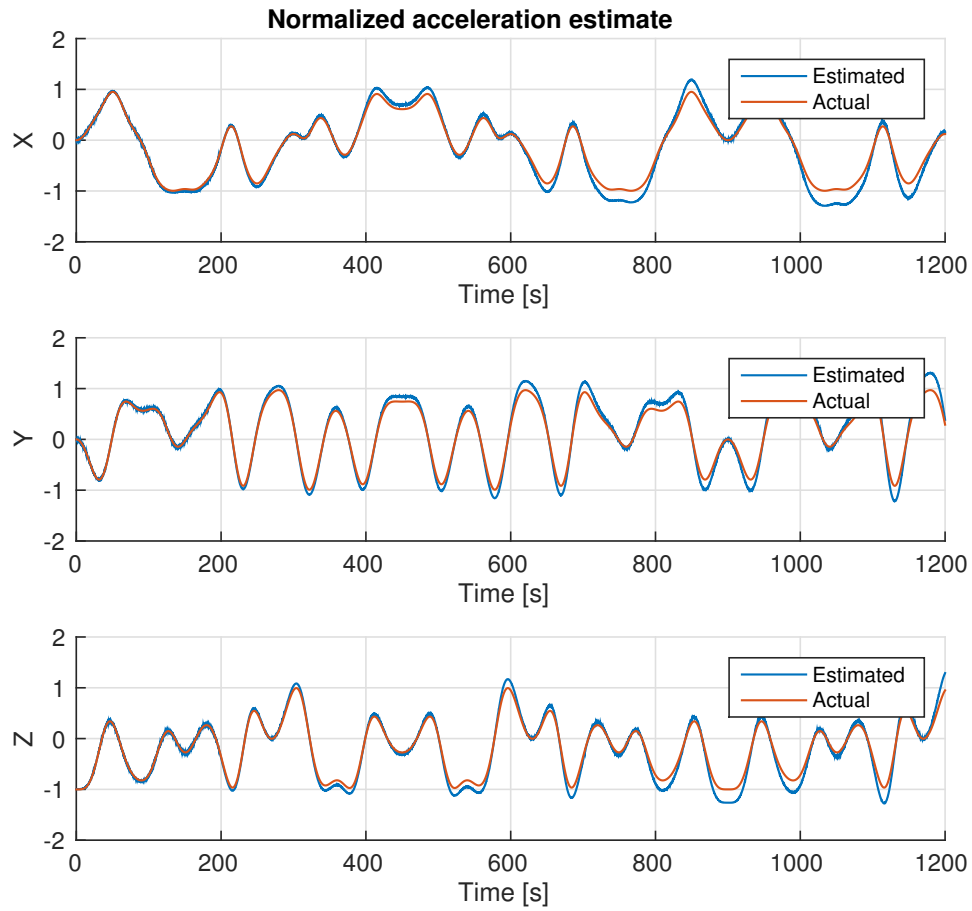


Figure 9.7: The actual and estimated X-, Y- and Z-axis normalized acceleration. Obtained by the Batista using a single vector

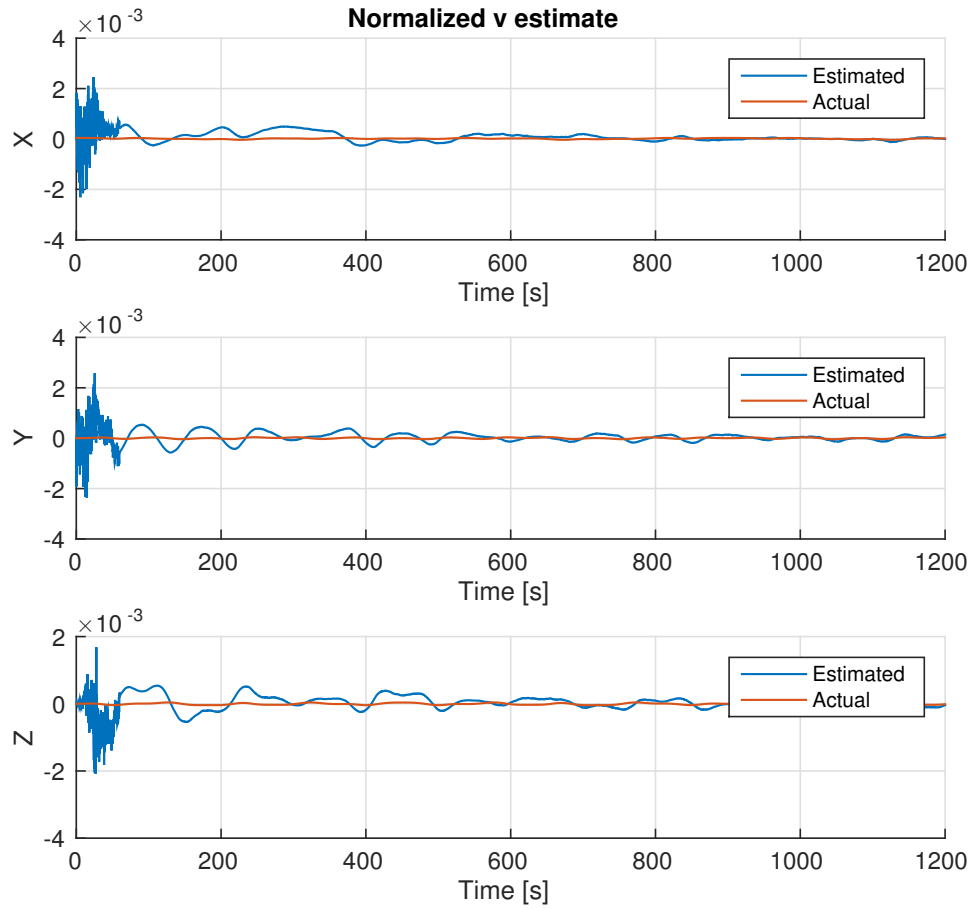


Figure 9.8: The actual and estimated X-, Y- and Z-axis normalized auxiliary vector $\hat{v}(t)$. Obtained by the Batista using a single vector

error of only 2.5 degree. See the results in Figure 9.9.

Time interval	$\omega^b(t)$, (rad/s)
[0, 360]	$[3.5\pi/180\sin(2\pi/180), 0.1\pi/180\sin(2\pi/60), 0]^T$
[360, 600]	$[0, 0, 0]^T$
[600, 1200]	$[0.1\pi/180\sin(2\pi/180), 0.001\pi/180\sin(2\pi/60), \pi/180\sin(2\pi/600)]^T$

Table 9.2: Angular velocity input

Discussion

From the results above, can one argue that applying a single vector observation are possible. Although only to some extent. Moreover, the gyro bias drift are assumed known or at least minimal. Introducing MEMS grade gyro bias drift wouldn't give any usable results and are therefore omitted. However, utilizing a higher grade gyro, a RLG, FOG or possibly more expensive MEMS gyro - less drift and noise - may help with this issue. On the other hand, the Grip method using single vector observation for short periods show promising results. The reason being that this observer makes it easy to switch between using two or one vector observation. For instance utilizing the single vector solution in cases of magnetic distortion and the two vector solution elsewhere. Batista give on the contrary better overall result when using a single vector observation under the assumptions discussed above.

The initialization error from the QUEST algorithm are fairly small. An Euler angle error of $[\phi_{error}, \theta_{error}, \psi_{error}]^T = [-0.3393, 0.1652, -1.3392]^T$. Although this initialization error are small do non of the algorithms seems to be able to correct this error in the heading estimates. But are instead fluctuating around this initialization error. Assuming a prefect initialization could on the contrary reduce the mean yaw error to less then 1 degree for the Batista observer.

The acceleration estimates of Batista are slightly deviating. The reason being somewhat strange in a "fixed" gain observer. Providing a piecewise constant gain sequence to ensures good steady-state performance should fix this problem accordantly to [Batista et al. \(2014b\)](#). How-

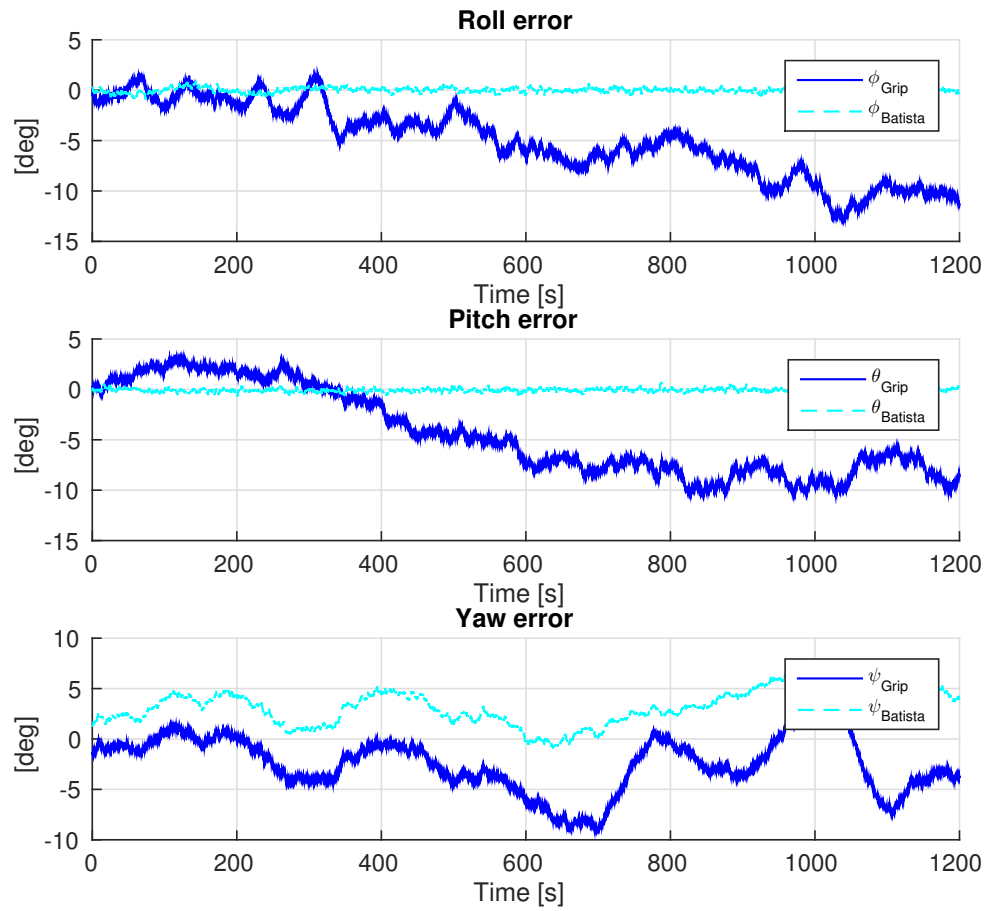


Figure 9.9: Euler estimate error using a single vector observation undergoing slow dynamics. Grip and Batista illustrated with blue and cyan respectively

ever, in practice are this method cumbersome. As tedious simulation are needed to produce a good gain-initialization phase. Moreover, the significance on the overall attitude estimation of this initialization phase are minimal. Nevertheless, a better analysis and tuning of the gain-initialization could produce smaller errors.

9.3 Developed Attitude Observer and Angular Velocity Estimation

In order for the Magnis and the Developed attitude observer in Section 7.7 to be tested in a practical application are multiple unknown bird coefficients needed. As these not are available are a pure simulation study used to make a prof of concept for this observer on the current system. However, for a more general tests on the Developed attitude observer see Section 9.5.

The Magnis angular velocity observer tuning used in the simulation where chosen as

$$k = 0.5 \quad (9.8)$$

$$\beta = 1.8\sqrt{1-p} = 0.3425 \quad \text{where} \quad p = \frac{\mathbf{a}^{nT} \mathbf{m}^n}{\|\mathbf{a}^n\| \|\mathbf{m}^n\|} \quad (9.9)$$

Where the norm of the vector measurements in the inertial frame are used to derive p , as suggested by Magnis and Petit (2015b). As in the reset of the thesis are the inertial vector measurements for the magnetometer retrieved from the WWM and the inertial acceleration are assumed constant. The initial condition of the observer where set to

$$\mathbf{X}_0 = [0, 0, 0, 0, 0, 0, 0.1, 0.1, -0.1]^T \quad (9.10)$$

which corresponds to an angular velocity error of $\omega_0 = [5.7, 5.7, -5.7]^T$ deg/s and zero acceleration and magnetic field.

Simulation are conducted assuming that only one wing are contributing to the wing mo-

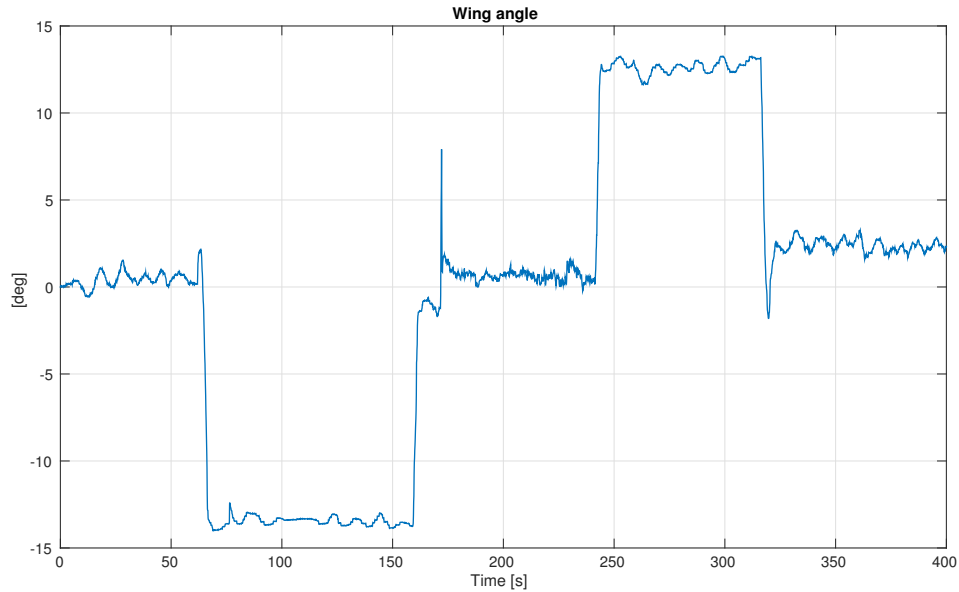


Figure 9.10: Wing deflection. Sourced from data collected during water test

ment², the two other wings have zero wing deflection. The wing angle, Figure 9.10, used as inputs are sourced from data collected from one wing during water test (See Section 10 for more information). Furthermore, the accelerometer and magnetometer measurements are assumed calibrated and known. Figure 9.11, 9.12 and 9.13 presents the angular velocity estimates, the normalized vector estimates of the acceleration and magnetic field, respectively. As one can observe do the estimates converge nicely to there true values.

The angular velocity estimates from Magnis are then governed thorough the kinematic relation of (2.23) to obtain the attitude estimate, seen in Figure 9.14 (illustrated in red). It's observed that the estimates converges, however not the true value!

As described in Section 3.7 where the author motivated by the ability of the Magnis approach of estimating the angular velocity to propose a attitude observer enabling locally exponentially stable attitude estimates. The tuning gains for the Developed observer are chosen

$$k_1 = 1, \quad k_2 = 0.3 \quad (9.11)$$

²There are no controller contributing to ensure stability

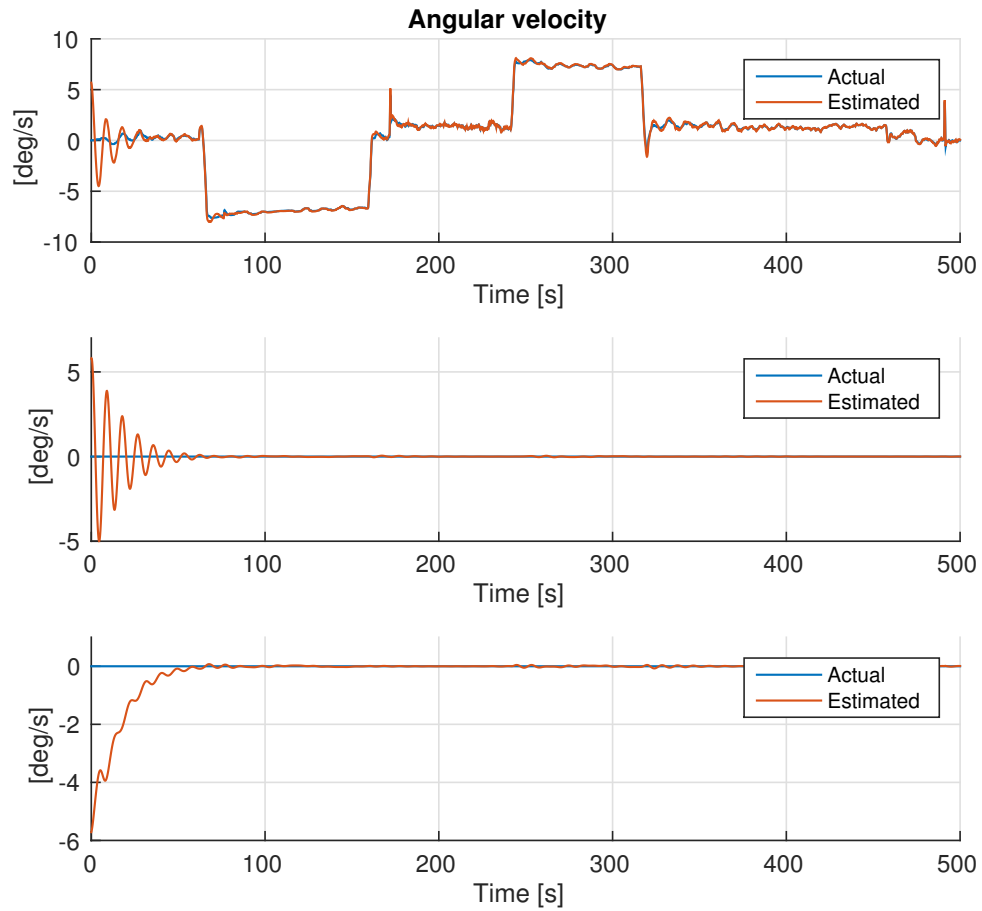


Figure 9.11: Gyroscope estimate.

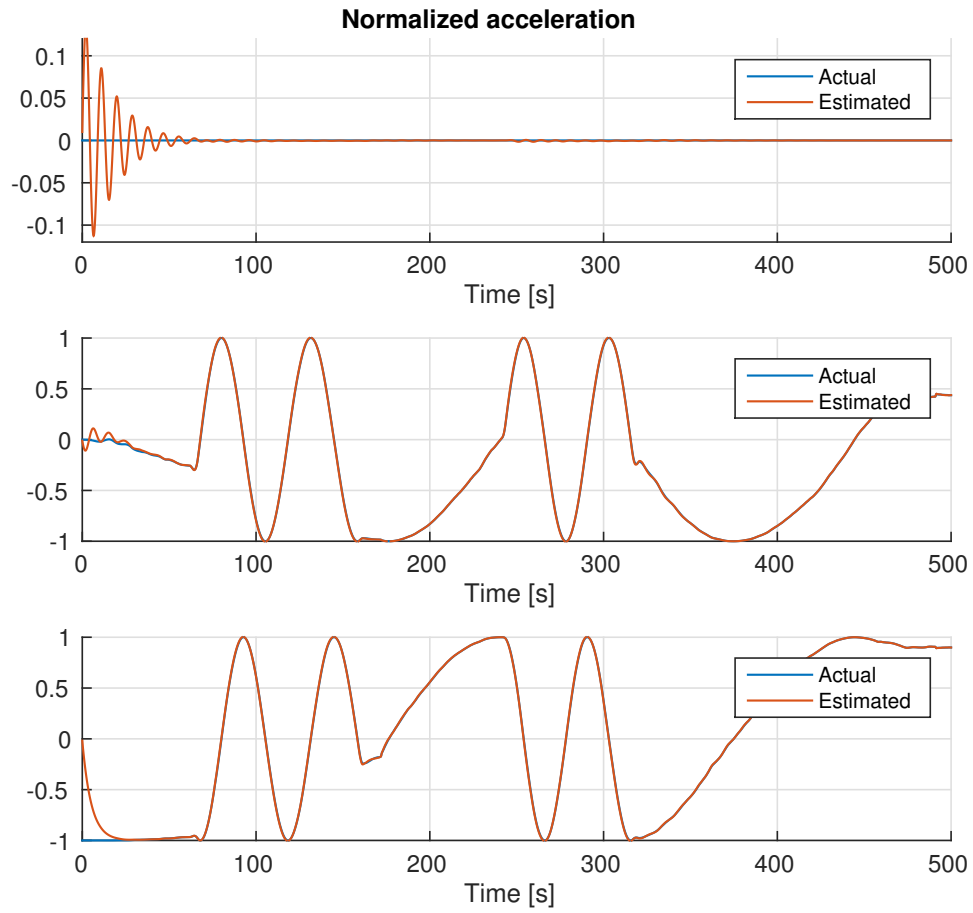


Figure 9.12: Normalized acceleration estimate.

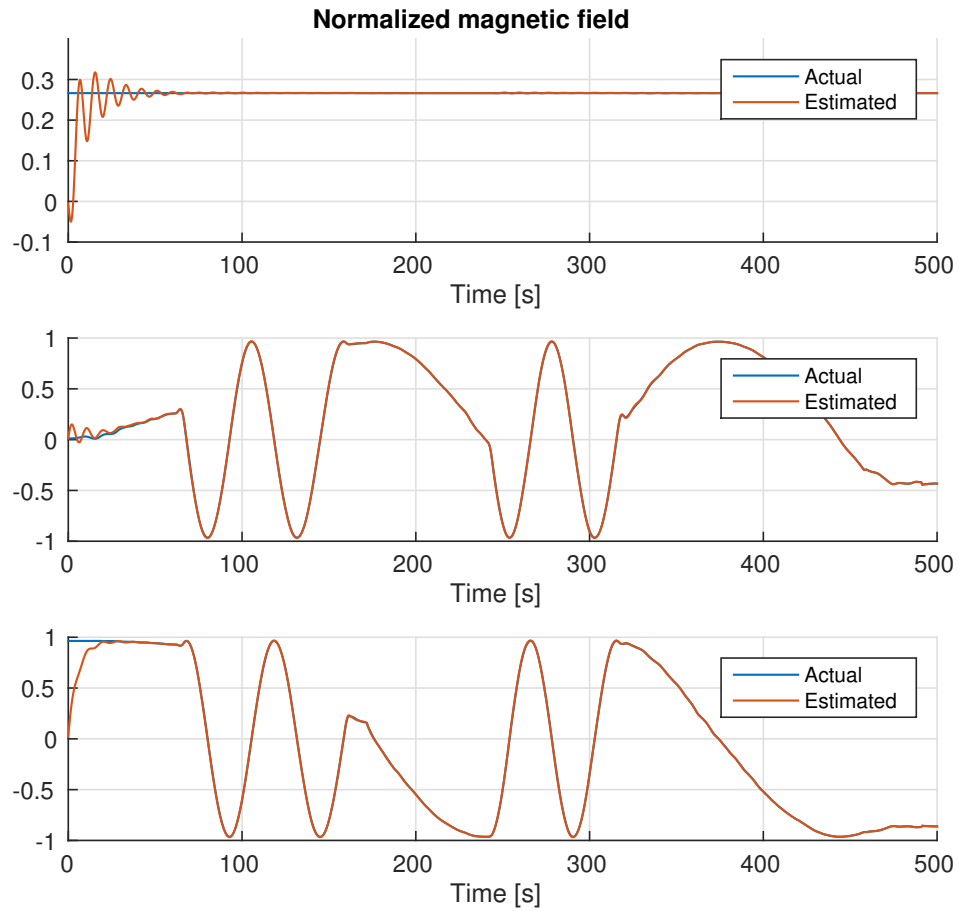


Figure 9.13: Normalized magnetic field estimate.

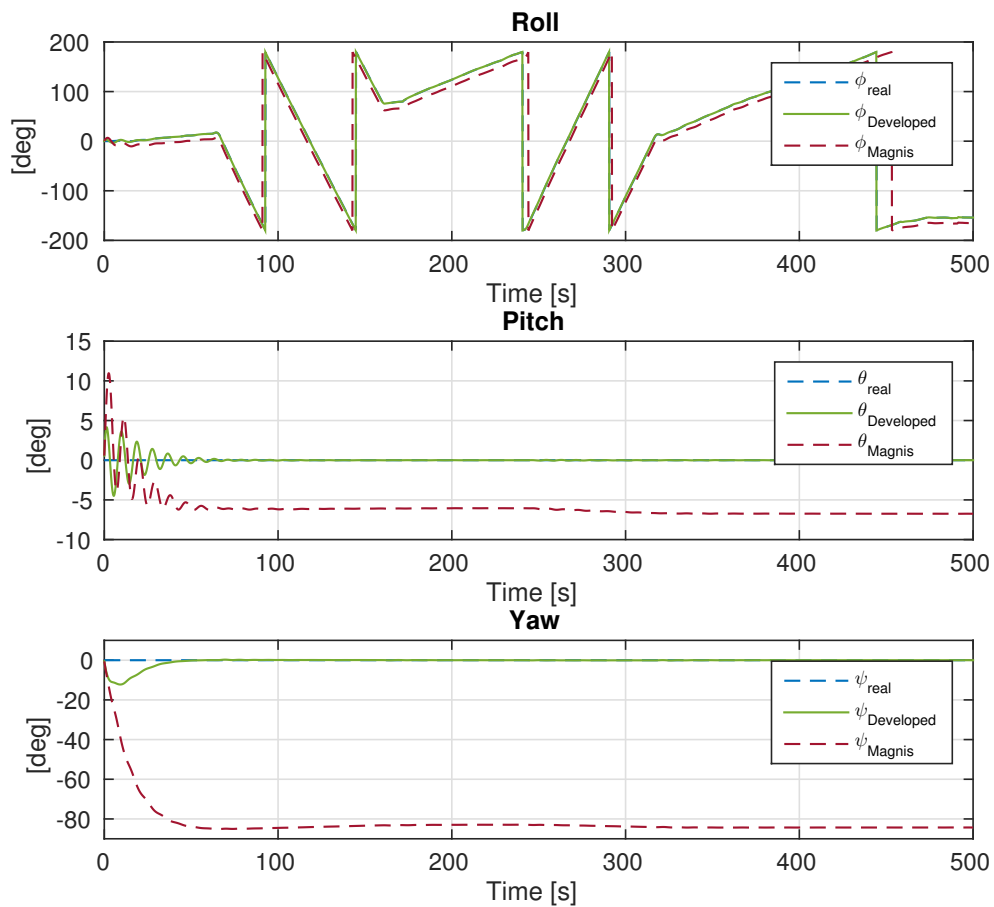


Figure 9.14: Euler angles estimates. The actual estimates (blue), the Developed attitude observer (green) and the Magnis estimate (red)

In Figure 9.14 can it be seen the significance on attitude estimates (green) using the injection (3.29) to derive the attitude through (3.28). The estimates converges nicely to there true values. Additional results concerning the Developed attitude observer - decoupling of the roll and pitch estimates from yaw and magnetic measurements, measurement noise handling etc. - are seen in Section 9.5.

Discussion

The angular velocity as well as the acceleration and magnetic estimates are seen to converge nicely after some settling time. Where the transient behavior of the settling time are strongly

influenced by the initial estimate of the angular velocity as well tuning and aggressiveness (gain scale) of the observer. Additionally, are this observer highly dependent on the torque, τ , input model. Nevertheless, results presented above motivates to further investigate the external forces and moments acting on the bird in order to make a more detailed and accurate torque input model. Including external forces contributions on both pitch and yaw moment. In the rest the simulation study are τ assumed known without any restrictions.

Another interesting aspect using such as approach are that the noisy measurements as well as the drift property of low cost MEMS rate gyros utilized in this system can be replaced with these less noisy estimates. Moreover, the Magnis observer's ability of estimating all the body-fixed measurements show that even the magnetometer and accelerometer measurements could be substituted by their estimates in the attitude determination of the Developed observer. Further investigation of the aspects of this approach are therefore advised.

9.4 SO(3) Confined vs Globally Defined Observer

A small comparison between a attitude estimation on SO(3) and a global attitude estimation are presented. In order to get fairly comparable results are the algorithms of [Grip et al. \(2013\)](#) and [Grip et al. \(2015\)](#) used in the comparison. Although these estimation schemes presents different approaches in estimating the attitude, are they still very comparable. Both observers introduces the same approach in gyro bias estimation , a two vector measurement observation for computing the attitude and both observers presents the opportunity of a SO(3) solution. More precisely a SO(3) solution ([Grip et al., 2013](#)) and a solution that converges to SO(3) ([Grip et al., 2015](#)).

The comparison are made by looking at the quaternion error estimate of both observers. Where the quaternion error angle β^3 (See section 2.2.2) are utilized to present the result.

Assuming measurements governed by discontinuous angular roll velocity, $p = 20\pi/180\text{square}(2\pi/60)$, and a roll initialization error of 180° , can it clearly be seen by Figure 9.15 that the SO(3) defined

³This angle is also known as θ in the Euler axis/angle attitude representation

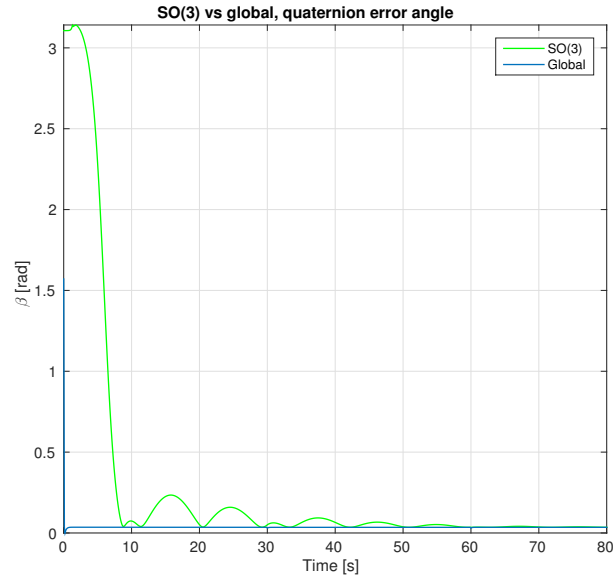


Figure 9.15: Comparison of globally defined and SO(3) confined attitude estimation. Represented by the quaternion error angle

estimation endures some unwinding as well a higher initial transient compared to the globally defined estimation.

Discussion

The result above emphasizes the role of a globally defined attitude estimation when it come to accuracy. Where discontinuity of the angular velocities measurements cause the unwinding of the quaternion. This may be the case of a slow sampling rate or temporally loss of measurements. The slow sampling rate situation and unwinding are seen using the experimental data, which are obtained at 10Hz, resulting in that the locally defined observers endures some small unwinding. However, it is believed that quaternion unwinding problem are a bigger issue for attitude control case. See Section 2.2.4 and [Bhat and Bernstein \(2000\)](#) for more details.

9.5 Comparison of the Attitude Observers

This section presents a comparison of the non-linear observers Grip, Developed and the deterministic MEKF filter and the QUEST algorithm. The algorithms heading estimate accuracy are emphasized, since this is the main concern for the purpose of this system. Nevertheless, other important aspects or abilities of the observers will also be presented - eg. magnetic disturbances. The simulated data are governed by the angular velocity in Table 9.2. Moreover, noisy measurements and biased gyro are used.

The tuning of the Developed observer are seen in Section 9.3. The Grip tuning in Section 9.2, where the Grip bias parameter bounds are chosen as

$$M_b = 0.30 \quad M_{\hat{b}} = 0.31 \quad (9.12)$$

which will ensure a parameter projection, $\|\hat{\mathbf{b}}\| \leq 0.31 [rad/s]$. The MEKF are tuned as follows

$$\bar{\mathbf{P}}_{a_0} = \text{diag}(0.1, \quad 0.1, \quad 0.1) \quad \bar{\mathbf{P}}_{c_0} = 1e^{-3} \text{diag}(1, \quad 1, \quad 1) \quad (9.13)$$

$$\mathbf{Q} = \text{diag}(5e^{-8}, \quad 5e^{-8}, \quad 5e^{-8}, \quad 1e^{-13}, \quad 1e^{-13}, \quad 1e^{-13}) \quad (9.14)$$

and the QUEST tuning are

$$\sigma_1 = 0.06905 \quad \sigma_2 = 0.1753 \quad (9.15)$$

Figure 9.16 presents the quaternion estimates of all the algorithms. The Euler angle error can be seen in Figure 9.17. It can be seen that all of the observer estimate the attitude correctly. The estimates are quit noisy, which are also expected regarding the high measurement noise. The Developed attitude observer stands out in noise performance, this are of course due to the ability to omit the noisy gyro measurement and use the estimates instead. The RMS of the Euler angle error for all the algorithms are seen in Table 9.3.

The bias estimation of MEKF and Grip can be seen in Figure 9.18. As seen are both methods

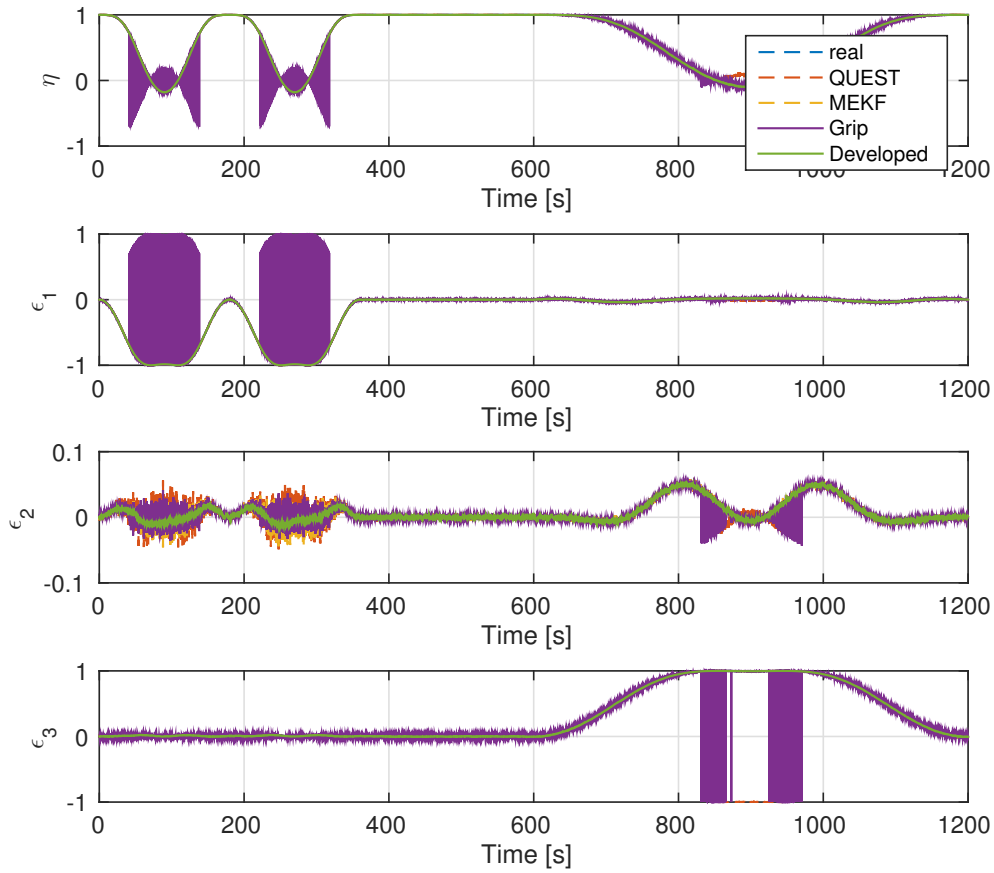


Figure 9.16: Quaternion estimates. Comparing the algorithms of Grip(purple), QUEST(striped, red), MEKF(striped, yellow) and the developed(green) attitude observer. The actual attitude in blue

Observer	RMS roll error [deg]	RMS pitch error [deg]	RMS yaw error [deg]
QUEST	0.37°	0.25°	1.76°
MEKF	0.34°	0.25°	1.56°
Grip	0.27°	0.23°	1.03°
Developed	0.18°	0.12°	0.45°

Table 9.3: Root-mean-square Euler angle error. Comparing of Grip, QUEST, MEKF and the Developed attitude observer.

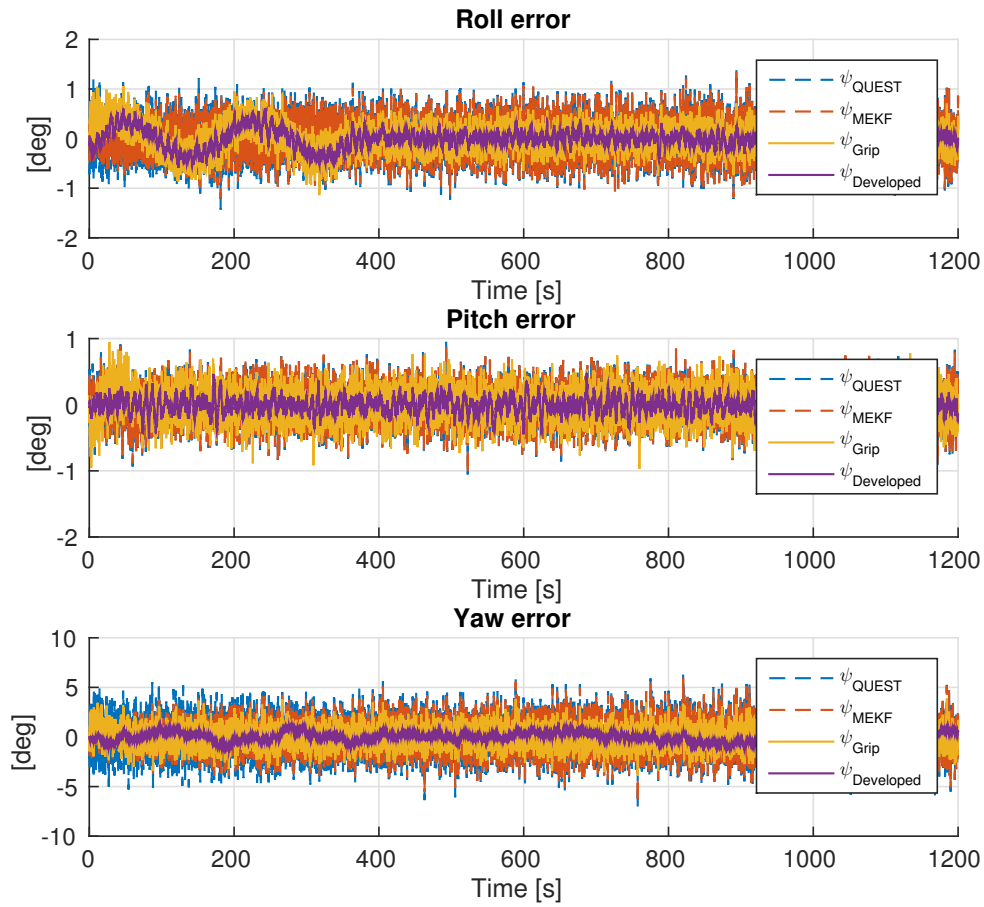


Figure 9.17: Euler angle error. Comparing the algorithms of QUEST(striped, blue), MEKF(striped, red), Grip(yellow) and the Developed(purple) attitude observer

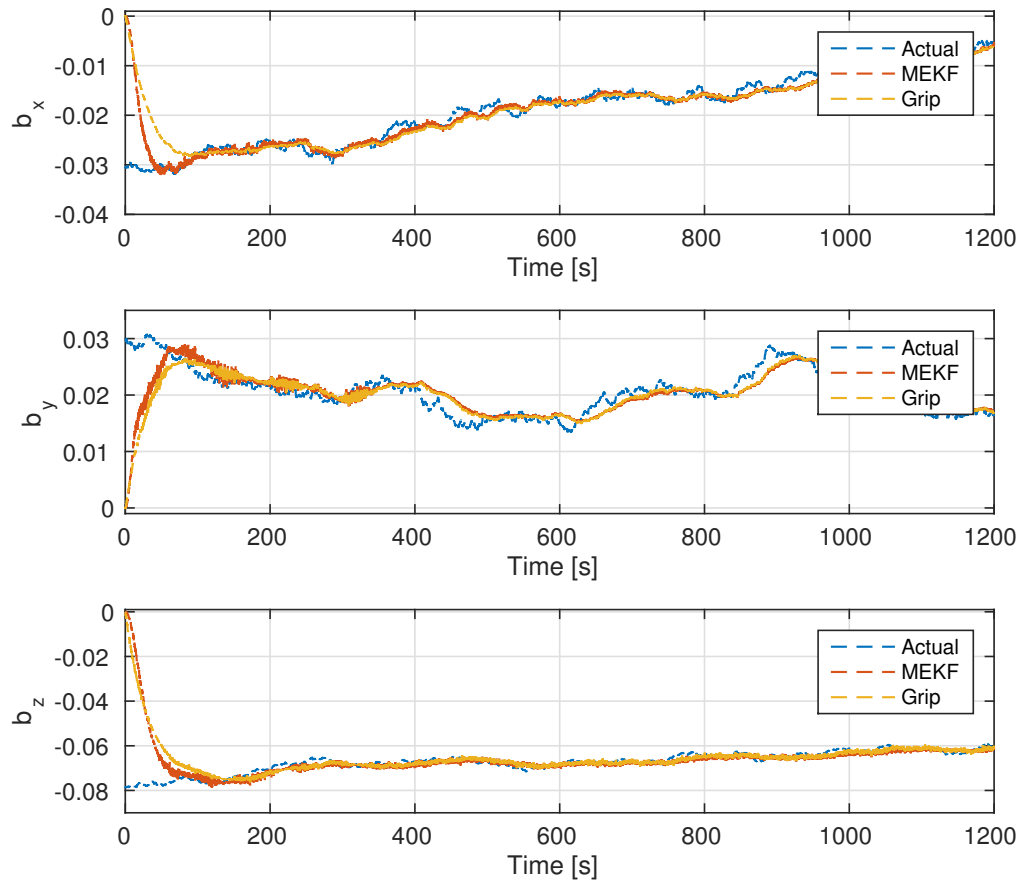


Figure 9.18: Grip(striped, yellow) and MEKF(striped, red) Gyro bias estimation compared against the actual bias. Both methods converge to the actual gyro bias

estimating the drifting gyro bias nicely. As the rest of the estimates are these quite noisy, due to the high noise level in the estimates. Furthermore, the noise level of the gyro bias estimation are highly dependent on the scale of k_i (Grip) and $\bar{\mathbf{P}}_c$ (MEKF).

Magnetic Distortions

Now introducing magnetic distortion in the magnetometer measurements, so-called *soft iron effects* - orthogonality and scale factor errors. The magnetic distortion are turned on after 100 seconds and turned off after 300 seconds.

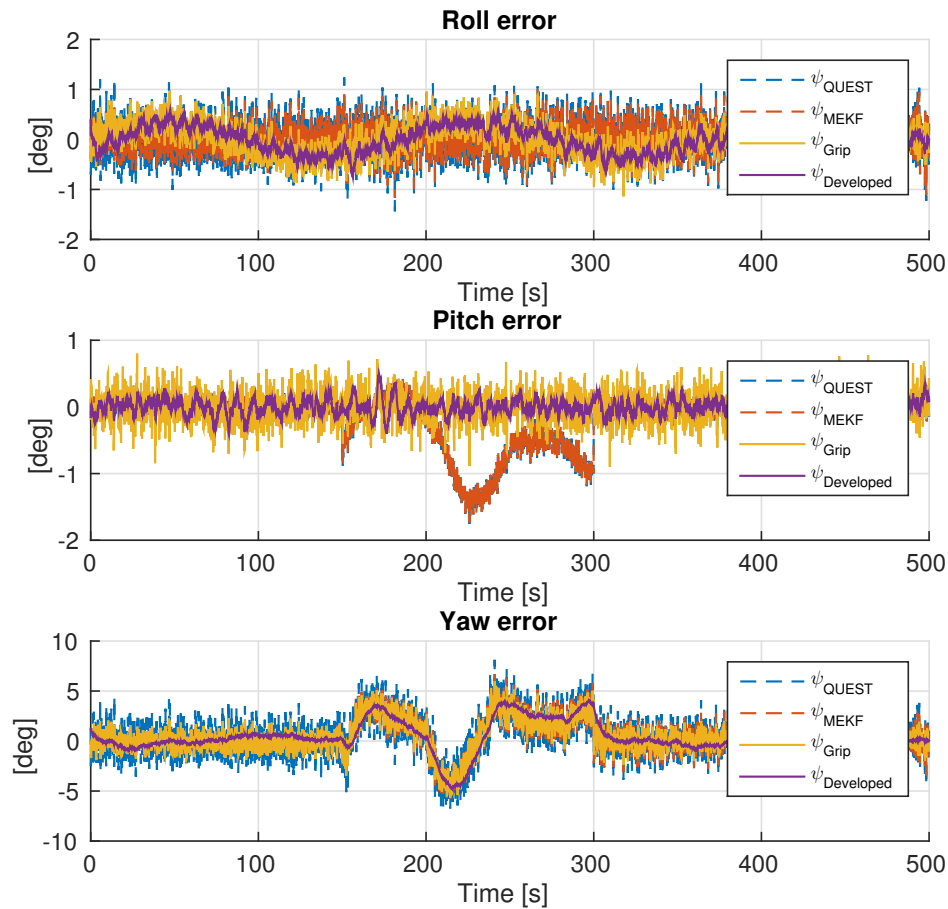


Figure 9.19: Euler angle estimate error. Magnetic misalignment and scale factor are introduced at 100 seconds and turned off after 300 seconds

Figure 9.19 presents the results of the algorithms ability to handle cases of magnetic distortion. It is observed that the both Grip and the Developed observer have the ability decoupling the roll and pitch estimates from magnetometer readings making the roll and pitch estimates unaffected by the magnetic distortion. It is however evident that magnetic disturbance impact on the yaw estimate are significant for all of the observers.

Now utilizing the corrector-predictor implementation of the observers and the ad-hoc magnetic distortion check in Section 6.2 and 6.4, respectively. The threshold constant d are chosen $d = 0.0015$. From Figure 9.20 can it be seen that the corrector-predictor formulation and the ad-hoc magnetic distortion introduce decreases the heading error. However, the roll and pitch

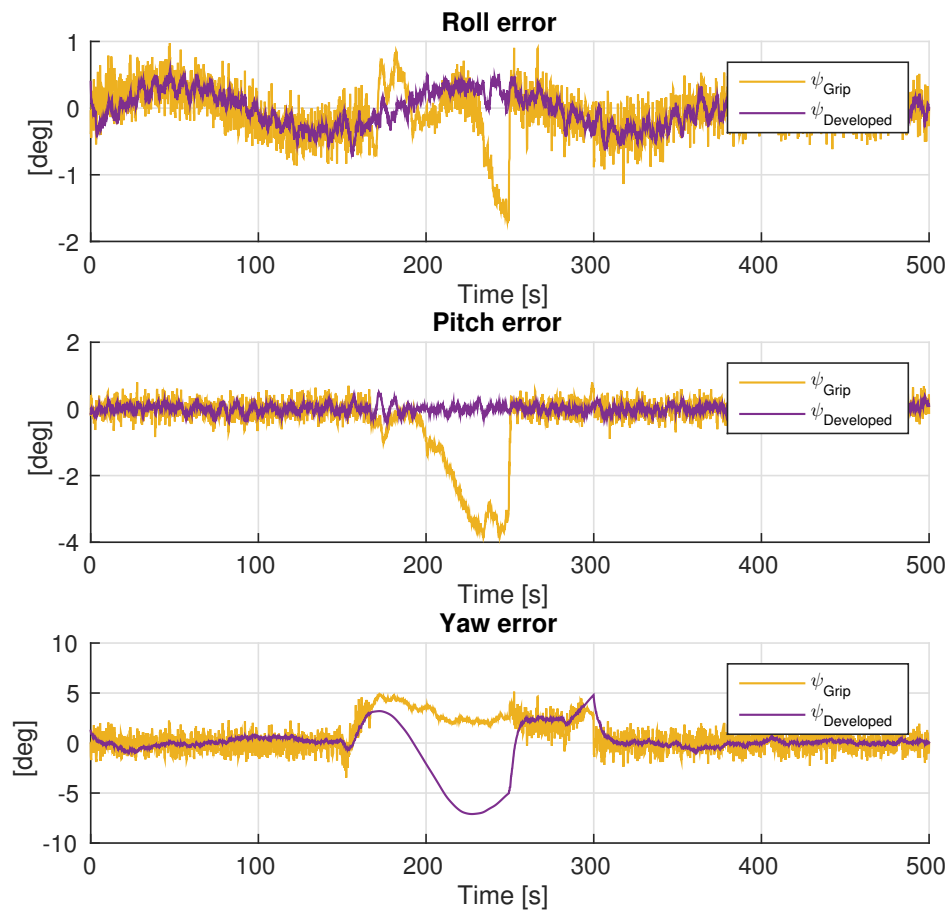


Figure 9.20: Grip and Developed with As-hoc magnetic disturbance handling, Euler angle estimate error. Magnetic misalignment and scale factor are introduced at 100 seconds and turned off after 300 seconds

errors increases for Grip. The heading error are reduced with almost 1° . Grip are able to keep a fairly constant heading error during the disturbance.

Time Varying Local Magnetic Field

Another factor of concern are the knowledge of the local magnetic field. Although, this is easily obtained by the WMM, are the knowledge of the current geographical localization (latitude and longitude) needed. Which aren't necessarily known, as the bird do not have a GPS.

Take for instance the example of a seismic operation, mapping the sea floor from Trondheim and one day straight north at 4 knots. Which certainly could be a case.

Traveling at 4 knots for 24 hours are equivalent to a travel distance of 178 km. Moreover, a meridian length⁴ of one degree latitude shift correspond to traveling distance of 111.2 km on the earth sphere (Osborne, 2013). Which mean that the local magnetic field would change from $\mathbf{m}_{from}^n = [13772, 604, 49823]^T$ to $\mathbf{m}_{to}^n = [12907, 589, 50478]^T$ witch corresponded to a latitude change of 1.5°.

On the other-hand travelling same distance west at a constant latitude. Where the length of one longitude degree are given by (Osborne, 2013)

$$\Delta_{Longitude} \approx \frac{\pi}{180} r_e \cos(\mu) \quad (9.16)$$

where $r_e = 6378137\text{m}$ and μ are the current latitude. Seen as Trondheim has a latitude of 63.4297°, would this give a longitude change of approximately 3.5 degrees. Resulting in that the local local magnetic field would change to $\mathbf{m}_{to}^n = [13624, 247, 49863]^T$.

The heading error RMS using a local magnetic field of \mathbf{m}_{from}^n when we are actually have \mathbf{m}_{to}^n are seen in Table 9.4. Where it clearly can be seen that this would affect the heading estimation. Moreover, traveling north would mainly affect the pitch estimates whereas a longitudinal shift would have substantial yaw estimate impact⁵.

Discussion

Looking at the Euler angle errors in Table 9.3 is it seen that the Developed observer has the smallest RMS and Grip following right behind. Although, improvements could be made with better tuning, could it be argued that a RMS less or approximately equal to 1° are not bad concerning the high noise levels in the measurements.

A important issue regarding the Developed observer in this section are that the bird are now

⁴Meridian length is the distance between two points with the same longitude. See Figure 2.1

⁵The geographical localization would of course be a factor

Observer	RMS Heading (yaw) error [deg]	
	1.5° latitude shift	3.5° longitude shift
QUEST	1.90°	2.32°
MEKF	1.58°	2.10°
Grip	1.13°	1.81°
Developed	0.52°	1.54°

Table 9.4: Root-mean-square heading error impact using wrong local magnetic field. Comparing the performance of QUEST, MEKF, Grip and developed attitude observer. The observer assume the local magnetic field at Trondheim. Although the actual operation area are 178 km north and west from Trondheim

only governed by angular velocity rates and not by external forces acting on the bird. Consequently, the external forces τ are zero, and the bird are seen as a free-rotating rigid body by the angular velocity observer. Applying external input forces to the system would of course result in the needed of torque model or measured quantity in order for the observer to work.

The bias estimation of both MEKF and Grip are satisfactory, since both are able to converge to the drifting gyro bias. Where a trade-off between convergence speed and estimate variance are made.

Introducing magnetic distortions has a significant impact on the yaw accuracy as seen by Figure 9.19. In addition are it verified that the Developed algorithm are decoupling the roll and pitch estimates from the magnetic measurements. This are also seen for the Grip observer.

Utilizing the predicted states during magnetic disturbances decreases the heading estimate errors, the roll and pitch errors on the other hand increases for Grip. A fairly constant heading error are obtained by Grip during the disturbance - the gyro bias are kept constant during the disturbance. Further, the switching criterion (6.8) are highly dependent on the noise scale of the magnetic measurements. A smaller d could be used with less noisy measurement. Resulting in a tighter band and that magnetic disturbances are detected more easily and earlier.

As expected, are the effect of a time varying local magnetic field contributing in the heading estimation accuracy. The results in Table 9.4 view that approximately 1° increase in the heading error for all the observers. Although these results would be time varying in it self, depending on the geographical localization, are the errors nevertheless noticeable. On the contrary using GPS obtained localization at the boat or the tail-buoy, could WMM magnetic field values be passed to the bird on a semi-regular basis. Increasing the accuracy.

Regarding sensor noise and the resulting noisy estimates. The noise levels are quite high, and no filtering of the measurement are applied. The reason being the interest in the performance of the algorithms on the raw data from the provide IMU. In practise would low pass filtering and/or a less noisy IMU be preferable.

Chapter 10

Experimental Tests / Water Tests

The following sections presents results related to the estimation algorithms on real data. Raw data collected during two days of experimental water tests with the bird. Different motions, orientations and and speeds where tested. A total of 1.60 kilometer of seismic streamer cable and six birds were used under the tests. The bird data presented here are from a bird mounted on the seismic streamer approximately 400 meters from the aft of the boat. The raw IMU data are presented in Figure [10.2](#) and [10.3](#), representing day one and two respectively. A fairly constant heading were keep during the first day, apart from a 180° turn, and Bird rolling and wing yawing were the main test concern. The main focus on the second day where turning or yawing of the bird. This was done by large boat circle turns.

The data collected were uncalibrated raw data, so some calibration of the data where therefore necessary. The results of this calibration are presented in Chapter [11](#). Another factor where the sampling of the data. The sampled data were logged on a computer onboard the boat. Although the sampling in the embedded system is quite fast, were the computer sampling quite slow. Providing samples approximately at 10Hz. Moreover, due to no-consistent sample periods - handshake problems and such - were the samples clocked with the computer clock providing a dynamic sample period. Another issue related to the slow sample rate are the reliability of the gyro samples, since fast dynamics may be lost. Comprehensive and detailed conclusions could therefore not be made. Nevertheless, results regarding the observer's performance on this data



Figure 10.1: Field test. Tail-buoy in left photo (mounted on the aft of the cable), the Bird mounted on the cable in the up-right photo and the seismic cable winch in the down-right photo.

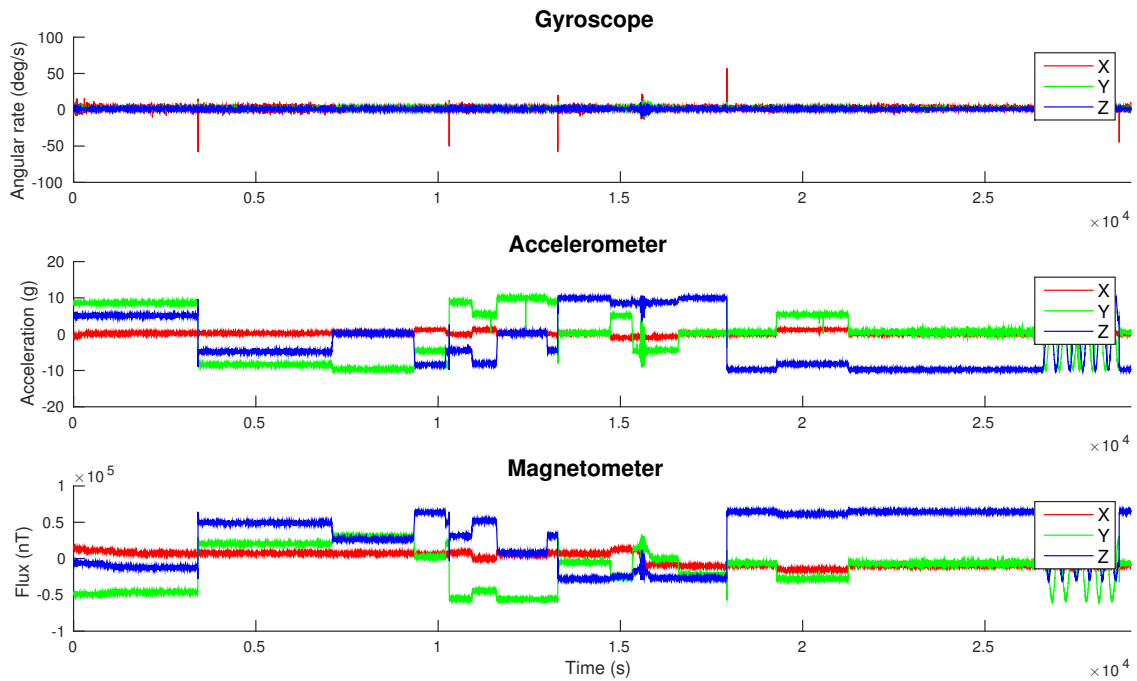


Figure 10.2: Experimental test, day one. Obtained raw sensor data

- calibrated - can be seen in Section 10.1.

10.1 Attitude Estimation

Results related to attitude estimation using the observers presented in Chapter 7 will be presented here.

The same inertial vectors are used under these tests as for the simulation studies, the local magnetic field at Trondheim - obtained from WWM - and a constant acceleration. This should be sufficient for the purpose of this section. However, see Section 9.5 for details concerning time varying local magnetic field.

Since much of the dynamic behavior are lost due to the slow sample period. Would for instance the PE condition, which are thought to be present, be lost. The basis of this PE as-

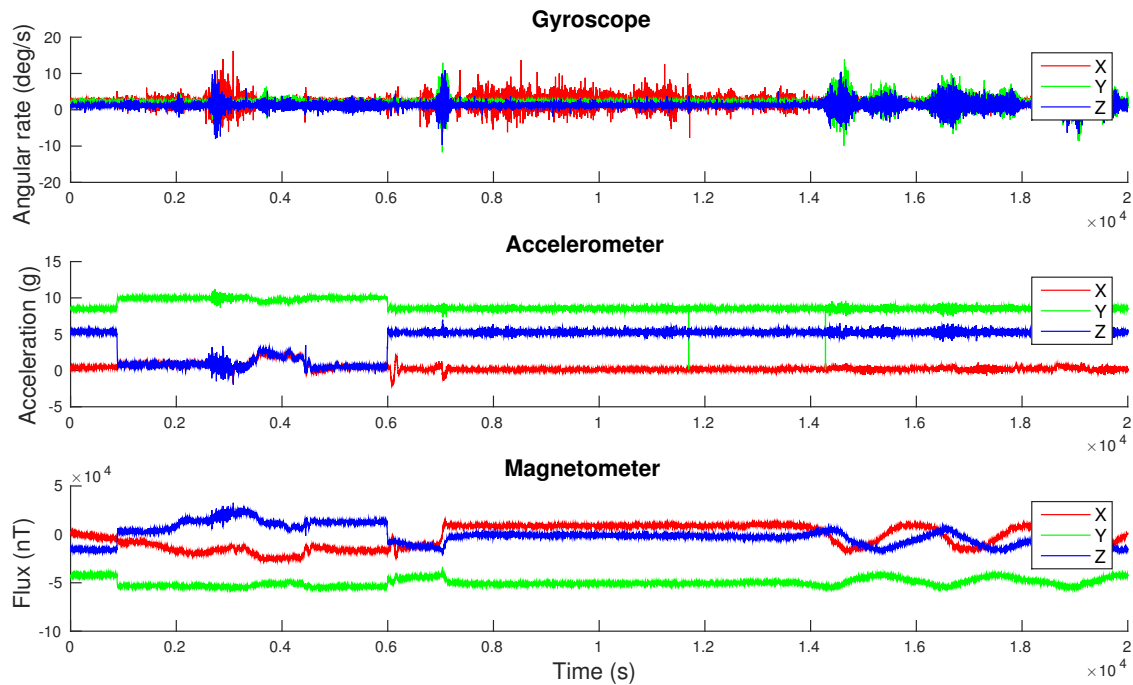


Figure 10.3: Experimental test, day two. Obtained raw sensor data

assumption are made on the premises of bird vibration in a fluid flow and constantly shifting wing angle. Single vector observer results will still be presented. The Developed observer would also be influenced by the loss of dynamic behavior, as the roll torque model(4.30) are highly affected by the system dynamics¹ (see Section 4.4.2). As previously mentioned, unknown coefficients do also contribute to the accuracy of the method, and the method are therefore omitted in this section.

Figure 10.4 and 10.5 present the results regarding the attitude estimation capability of the linear mapping and tilt compensation(LinearMapping), QUEST, MEKF and the Grip algorithm. As one can observe do non-linear Grip method stand out, producing good filtering capabilities and accurate estimation compared to the MEKF. The LinearMapping and QUEST introduces no filtering and this is clearly seen by the artifices in the estimates. Taking a closer look at the standard deviation (std), when yaw is fairly constant, are it seen that QUEST and LinearMapping has std of 2.75° , MEKF 1.19° and Grip 0.97° .

¹Pitch and yaw would of course have to have a separate torque model to get an full attitude estimation.

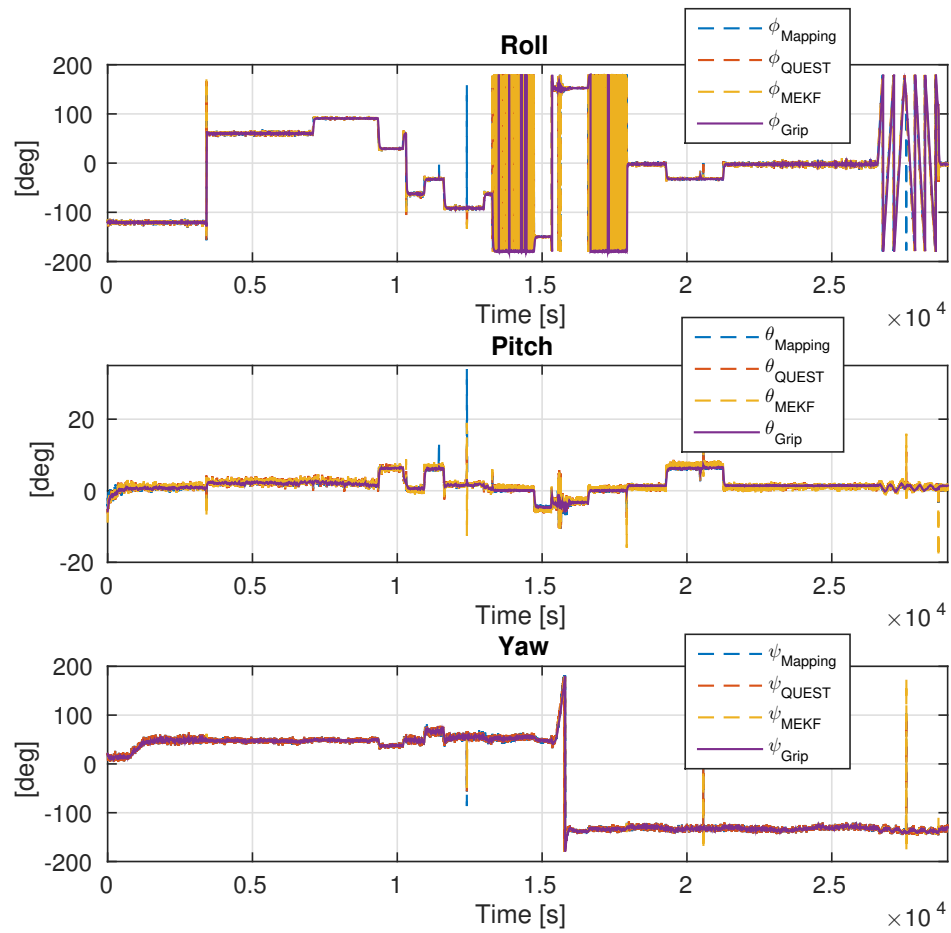


Figure 10.4: Field test Midøy day 1. Euler angle estimation, LinearMapping(striped, blue), QUEST (striped, red), MEKF(striped, yellow) and Grip(purple)

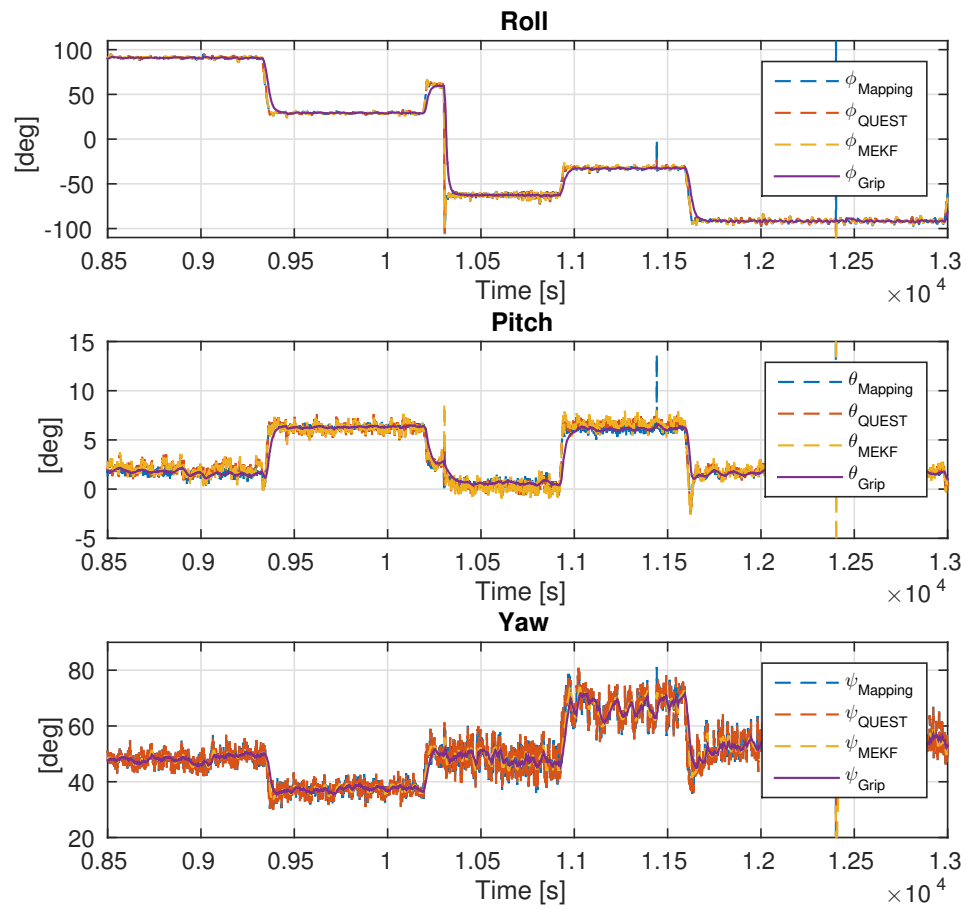


Figure 10.5: Field test Midøy day 1 zoom. Euler angle estimation, LinearMapping(striped, blue), QUEST(striped, red), MEKF(striped, yellow) and Grip(purple)

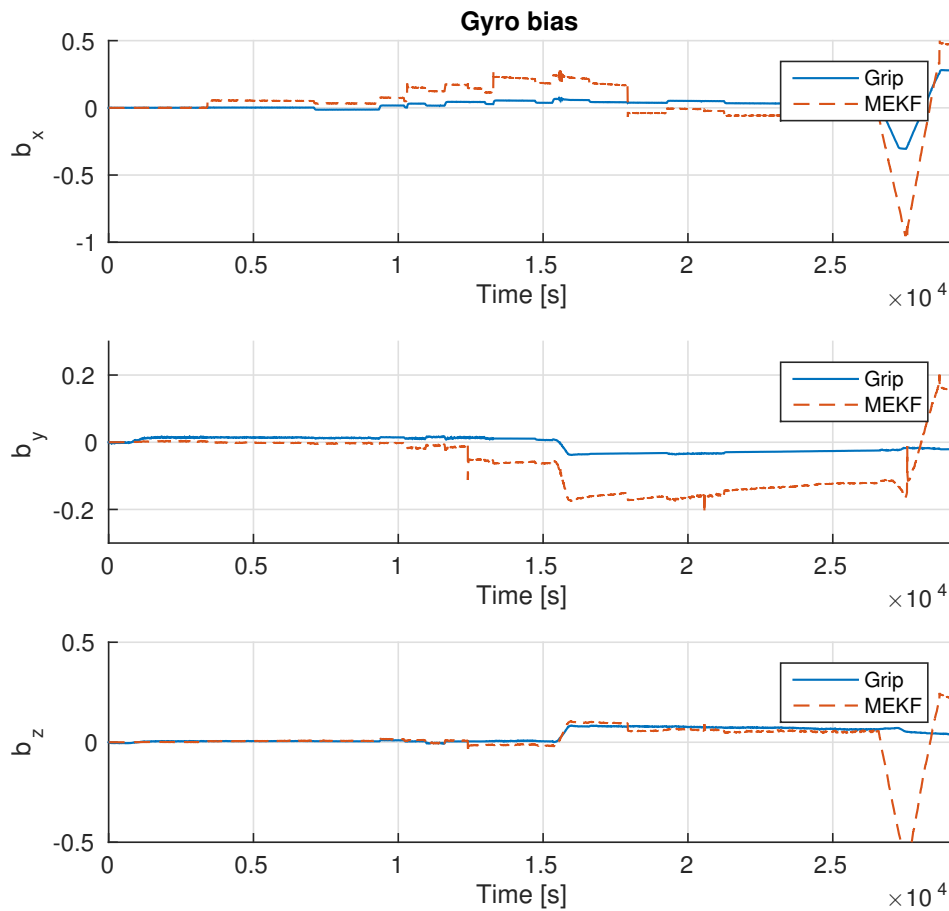


Figure 10.6: Field test Midøy day 1. Gyro bias estimation, MEKF(striped, red) and Grip(blue)

The bias estimates of MEKF and Grip are seen in Figure 10.6. One can observe that these estimates do not coincide. However, this is thought to be due to the loss of dynamic behavior.

Now looking at the results concerning single vector estimation. The Batista method are benchmarked against the MEKF solution, in Figure 10.7. The roll and pitch estimates are nicely estimated. Heading on the other hand are not estimated correctly. The most plausible reason being the loss of dynamics and the noisy drifting gyro measurements.

Additional result's, such as RMS Euler angles, quaternion estimates and estimation using data from the second day are seen in Appendix D.

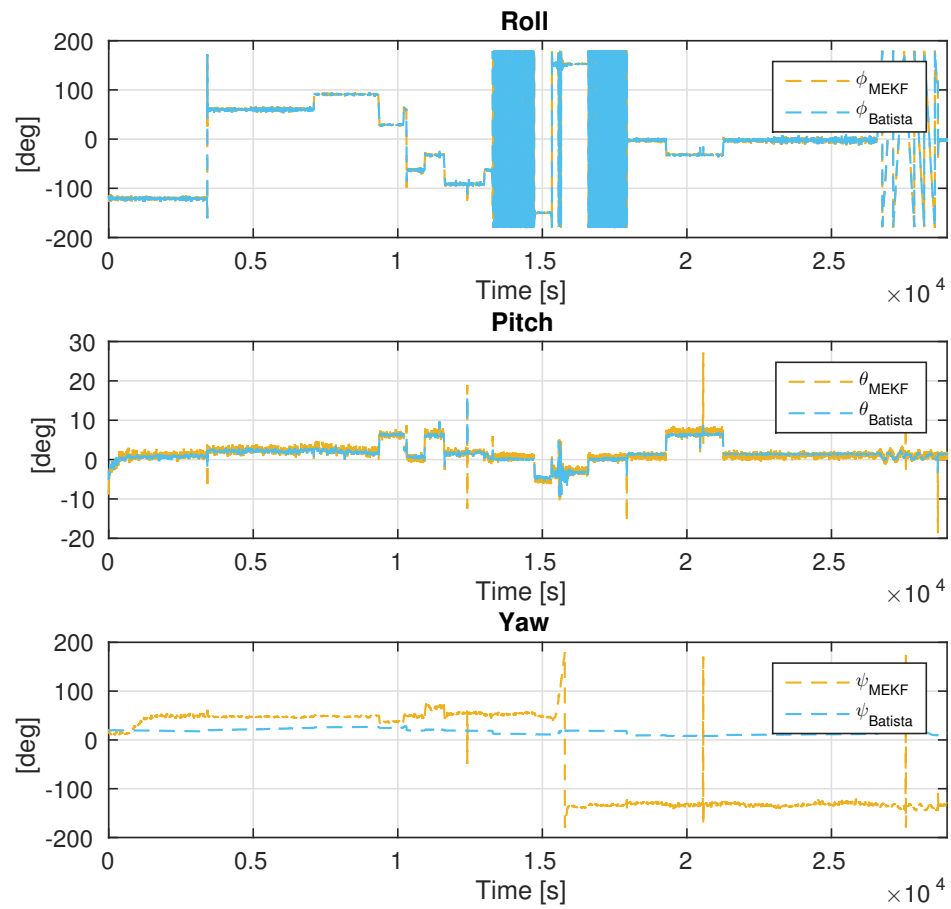


Figure 10.7: Field test Midøy day 1. Euler angle estimation using single vector observation, MEKF(striped, yellow) and Batista(striped, light blue)

Discussion

As described in the introduction for this chapter would a comprehensive and detailed conclusion nor analysis be made due to the slow sample rates. However, some aspects are still available for discussion. Namely the validity of the implemented algorithms and challenges related to these.

Firstly some observations that may be of interest. From Figure 10.2 it is observed that the angular velocity actually excised the limits - $\omega_{max} = 30$ deg/s - of a stable system. This situation are seen when the bird undergoes rapid roll motions. It's also seen, by looking at Figure 10.2, that during the 180° heading shift that fairly large roll motions occur. Which are probably due to that the bird are trying to stabilize itself, as the water-current angle of attack changes.

Another factor concerning the data are that no signal processing are utilized, only raw data. However, in a practice should some low level signal processing be utilized. See Section 6.3 for common signal processing techniques.

The LinearMapping are again verified as the most noisy and deviating method. Significant estimate errors occur during high angler velocity, producing large heading errors. Although much smaller, are heading errors in cases of high angular velocity also seen in the QUEST, and consequently the MEKF, method. The reason being the high state coupling, leading to that roll and pitch errors influencing the heading estimates. Grip do not suffer from this coupling, as verified in Section 9.5, and produces yaw estimates unaffected by the roll and pitch estimates. Moreover, Grip has the smallest heading std at 0.97°.

The Batista observer aren't preforming satisfactory. Roll and pitch estimates works fine, yaw not so much. Again, loss in fast dynamics my be a problem. Increasing the sample rate and running more tests would be of great interest.

It is also worth mentioning, that using the calibrated data, including bias scale and non-orthogonal errors, significantly reduces the errors in the estimates compared to calibrated data using only bias and scale error correction. See Section 11 for further discussion.

Chapter 11

Calibration

The following sections presents results and discussion related to the online calibration procedures from Section 4.2. Both by simulation - verification - and on the experimental collected data.

11.1 Calibration Simulation

In order to validate the calibration method for data collected during realistic bird behavior, are some simulations conducted. Due to the constraints on the bird orientation under operation will a full six point tumble test not be possible. However, 360° bird roll and $\pm 20^\circ$ wing yaw is possible. A magnetometer calibration are utilized to verify the calibration procedures. The measurements are subjected to constant bias, scale factor and orthogonal errors and measurement noise. The results of the calibration compared to their true values are seen in Table 11.1.

As seen from table are the scale-factors and non-orthogonal errors estimated nicely. The bias estimates b_y and b_z are also determined. However, the estimation of b_x are seen highly dependent on the scale of the pitching, and do not give consistent estimates. A solution would of course be to utilize a more complex maneuver. Although this could be difficult in practise.

	b_x	b_y	b_z	ξ_x	ξ_y	ξ_z	γ_{xy}	γ_{xz}	γ_{yz}
True	80	30	600	3.0000	0.0700	0.8900	0.1000	0.0500	0.0500
Estimate	90.7925	29.9849	600.1781	0.3006	0.0701	0.8902	0.1000	0.0500	0.0500

Table 11.1: Magnetometer calibration estimates, compared to their true values. Using ring formed data, 360° rolling and pitch less than 15°

On the contrary, performing multiple calibrations on the same data set to get an average of the b_x estimates could be a more suitable solution. Since the estimation converges so rapidly shouldn't this be a problem. Only three iterations are needed for the estimates to converge on the simulated data set.

Moreover, the inclusion of the *Backtracking Line Search* algorithm into the [Alonso and Shuster \(2002\)](#) method, introduce a significant reduction in the convergence rate - the number of iterations.

11.2 Calibration of Experimental Data

The Gauss-Newton method in Section 4.2 are applied to the batch of logged experimental data. Where the bird is rotated and some wing yawing is done (Raw Data from the first day). Multiple calibrations are conducted and the mean calibration parameters are seen in Table 11.2 Further,

	b_x [μ T]	b_y [μ T]	b_z [μ T]	ξ_x	ξ_y	ξ_z	γ_{xy}	γ_{xz}	γ_{yz}
Estimate	-0.0395	-1.7003	2.2985	1.2225	1.3153	1.2355	-0.0084	-0.0103	0.0024

Table 11.2: Magnetometer calibration estimates, experimental data.

a average of three iterations where used to obtain an estimate. The calibrated magnetometer measurements with the raw measurements are seen in Figure 11.1. Where one can clearly see the calibration centering and re-scaling of the measurements.

Calibration of the accelerometers are also conducted. The calibration are done using the gravity vector as reference. Producing the calibration parameters in Table 11.3. A total of 17

iterations where required to obtain the desired accuracy.

	b_x	b_y	b_z	ϵ_x	ϵ_y	ϵ_z	β_{xy}	β_{xz}	β_{yz}
Estimate	-0.0740	0.1664	0.7028	0.9948	0.9931	-0.0069	-0.0028	-0.0182	0.0022

Table 11.3: Accelerometer calibration estimates, experimental data.

Discussion

As verified in Section 11.1 do the calibration method presented in Section 4.2 produce reliable, fast and accurate estimates of the bias, scale factors and non-orthogonal errors in the measurements. Moreover, as briefly discussed in Section 10.1 do the attitude estimation using calibrated data - bias, scale and orthogonal - significantly reduce the noise levels and deviations in the estimates. Which indicates that the estimated errors in Table 11.2 and 11.3 are quite correct. Inclusion of the *Backtracking Line Search* are also seen advantageous.

Although calibration of the sensor not are the main issue of this thesis are allot of work put into the implementation and verification of the calibration. As this proved itself to be more cumbersome than first anticipated. Especially the calibration of the non-orthogonal errors. Initially where the method of Vasconcelos et al. (2011) attempted - at least the scale and bias part - since this was initially thought to be a more intuitive method. Although the calibration of the bias and scale factor using this approach was quite straightforward, did the inclusion of the non-orthogonal error not give satisfiable results (this could of course be some implementation faults made by the author). Nevertheless, calibration of the sensor measurements using the a ellipsoid model are interesting. For instance: Magnetic distortion could maybe be detected through the obtained ellipsoid model. By checking at each measured sample whether the sample lie on the surface of the estimated ellipsoid, deviations would then mean a magnetic distortion!

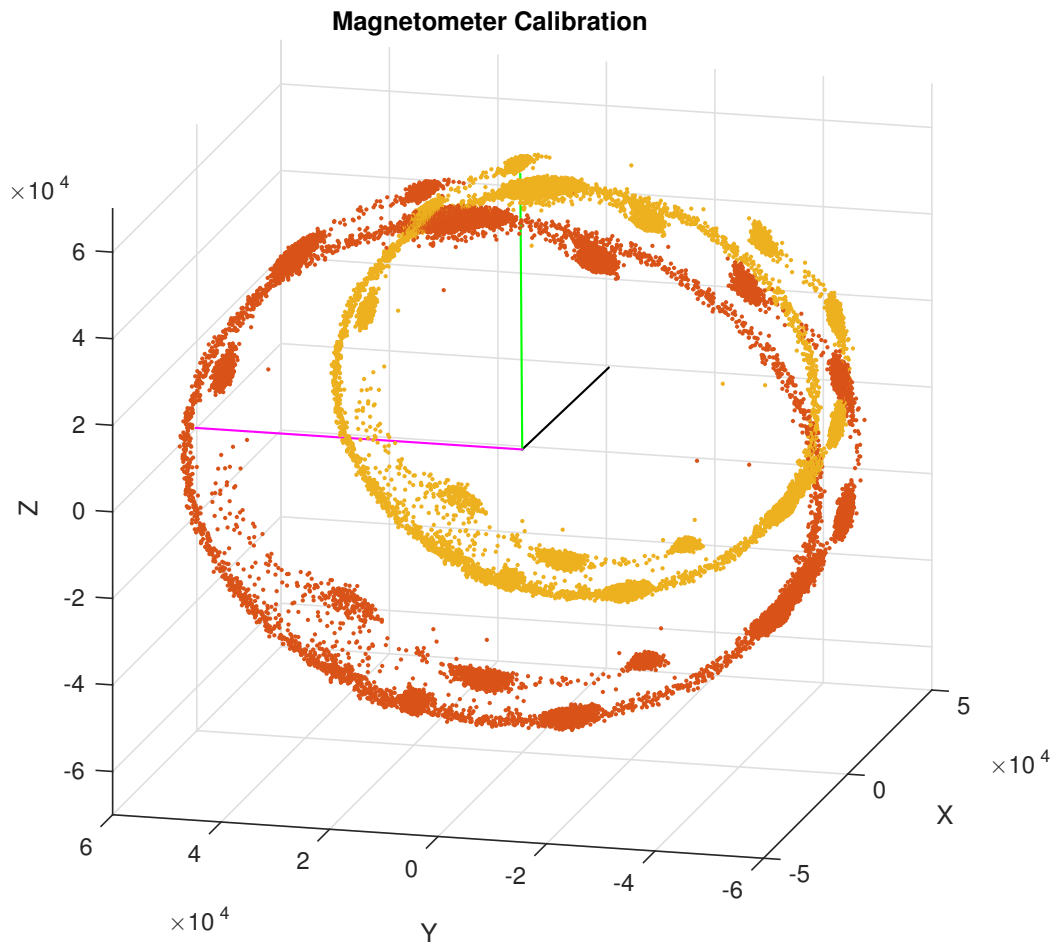


Figure 11.1: Calibrated magnetometer measurements (dotted, red) compared to the raw magnetic measurement (dotted, yellow). The estimated IMU-sensor axis in black, magenta and green.

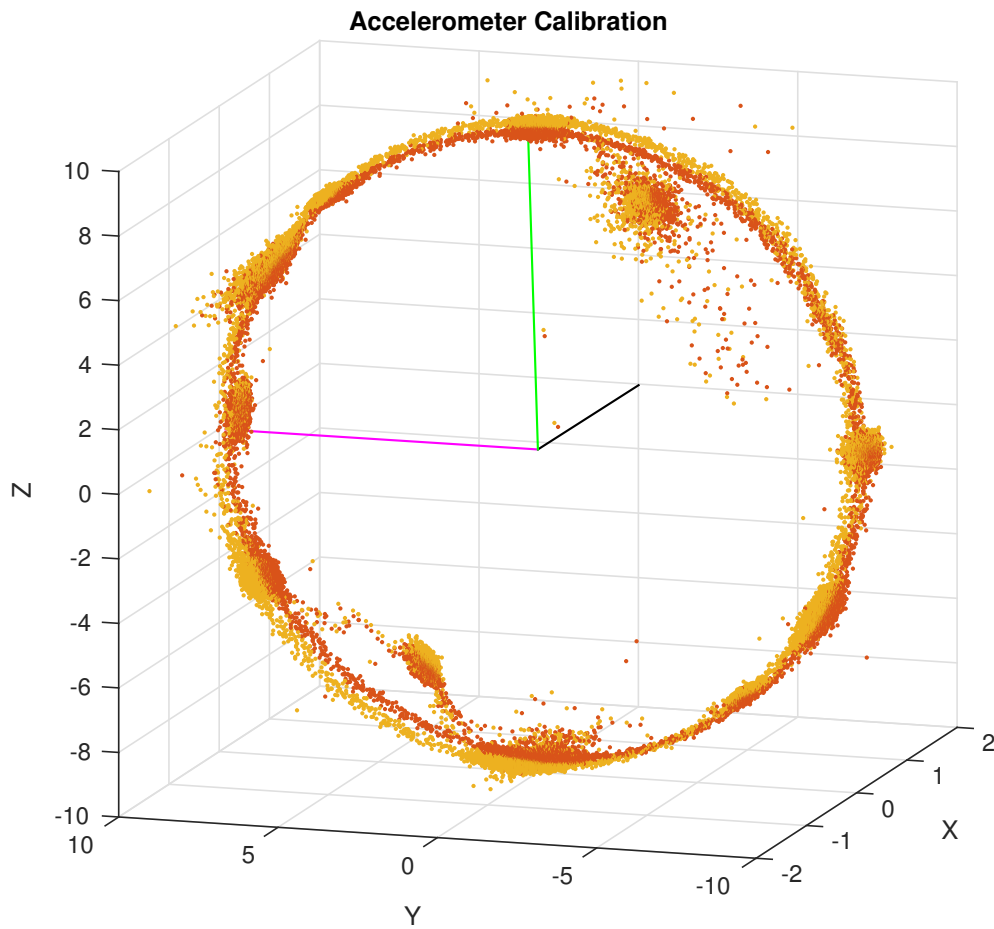


Figure 11.2: Calibrated accelerometer measurements (dotted, red) compared to the raw accelerometer measurement (dotted, yellow). The estimated IMU-sensor axis in black, magenta and green.

Part VI

Overall Discussion

Chapter 12

Overall Discussion

Sensor Calibration, Faults and Handling

Assumptions regarding the knowledge of the local magnetic field are evident in all the non-linear observes. Where the WWM are used to get these quantities. However, the geographical localization are needed to obtain the WWM magnetic field. [Mahony et al. \(2008\)](#) are presenting a method of estimating the direction of the local magnetic field. However, this method are not a proven robust method for obtaining the magnetic field. Increased attitude and heading error could then be a issue. It are therefore recommended to have a semi-regular update of the local magnetic field from the WWM. Either by storing the WWM in the bird and give longitude and latitude updates or by supplying magnetic field updates directly. The geographical localization could be obtained by the ship dragging the seismic cables, or a tail-buoy mounted GPS.

The IMU measurement accuracy are a major concern for the accuracy of the attitude and heading estimates. Providing a higher grade gyro (eg. FOG) or even a more accurate and expensive MEMS gyro would enable the use of the Batista method, using only a single vector to estimate the attitude. Which again will mean that the magnetic disturbances wouldn't be a problem. However, increasing the IMU-sensor accuracy would contribute to substantial overall cost of such a bird system - numerous birds are mounted at the seismic cable -, making this to a undesirable solution?

Calibration of the sensor measurements would of course reduce error sources. However, some time-varying magnetic disturbances would still be present. One could of course regularly calibrate the magnetic measurements by the method in Section 4.2, which are proven to be a robust and reliable calibration method. On the other-hand using a real-time method such as Crassidis et al. (2005) to update the magnetometer calibration error could be beneficial. A drawback would then be the computational burden. (Moreover, it should be a short transition from the batch based method in section 4.2 to the real-time Crassidis et al. (2005) method, as these are made under the same assumptions and use the same error model.) Contrary, keeping with a batch based method, for instance a ellipsoid fitting method could maybe be exploited to check for magnetic distortions. See further discussion in Section 11.

Utilizing the corrector-predictor formulation are advantageous. During measurement loss or magnetic disturbances as well as measurement synchronization. For instance during magnetic disturbances, using the switching-criterion (6.4) to turn on and off the estimate correction. However, the results of the (6.4) handling did not give substantial benefits. Noise levels and uncertainty in the measurements was a major contributor. Further analysis of a switching criterion are advised.

Both the Grip and the Developed observers have clear advantages in term's of their decoupling abilities. Since good roll and pitch estimation are obtained independently from magnetic disturbances, can a robust bird stability be obtained and additional heading errors be avoided.

MEKF and the Non-Linear Observers

As verified do the Gibbs vector error representation compared to the unit quaternion error representation give a more robust solution for the MEKF. Further, the overall MEKF algorithm may be more robust, or equivalent methods using time-varying gains. However, the computational burden of solving the Ricatti equations and similar equation are tremendous compared to a fixed gain non-linear observer. Utstumo and Gravdahl (2013) view this by comparing the non-linear Mahony et al. (2008) observer with the MEKF, resulting in that the non-linear Mahony observer were running more than ten times faster then the MEKF.

The global property of the Grip method have proven itself to give excellent performance. Enabling good filtering and accurate estimates. Easy to tune and enables both a single and multiple vector observations. Although the single vector solution only are applicable under PE and for small periods.

The Developed attitude observer show promising results regarding attitude estimation and accuracy. Producing accurate estimates, even with a low-cost IMU. The main reason being the omission of the noisy and biased gyro measurements. However, a measurement or a model of the external torques are evident. The Magnis angular velocity observer's ability of also estimating all the body-fixed measurements even show that the magnetometer and accelerometer measurements could be substituted by their estimates in the attitude determination. Further stability analysis of substituting these estimates into the injection term of the Developed observer(or a equivalent method) are then needed.

A detailed system model would be preferable, both in simulation and for testing of the Developed observer. Moreover, considering a robust attitude solution could also a system model contribute to a more fault-tolerant design. Fusing and switching between using a model based approach and a measurement fusion approach.

Part VII

Conclusion and Further Work

Chapter 13

Conclusion

Attitude observers using IMU-sensor fusion have been considered in this master thesis. Multiple observer's and strategies are tested and studied, looking for a suitable and accurate attitude observer for an underwater steering device. Fault cases and situation are emphasized.

To get as accurate results as possible with the current system. Are accuracy subjects ranging from attitude representations, discretization method's, signals processing, fault handling, calibration and different attitude observer also considered.

All the attitude observers that are studied are discretized and implemented, using a corrector-predictor formulation and a object-oriented implantation structure in MATLAB. A good and broad simulation model are developed in Simulink. Providing multiple test scenarios and different input strategies. Comparison of several non-linear attitude observer are made and benchmarked against the MEKF. Different error representations in the MEKF are also compared. Verifications and tests of the algorithms are done, both with simulated and experimental data.

The author have also proposed a new - $SO(3)$ confined - attitude observer. By fusing a angular velocity observer and a attitude correction term. Obtaining a locally exponential stable attitude observer.

A simple system roll model are designed and tested. Utilizing general fluid dynamics and foil theory.

As for the conclusion of a robust and accurate attitude observer. Is it advised to fuse a bird model with the Developed attitude observer and/or the Grip observer. Seen their decoupling abilities are evident in a robust bird stabilization. Furthermore, the corrector-predictor formulation, the single and multiple vector fusing ability of Grip are also advantageous in a fault-tolerant design.

Chapter 14

Further Work

- Investigate stability of fusing estimated body vector measurements - obtained by the Magnus alg. - into the Developed attitude observer's correction term.
- Investigate and further develop a model of the external forces acting on the bird. Contributing to a more accurate torque input model for the Developed attitude observer. Better fault-tolerance could also be obtained, through a switching mechanism between the IMU sensor fusion and a Bird model in fault cases.
- Implement and test the observer on the Bird embedded system.
- Investigate PE assumption related to a real bird motion. If PE, could a single vector observation be utilized.
- Investigate calibration methods to obtain an estimate of the measurement ellipsoid. Which could be the basis of a magnetic distortion switching criterion. Moreover, further investigate magnetic distortion compensation methods and/or switching criteria.

Part VIII

Appendix

Appendix A

Acronyms

NTNU Norges Teknisk Naturvitenskapelige Universitet - Norwegian University of Science and Technology

EoM Equations of Motion

PE Persistent Excitation

AUV Autonomous Underwater Vehicle

SO(3) Special Orthogonal group of order 3

GNSS Global Navigation Satellite System

INS Internal Navigation System

KF Kalman Filter

EKF Extended Kalman Filter

MEKF Multiplicative Extended Kalman Filter

QUEST QUaternion ESTimator

PE Persistent-Excitation

GES Globally exponentially stable

LES Locally exponentially stable

CG Crouch-Grossman

RK Runge-Kutta

RMS Root-Mean-Square

std Standard deviation

3D Three-dimensional

2D Two-dimensional

DP Dynamic Positioning

Appendix B

Assumptions, Definitions

The following appendix contains assumptions and attentional aspects related to the different observers and the calibration procedures.

B.1 Assumption 1

There exist a constant $c_{obs} > 0$ such that $\|w_i^n \times w_j^n\| \geq c_{obs}$, $i, j \in 1, \dots, k$ for each $t \geq 0$. Furthermore, w represent a arbitrary vectors. Under this assumption do the set

$$\left[\begin{array}{ccc} \frac{w_1^i}{\|w_1^i\|} & \frac{\mathbf{S}(w_1^i)w_2^i}{\|\mathbf{S}(w_1^i)w_2^i\|} & \frac{\mathbf{S}^2(w_1^i)w_2^i}{\|\mathbf{S}^2(w_1^i)w_2^i\|} \end{array} \right] \quad (\text{B.1})$$

where $i \in \{n, b\}$, provides an orthogonal basis in \mathbb{R}^3 . ([Grip et al., 2015](#); [Batista et al., 2014b](#)).

B.2 Assumption 2

The gyro bias \mathbf{b} is constant, and there exist a known $M_b > 0$ such that $\|\mathbf{b}\| \leq M_b$. ([Grip et al., 2015](#))

B.3 Assumption 3

The gyro $\omega^b(t)$ and its derivative $\dot{\omega}^b(t)$ are bounded for all time. ([Batista et al., 2014b](#); [Magnis and Petit, 2015b](#))

B.4 Definition 1

The definition of persistent excitation (PE). A signal that is satisfying

$$\int_t^{t+T} \mathbf{u}(\tau)\mathbf{u}(\tau)^T d\tau \geq \epsilon \mathbf{I} \quad \forall t \geq 0 \quad (\text{B.2})$$

for some $\epsilon, T \geq 0$. Is said to be PE. This is a widely used criterion in adaptive schemes where parameter convergence is one of the objects.

B.5 Theorem 3.5 in ([Nocedal and Wright, 2006](#))

Suppose that f is twice differentiable and that the Hessian $\nabla^2 f(x)$ is Lipschitz continuous (see (A.42)) in a neighborhood of a solution x at which the sufficient conditions (Theorem 2.4) are satisfied. Consider the iteration $x_{k+1} = x_k + p_k$, where p_k is given by (3.30). Then

- (i) if the starting point x_0 is sufficiently close to x^* , the sequence of iterates converges to x^* ;*
- (ii) the rate of convergence of $\{x_k\}$ is quadratic; and*
- (iii) the sequence of gradient norms $\{\nabla f_k\}$ converges quadratically to zero.*

Appendix C

Simulation Parameters

Simulation parameters utilized in the simulation are presented here. The magnetic, acceleration and angular rate specifications is based on the IMU data specs of the provided IMU and typical parameter errors retrieved from [Vik \(2014\)](#). The bird parameters are based on parameters given in the master thesis of [Barheim, 2009](#)) and project report of [Torseth et al. \(2014\)](#). Furthermore, the lift and drag coefficients are given on the basis of typical values given in [\(Newman, 1977\)](#) with Reynolds number $R_n < 10^6$

Initial conditions	
latitude (Trondheim)	63.4297 [°]
longitude (Trondheim)	10.3933 [°]
Sampling time	$f_s = 10$ [Hz] $\Rightarrow t_s = 0.1$ [s]
Earth angular rate (WGS-84)	$\omega_e = 7.292115e^{-5}$
Quaternion attitude	$\mathbf{q}_0 = [1, 0, 0, 0]^T$
Water density	$\rho = 1025$ [Kg/m ³]
Water in-flow velocity	$U = 4$ [knots] ≈ 2.0576 [m/s]

Table C.1: Initial simulation parameters

Bird parameters	
Mass	$m = 10$ [Kg]
Wing length	$l = 0.4$ [m]
Inertia	$I_x = 1/2ml^2$ [kg m ²]
Projected wing area	$A = 0.12$ [m ²]
Lift coefficient	$C_L = 0.5$
Drag coefficient	$C_D = 0.00$
Max angular rate	$\omega_{max} = 30$ [deg/s]
Hydrodynamic Quadratic drag coefficient	$K_{\phi\phi} = 47$
Hydrodynamic Linear drag coefficient	$K_{\phi} = 40$
Hydrodynamic restoring coefficient	$K_s = 0.07$
Added mass	$K_{\dot{\phi}} = 40$
Lever arm	$\mathbf{r}_{wing}^{bird} = [-0.15, -0.15\sin(\alpha), 0.15]^T$ [m]

Table C.2: Bird simulation parameters

Accelerometer

Local gravity vector	$\mathbf{a}^n = [0, 0, 9.81]^T$ [m/s ²]
Measurement noise (from IMU spec)	$\mathbf{w}_1 = 4e^{-3}$
Bias dot noise	$\mathbf{w}_2 = 1e^{-6}$
Scale factor error noise	$\mathbf{w}_3 = 1e^{-6}$
Misalignment error noise	$\mathbf{w}_4 = 1e^{-6}$
Initial scale factor error	$\epsilon = 1e^{-6}$
Initial misalignment error angles	$\beta = 1e^{-6}$
Initial bias	$\mathbf{b}_{acc} = 1e^{-3}$

Gyroscope

Initial angular rate	$\omega^b = [0, 0, 0]^T$
Measurement noise (from IMU spec)	$\mathbf{w}_1 = 0.005\pi/180$
Bias dot noise	$\mathbf{w}_2 = 1e^{-6}$
Scale factor error noise	$\mathbf{w}_3 = 1e^{-6}$
Misalignment error noise	$\mathbf{w}_4 = 1e^{-6}$
Initial scale factor error	$\kappa = 1e^{-6}$
Initial misalignment error angles	$\alpha = 1e^{-6}$
Initial bias	$\mathbf{b}_{gyro} = 1e^{-3}$

Magnetometer

Local magnetic field	$\mathbf{m}^n = [13772, 604, 49823]^T$ [nT]
Measurement noise (from IMU spec)	$\mathbf{w}_1 = 8e^{-3}$
Bias dot noise	$\mathbf{w}_2 = 1e^{-7}$
Scale factor error noise	$\mathbf{w}_3 = 1e^{-5}$
Misalignment error noise	$\mathbf{w}_4 = 1e^{-5}$
Initial scale factor error	$\xi = 1e^{-2}$
Initial misalignment error angles	$\gamma = 1e^{-2}$
Initial bias	$\mathbf{b}_{mag} = 10e^{-3}$

Table C.3: IMU simulation parameters

Appendix D

Additional Results

D.1 Developed observer - Correction Term Comparison

In the Developed observer are the correction term (3.29) utilized. Although, the more standard correction term $\sigma = \sum_{j=1}^n k_j \mathbf{v}_j^b \times \mathbf{v}_j^n$ could also be applied. However, a ill-condition attitude problem would greatly benefit of using (3.29). To clarify this are a small comparison presented.

A ill-conditioned attitude problem, would be when the vectors utilized in the attitude determination have almost the same direction. Assuming that the gravitational and geomagnetic vector are utilized, are Trondheim a good candidate for a ill-conditioned problem - $\bar{\mathbf{m}} \approx [0.2664, 0.0117, 0.9638]^T$ and $\bar{\mathbf{a}} = [0, 0, 1]^T$.

The simulated data are governed by the angular velocity in Table 9.2. Both correction terms are provided with the same non-high gains ($k_1 = 1, k_2 = 0.3$) to make to results comparable. As seen from Figure D.1 are yaw error much higher for the standard correction term. Increasing the gains for the standard correction term ($k_1 = 7, k_2 = 7$) would of course help, however amplifying the estimate variance \rightarrow more noise sensitive.

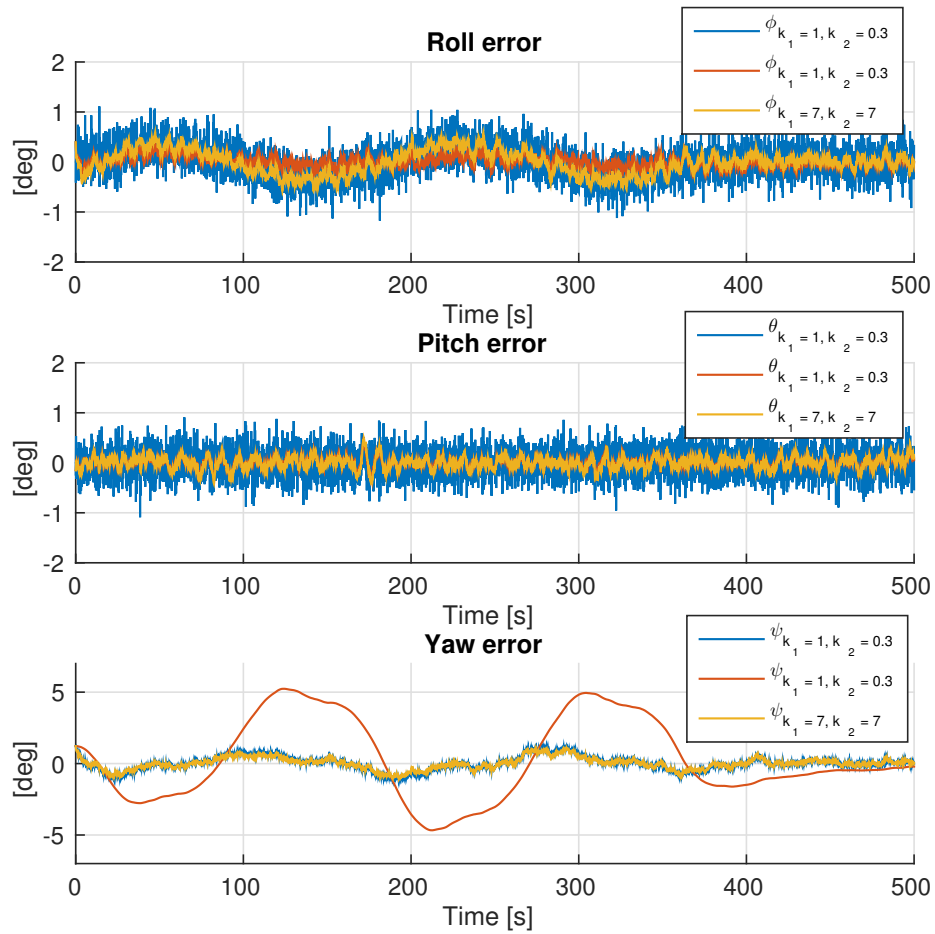


Figure D.1: Comparison of different injection terms in the Developed observer.

D.2 Additional Field Test Results

Results from day two and additional results from the field test during day one are presented.

First Day

Conversion of the Euler angles estimates to the $\{bird\}$ -frame are seen in Figure D.2. The attitude estimates, using quaternion, are given in Figure D.3, whereas the RMS Euler representation are viewed in Figure D.4. The estimates from the auxiliary body vector observer, of Batista, gave the normalized acceleration estimates seen in Figure D.5

Second Day

Quaternion estimates are given in Figure D.7, whereas the Euler angle estimates and RMS Euler angle and $\{bird\}$ -frame euler angles are shown in Figure D.6 and D.9 respectively. MEKF and Grip gyro bias estimation are viewed in Figure D.10

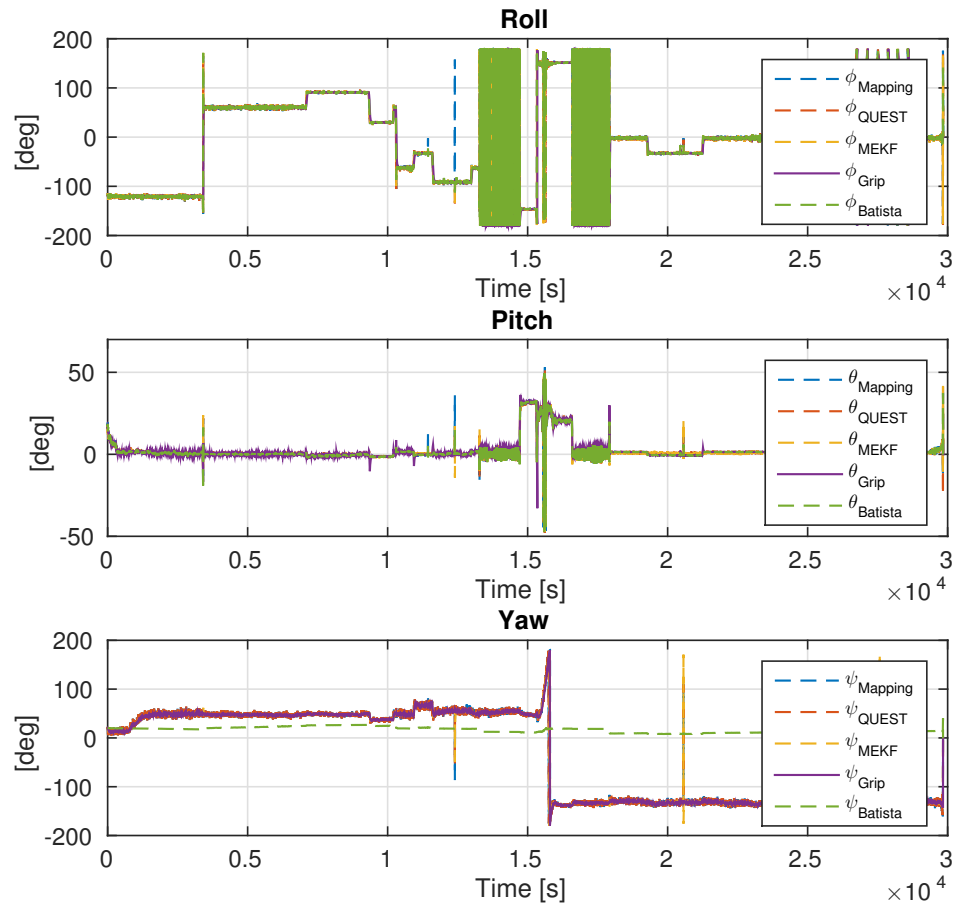


Figure D.2: Field test Midøy day 1. Euler angle estimation, converted to the Bird frame, linear mapping(striped, blue), QUEST(striped, red), MEKF(striped, yellow) and Grip(purple)

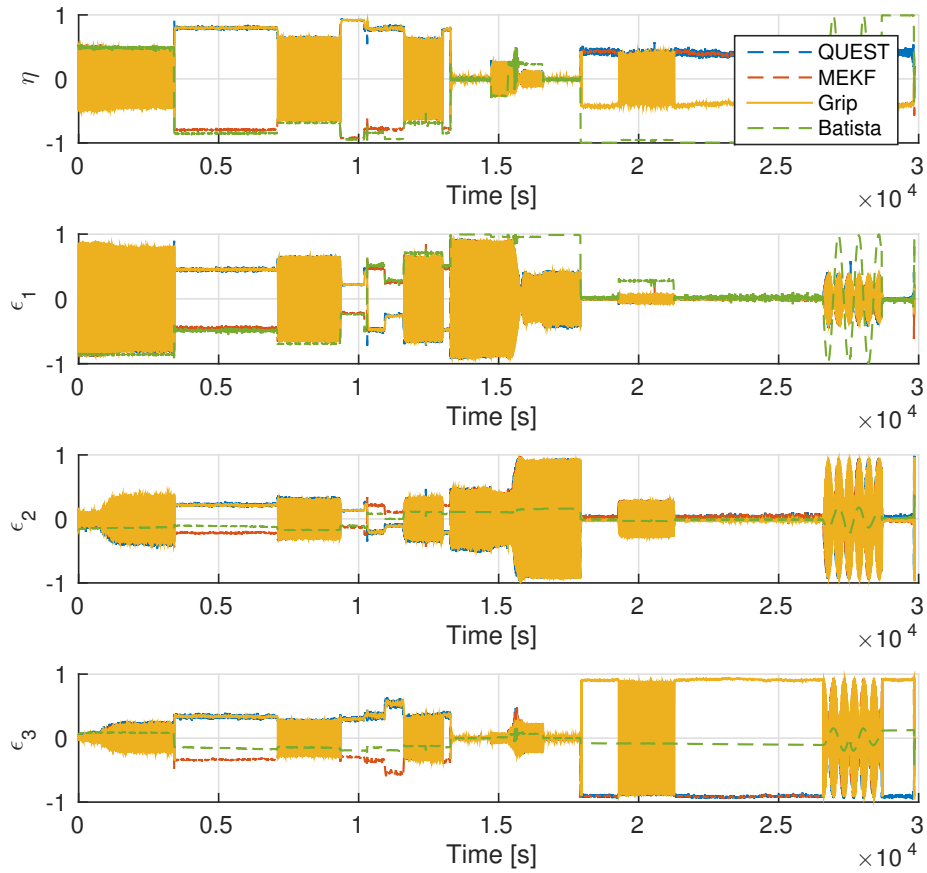


Figure D.3: Field test Midøy day 1. Quaternion estimation, QUEST(striped, blue), MEKF(striped, red), Grip(yellow) and Batista(striped, green)

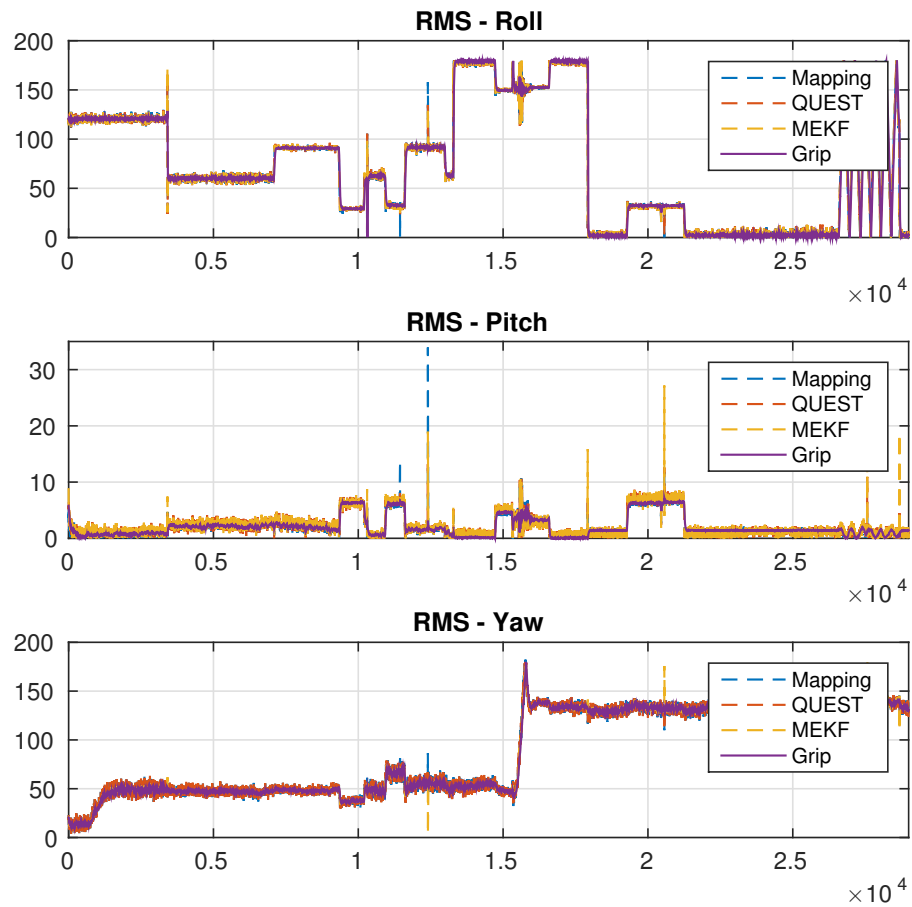


Figure D.4: Field test Midøy day 1. Euler angle estimation RMS, linear mapping(striped, blue), QUEST(striped, red), MEKF(striped, yellow) and Grip(purple)

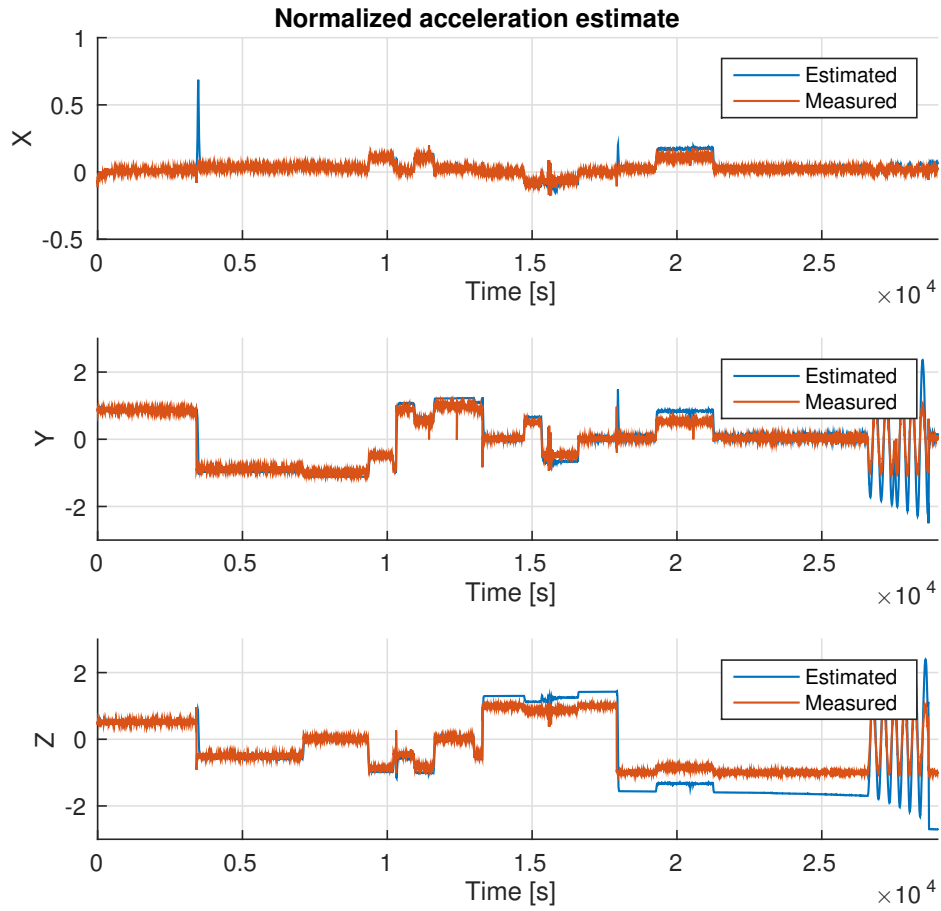


Figure D.5: Field test Midøy day 1. Batista, normalized acceleration estimates(blue) and the measured(red).

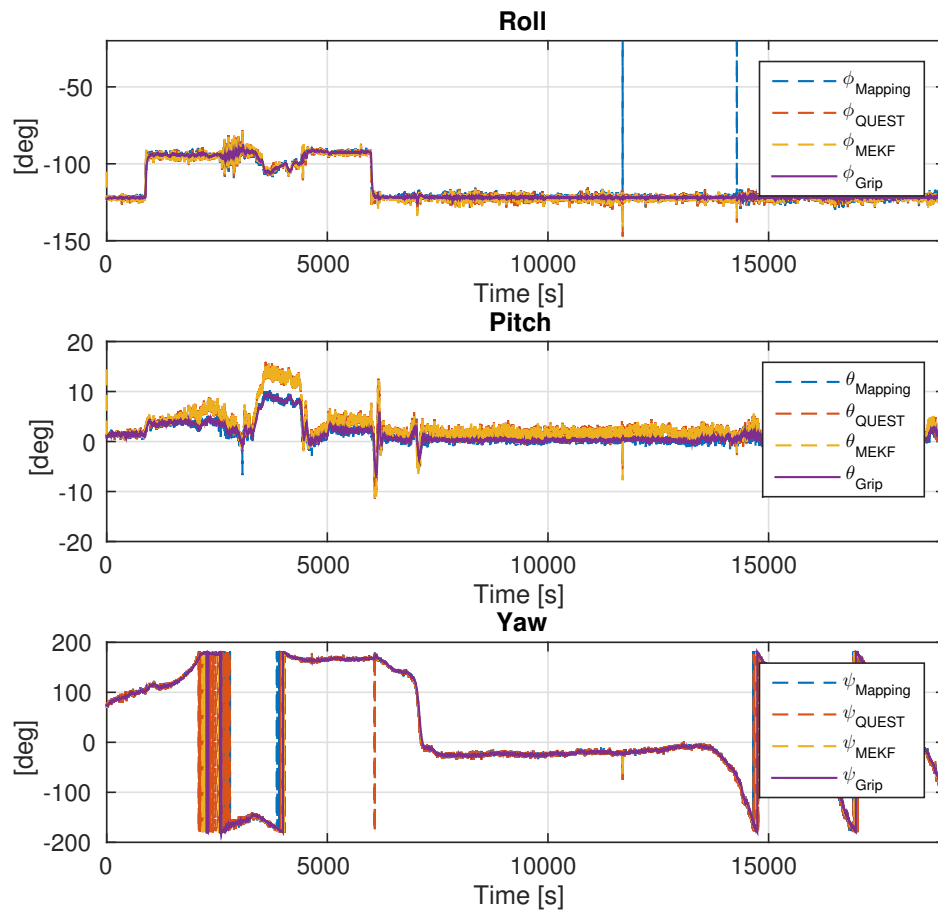


Figure D.6: Field test Midøy day 2. Euler angle estimation, LinearMapping(striped, blue), QUEST (striped, red), MEKF(striped, yellow) and Grip(purple)

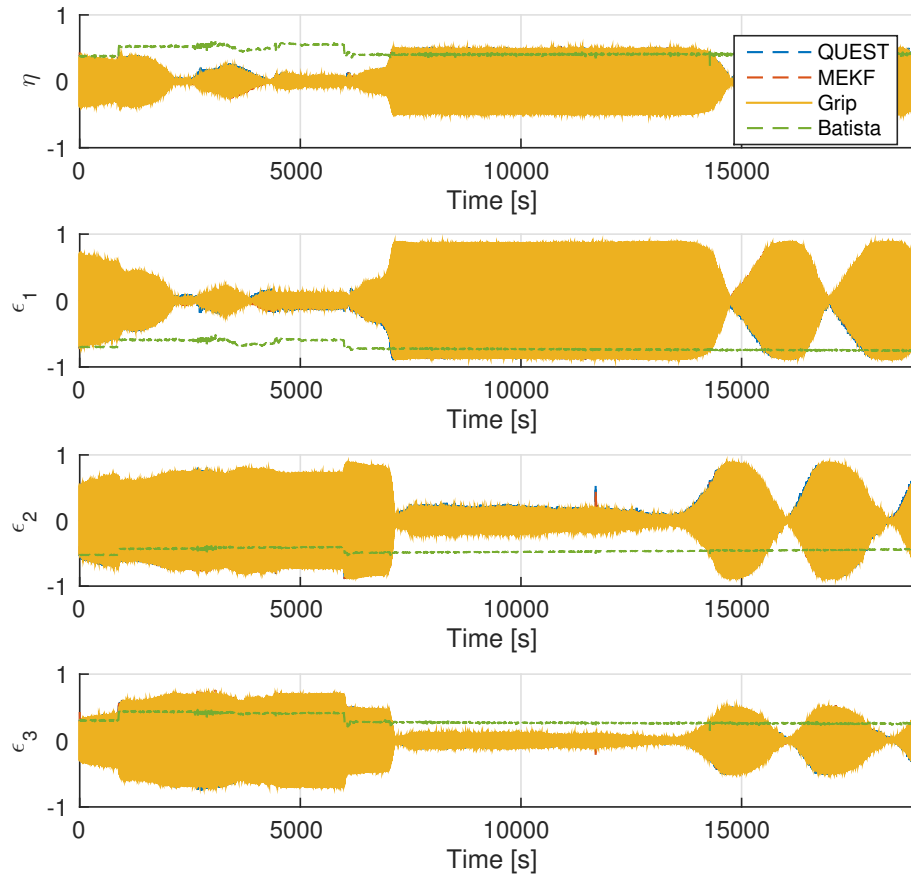


Figure D.7: Field test Midøy day 2. Quaternion estimation, QUEST(striped, blue), MEKF(striped, red), Grip(yellow) and Batista(striped, green)

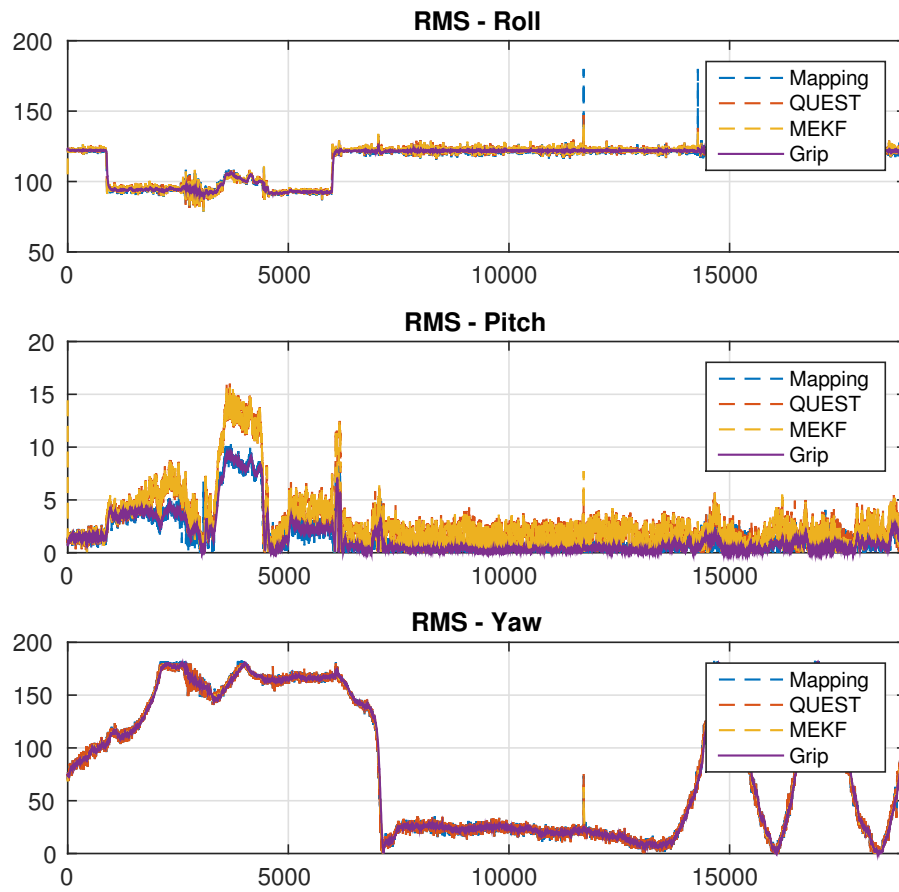


Figure D.8: Field test Midøy day 2. Euler angle estimation RMS, linear mapping(striped, blue), QUEST(striped, red), MEKF(striped, yellow) and Grip(purple)

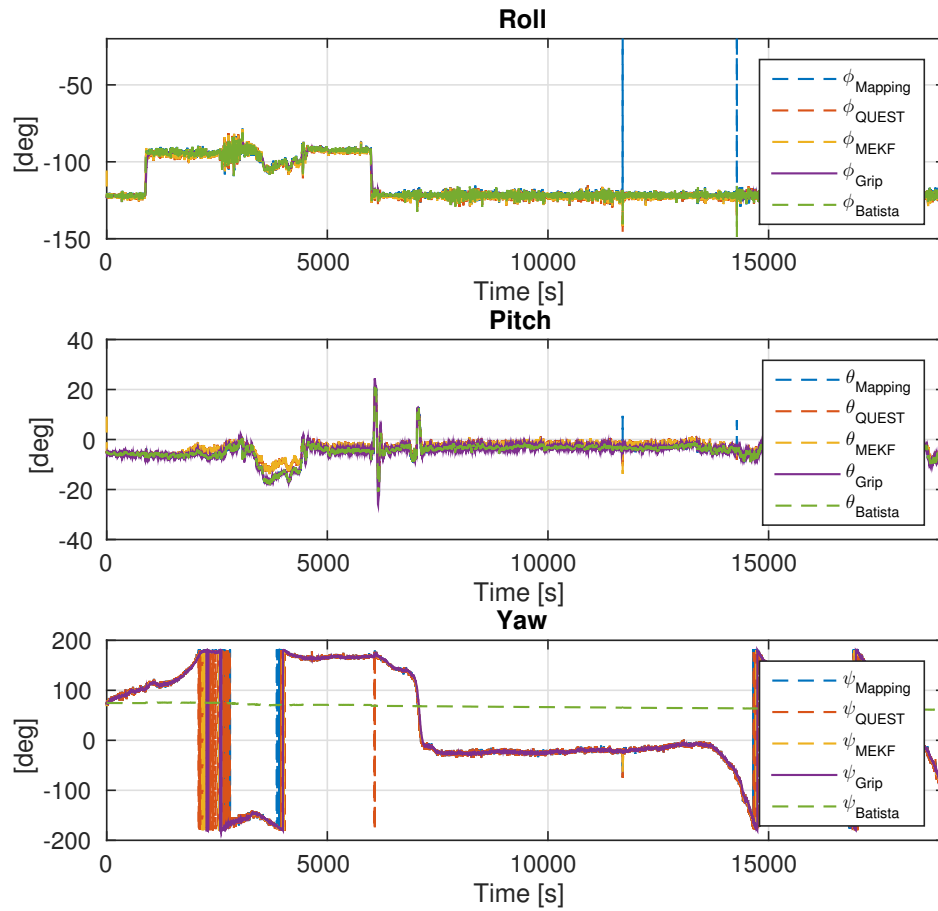


Figure D.9: Field test Midøy day 2. Euler angle estimation, converted to the Bird frame, linear mapping(striped, blue), QUEST(striped, red), MEKF(striped, yellow) and Grip(purple)

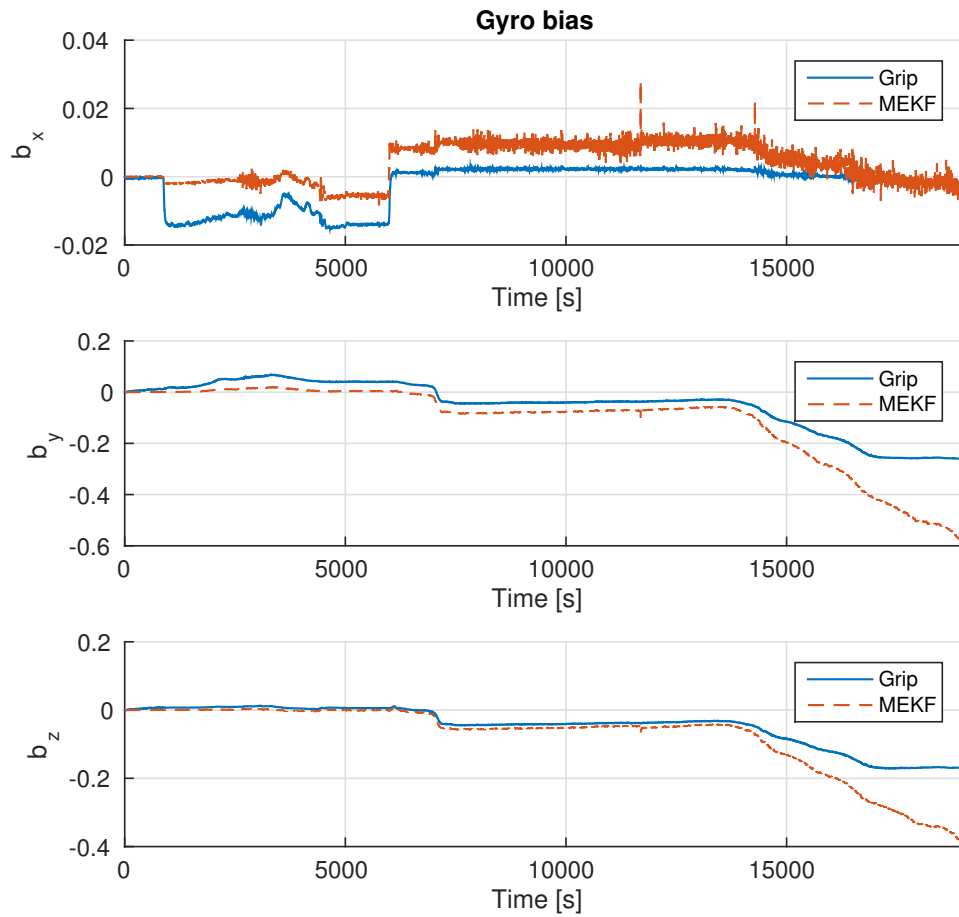


Figure D.10: Field test Midøy day 2. Gyro bias estimation, MEKF(striped, red) and Grip(blue)

Appendix E

Simulink Model

Overviews over the Simulink simulation model are presented. Figure E.1 show the IMU model. The gyro model, Figure E.2, are governed by the bird angular velocity, sensor noise, bias, scale factor and misalignment angles. The magnetometer model, Figure E.3, governed by the quaternion attitude and a constant magnetic field, then adds sensor noise, bias, scale factor and misalignment angles. The same goes for the accelerometer model, Figure E.2, are governed by the quaternion attitude, gravitational acceleration and centripetal acceleration, and adds sensor noise, bias, scale factor and misalignment angles. The kinetic, Figure E.5, and kinematic, Figure E.6, model produce the quaternion attitude by input torque and angular velocity. The rest of model subsystems are omitted to to space.

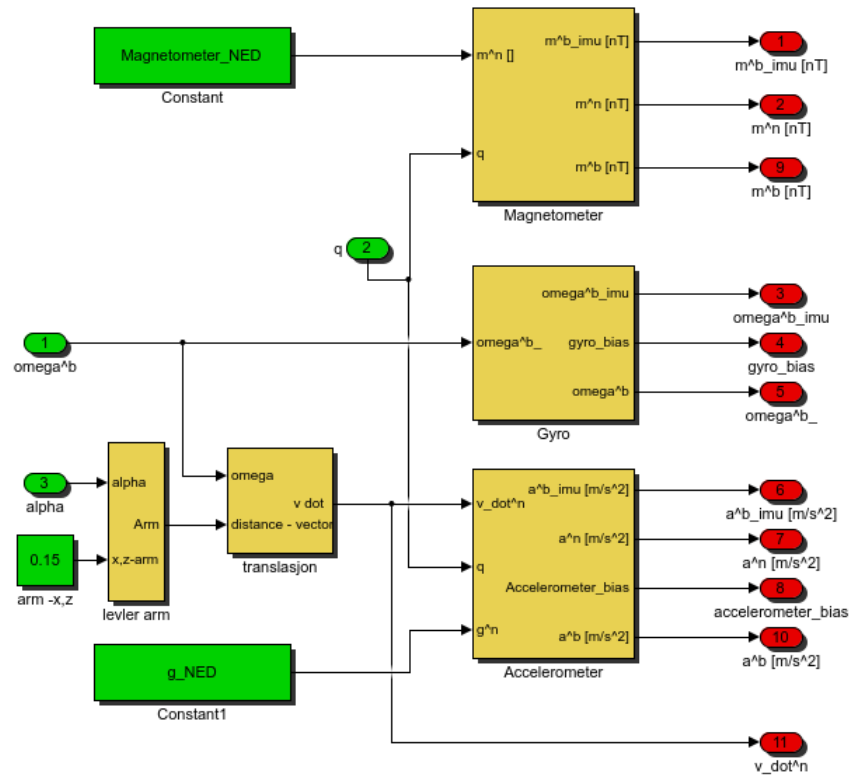


Figure E.1: IMU model.

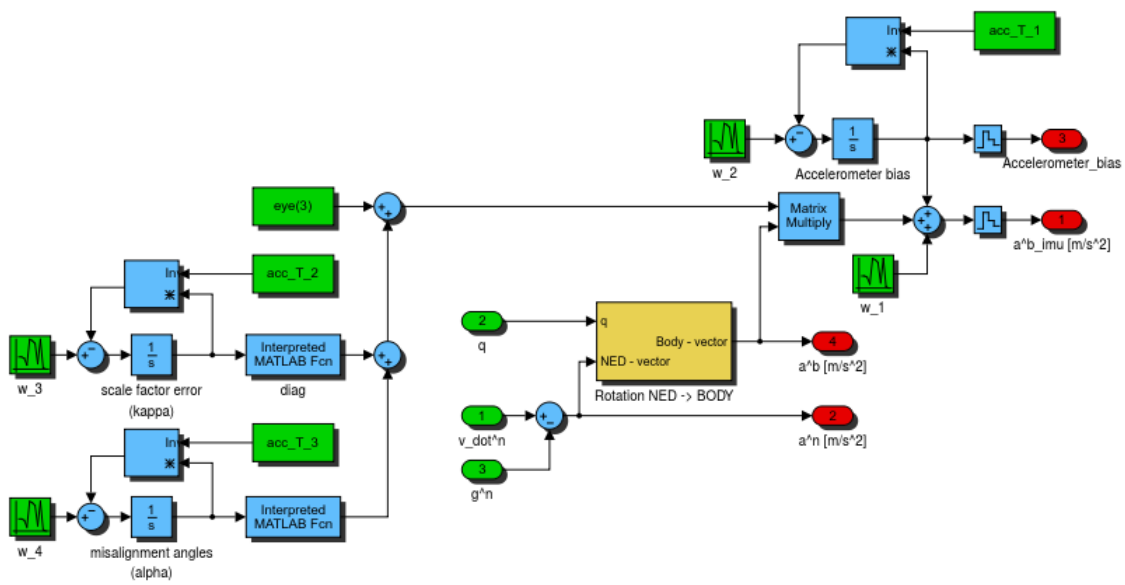


Figure E.2: Accelerometer model

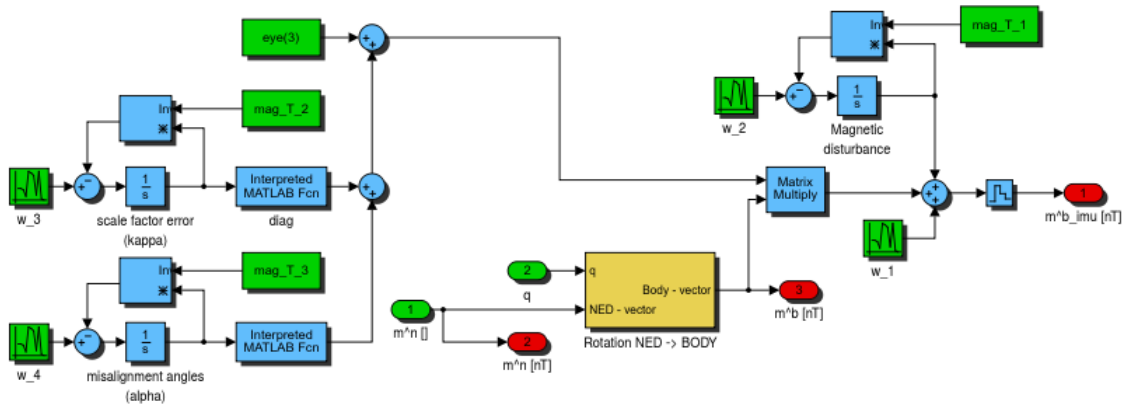


Figure E.3: Magnetometer model

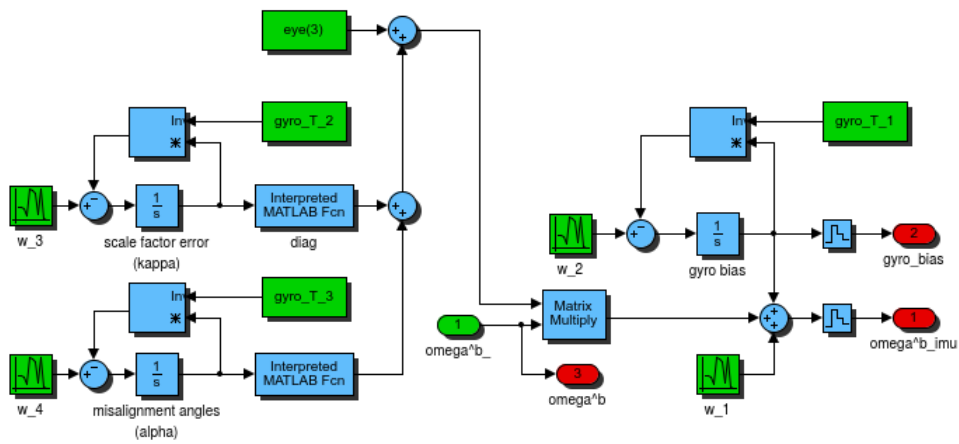


Figure E.4: Gyroscope model

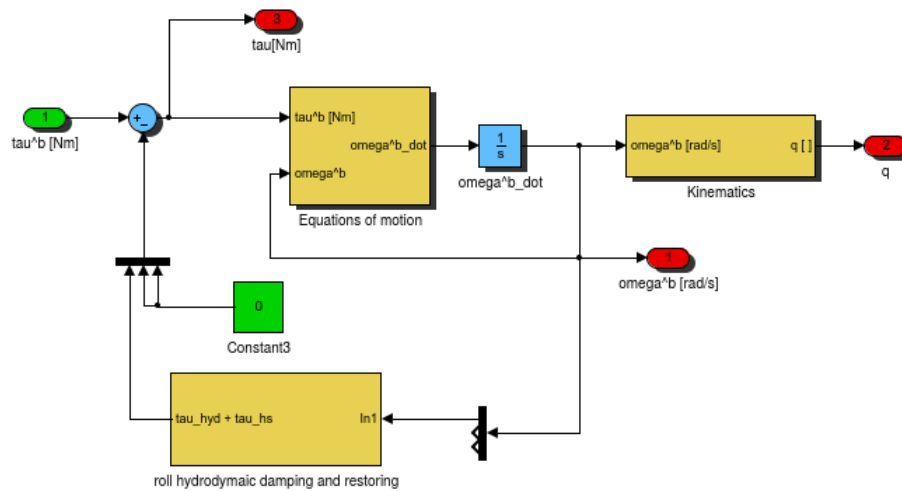


Figure E.5: Kinetic model

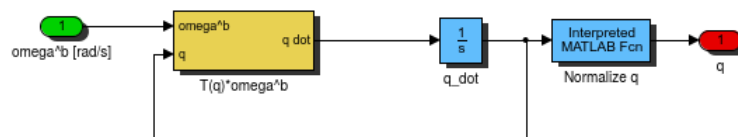


Figure E.6: Kinematic model.

Bibliography

- Alonso, R. and Shuster, M. D. (2002). Complete linear attitude-independent magnetometer calibration. *Journal of the Astronautical Sciences*, 50:477–490.
- Barheim, T. r. (2009). *Lateral control of towed submerged cables*. Master thesis, Norwegian University of Science and Technology.
- Batista, P., Silvestre, C., and Oliveira, P. (2011). GES Attitude Observers - Part I: Multiple General Vector Observations. *IFAC Proceedings Volumes (IFAC-PapersOnline)*, 18.
- Batista, P., Silvestre, C., and Oliveira, P. (2012a). A {GES} attitude observer with single vector observations. *Automatica*, 48(2):339–388.
- Batista, P., Silvestre, C., and Oliveira, P. (2012b). Sensor-Based Globally Asymptotically Stable Filters for Attitude Estimation: Analysis, Design, and Performance Evaluation. *IEEE Transactions on Automatic Control*, 57(8):2095–2100.
- Batista, P., Silvestre, C., and Oliveira, P. (2014a). Attitude and Earth Velocity Estimation - Part I: Globally Exponentially Stable Observer.
- Batista, P., Silvestre, C., and Oliveira, P. (2014b). Attitude and Earth Velocity Estimation - Part II: Observer on the Special Orthogonal Group.
- Bhat, S. P. and Bernstein, D. S. (2000). A topological obstruction to continuous global stabilization of rotational motion and the unwinding phenomenon. *Systems & Control Letters*, 39(1):63–70.

- Bonnabel, S., Martin, P., and Rouchon, P. (2008). Symmetry-Preserving Observers. *IEEE Transactions on Automatic Control*, 53(11):2514–2526.
- Borup, K. T., Fossen, T. I., Braga, J., and de Sousa, J. B. (2014). Nonlinear observer for depth-aided INS: Experimental evaluation using an AUV. *22nd Mediterranean Conference on Control and Automation*, pages 1231–1236.
- Bryne, T. H., Fossen, T. I., and Johansen, T. a. (2014). Nonlinear observer with time-varying gains for inertial navigation aided by satellite reference systems in dynamic positioning. *22nd Mediterranean Conference on Control and Automation*, pages 1353–1360.
- Crassidis, J. L., Lai, K.-L., and Harman, R. R. (2005). Real-Time Attitude-Independent Three-Axis Magnetometer Calibration. *Journal of Guidance, Control, and Dynamics*, 28:115–120.
- Crassidis, J. L., Markley, F. L., and Cheng, Y. (2007). A Survey of Nonlinear Attitude Estimation Methods. *Journal of Guidance, Control, and Dynamics*, 30(1):12–28.
- Davies, R. J., Stewart, S. a., Cartwright, J. a., Lappin, M., Johnston, R., Fraser, S. I., and Brown, a. R. (2004). 3D Seismic Technology: Are We Realising Its Full Potential? *Geological Society, London, Memoirs*, 29:1–10.
- Egeland, O. and Gravdahl, J. T. (2002). *Modeling and Simulation for Automatic Control*. Marine Cybernetics, Trondheim.
- Fossen, T. I. (2011). *Handbook of Marine Craft Hydrodynamics and Motion Control*. John Wiley & Sons, Ltd, Chichester, UK.
- Foster, C. C. and Elkaim, G. H. (2008). Extension of a two-step calibration methodology to include nonorthogonal sensor axes. *IEEE Transactions on Aerospace and Electronic Systems*, 44(3):1070–1078.
- Grip, H. F., Fossen, T. I., Johansen, T. a., and Saberi, a. (2012a). A nonlinear observer for integration of GNSS and IMU measurements with gyro bias estimation. *2012 American Control Conference (ACC)*, pages 4607–4612.

- Grip, H. F., Fossen, T. I., Johansen, T. a., and Saberi, a. (2012b). Attitude Estimation Using Biased Gyro and Vector Measurements With Time-Varying Reference Vectors. *IEEE Transactions on Automatic Control*, 57(5):1332–1338.
- Grip, H. F., Fossen, T. I., Johansen, T. a., and Saberi, A. (2013). Nonlinear observer for GNSS-aided inertial navigation with quaternion-based attitude estimation. *2013 American Control Conference*, pages 272–279.
- Grip, H. v. F r., Fossen, T. I., Johansen, T. A., and Saberi, A. (2011). Attitude estimation based on time-varying reference vectors with biased gyro and vector measurements. In *IFAC Proceedings Volumes (IFAC-PapersOnline)*, volume 18, pages 8497–8502.
- Grip, H. v. F r., Fossen, T. I., Johansen, T. a., and Saberi, A. (2015). Globally exponentially stable attitude and gyro bias estimation with application to GNSS/INS integration. *Automatica*, 51:158–166.
- Grip, H. v. F r., Saberi, A., and Johansen, T. a. (2012c). Observers for interconnected nonlinear and linear systems. *Automatica*, 48(7):1339–1346.
- Hua, M.-D., Ducard, G., Hamel, T., Mahony, R., and Rudin, K. (2014a). Implementation of a Nonlinear Attitude Estimator for Aerial Robotic Vehicles. *IEEE Transactions on Control Systems Technology*, 22(1):201–213.
- Hua, M.-D. M.-D., Martin, P., and Hamel, T. (2014b). Velocity-aided Attitude Estimation for Accelerated Rigid Bodies. *IEEE Conf. on Decision and Control (CDC)*, pages 328–333.
- Kalman, R. E. (1960). A New Approach to Linear Filtering and Prediction Problems. *Journal of Basic Engineering*, 82(1):35.
- Magnis, L. and Petit, N. (2015a). Angular velocity nonlinear observer from single vector measurements. *IEEE Transactions on Automatic Control, en révision*, (March).
- Magnis, L. and Petit, N. (2015b). Angular velocity nonlinear observer from vector measurements. *Automatica, en révision*, (March).

- Mahony, R., Hamel, T., and Pflimlin, J. (2005). Complementary filter design on the special orthogonal group SO (3). *Decision and Control, 2005 and 2005 European Control Conference. CDC-ECC '05. 44th IEEE Conference on*, (1):1477–1484.
- Mahony, R., Hamel, T., and Pflimlin, J. J.-M. (2008). Nonlinear Complementary Filters on the Special Orthogonal Group. *IEEE Transactions on Automatic Control*, 53(5):1203–1218.
- Mahony, R., Hamel, T., Trumpf, J., and Lageman, C. (2009). Nonlinear attitude observers on SO(3) for complementary and compatible measurements: A theoretical study. In *Proceedings of the IEEE Conference on Decision and Control*, pages 6407–6412.
- Markley, F. (2003). Attitude error representations for Kalman filtering. *Journal of Guidance, Control, and Dynamics*, Vol. 26, No. 2, pages 311–317.
- Markley, F. L. and Mortari, D. (2000). Quaternion Attitude Estimation Using Vector Observations. *Journal of the Astronautical Sciences*, 48(2):359–380.
- Martin, P. and Salaün, E. (2007). Invariant observers for attitude and heading estimation from low-cost inertial and magnetic sensors. In *Proceedings of the IEEE Conference on Decision and Control*, pages 1039–1045.
- Newman, J. N. (1977). *Marine Hydrodynamics*. MIT Press.
- Ngdc.noaa.gov (2015a). Geomagnetic Field Models at NGDC. <http://www.ngdc.noaa.gov/geomag/models.shtml>. [Accessed 13 Feb. 2015].
- Ngdc.noaa.gov (2015b). Magnetic Field Calculators. <http://www.ngdc.noaa.gov/geomag-web/#igrfwmm>. [Accessed 20 Feb. 2015].
- Nguyen, T. and Egeland, O. (2004). Observer design for a towed seismic cable. *American Control Conference, 2004. Proceedings of the 2004 (Volume:3)*, 3:2233 – 2238.
- Nijmeijer, H. and Fossen, T. (1999). *New directions in nonlinear observer design*. Springer London.
- Nocedal, J. and Wright, S. J. (2006). *Numerical Optimization*. Springer New York.

- Osborne, P. (2013). The Mercator Projections. Technical report, Edinburgh.
- Shuster, M. D. (1993). A Survey of Attitude Representations. *The Journal of the Astronautical Sciences*, 1:439–517.
- Shuster, M. D. (2006). The quest for Better attitudes. *Astronautical Sciences*, 54.
- Shuster, M. D. and Oh, S. D. (1981). Three-axis attitude determination from vector observations. *Journal of guidance and control*, 4:70–77.
- Spong, M. W., Hutchinson, S., and Vidyasagar, M. (2006). *Robot Modeling and Control*. John Wiley & Sons, Inc., New York.
- Sørensen, A. J. (2013). Marine Control Systems. *Department of Marine Technology Norwegian University of Science and Technology. Lecture Notes TMR4240 Marine Control Systems*.
- Takahashi, N., Souza, A., and Tosin, M. (2009). Execution time of quest algorithm in embedded processors. *Brazilian Symposium on Aerospace Eng. & Applications*.
- Torseth, H. H., Barheim, T. r., and Blanke, M. (2014). Roll Control of Control Unit. Technical report.
- Treven, A. and Saje, M. (2015). Integrating rotation from angular velocity. *Advances in Engineering Software*, 42(9):723–733.
- Utstumo, T. and Gravdahl, J. (2013). Implementation and Comparison of Attitude Estimation Methods for Agricultural Robotics. *in proceedings of the 4th IFAC Conference on Modelling and Control in Agriculture, Horticulture and Post Harvest Industry (AgriControl 2013), Aalto University, School of Electrical Engineering, Espoo, Finland*.
- Vasconcelos, J. F., Elkaim, G., Silvestre, C., Oliveira, P., and Carneira, B. (2011). Geometric approach to strapdown magnetometer calibration in sensor frame. *IEEE Transactions on Aerospace and Electronic Systems*, 47(2):1293–1306.
- Vik, B. r. (2014). Integrated Satellite and Inter al Navigation Systems. *Department of Engineering Cybernetics University of Science and Technology. Lecture Notes in TTK5 Kalman Filtering and Navigation*.

Vik, B. r. and Fossen, T. I. (2000). A nonlinear observer for integration of GPS and inertial navigation systems. *Modeling, Identification and Control*, 21:193–208.

Wahba, G. (1965). A least squares estimate of satellite attitude. *SIAM review*, 7(3):409–409.

WIKIPEDIA (2015). Gnomonic projection. http://en.wikipedia.org/wiki/Gnomonic_projection. [Accessed 17 Feb. 2015].